

Institute for Nuclear Research
Russian Academy of Sciences
60th October Anniversary Prospect, 7A
Moscow, 117 312, Russia

Study of a Beam Transport and Distribution System for the TESLA X-ray Facility

Moscow-Hamburg, 2000

Working group:

INR

V.N. Aseev, V.V. Balandin, S.E. Bragin, N.I. Golubeva, V.E. Loskutov, V.N. Mikhailov,
V.V. Paramonov, P.I. Reinhardt-Nickoulin

DESY

K. Flöttmann

Edited by V.V. Paramonov, K. Flöttmann

Moscow-Hamburg, 2000

Contents

1	Introduction	5
2	The electron beam collimation	6
2.1	Spoiler survival	6
2.2	Secondary particles	8
2.3	Transverse phase space collimation	12
2.3.1	Triplet lattice	12
2.3.2	FODO lattice	12
2.4	Energy collimation	14
2.4.1	Collimation in the elevation arc.	14
2.4.2	Collimation in the extraction region.	14
2.4.3	Energy collimation insertion in the long straight line.	15
2.4.4	The implementation of the sweeping system	17
2.5	Radiation dose estimations.	18
2.6	Summary	19
3	Elevation of the beam to ground level	22
3.1	General requirements	22
3.2	Design of arcs	24
3.3	Tracking studies	29
3.4	Summary	29
4	The electron beam distribution system	35
4.1	General requirements	35
4.2	Optics for the separation of the bunch trains (D1)	35
4.3	Optics between undulators (D2)	39
4.4	Matching sections	42
4.5	Integration of the fast feedback system	49
4.6	Summary	50
5	The Diagnostic Commissioning line	51
5.1	The DCL structure	51
5.2	Diagnostic tools and methods	56
5.2.1	The beam intensity measurements	57
5.2.2	Beam Position Monitors (BPMs)	58
5.2.3	Transverse beam profile measurements	58
5.2.4	Energy spread and longitudinal bunch shape estimation	59
5.3	Summary	60
6	The beam transport to the dumps	61
6.1	The basic layout of the optics	61
6.1.1	Matching Section	61
6.1.2	Bending arc	63
6.1.3	Defocusing section	63
6.2	Scheme1: One beam dump for one beam line	65
6.3	Scheme2: One beam dump for two beam lines	68

6.4	Summary	68
7	Post accelerator	69
7.1	Accelerating structure and RF system	69
7.2	Energy modulation depth	70
7.3	Energy modulation velocity	70
7.4	Summary	72
8	Magnetic elements	73
8.1	Pulsed magnets	73
8.2	Pulse power supply scheme.	74
8.3	Parameters of DC magnetic elements and power requirements	77
8.4	Summary	79
9	Conclusion	81
	References	82

1 Introduction

The X-ray Laser Facility is an important part of the TESLA project. With the unique beam parameters the X-ray Free Electron Laser (FEL) opens new possibilities in both fundamental and applied investigations. The general FEL concept and parameters are described in [1]. Being a part of the TESLA complex, the FEL facility will use the beam from the main TESLA linac. Beams with an energy of $12 \div 50 GeV$ are required for the FEL in comparison with $250 GeV$ or more for the TESLA collider. The FEL laboratory is planned now at the same site as the TESLA collider experimental hall. So, for the FEL applications the beam should be extracted from the TESLA linac, transported over a long distance of $\approx 12 km$, collimated both in transverse and longitudinal planes, elevated to the earth surface, distributed between different users and finally directed to beam dumps. The unique FEL parameters are strongly based on the unique beam parameters - phase space density, a bunch charge and the narrow energy spread. All magneto-optic systems should handle the beam "carefully" to avoid the energy spread growth and emittance dilution due to a uncorrelated synchrotron radiation. Another important parameter for a transport and distribution system is the energy acceptance. To scan with the FEL radiation wavelength during a bunch train one should scan the bunch energy inside the bunch train. No magnet element tuning is possible during the train. The transport and distribution system should accept bunches with different energies and transport them carefully without a parameter deterioration. So, the systems should satisfy to contradictory scientific requirements, together with space limitations and cost reduction wishes. In this report a results of the study for the collimation, elevation and distribution system are presented.

2 The electron beam collimation

The electron beam collimation is necessary both for the collider operation mode and for the FEL operation mode to remove particles which don't satisfy the design requirements. The general idea of the collimation is fairly simple: particles with parameters outside the limits should be separated from the useful part of the beam and be absorbed. Two options of the collimation exists - ordinary collimation for "halo" particles, usually with a lowered intensity in comparison to the total beam, and protection collimation, when the total beam is out of the parameter range and should be absorbed. Both for collider and for FEL applications, the electron beam has a high bunch charge, a high energy in the bunch and very small dimensions. Already several bunches can lead to a destruction of hardware components if directly hit by the beam.

For a high energy electron beam the collimator scheme spoiler-absorber (see Fig. 2.1.1) is now used. The particles to be collimated should go through the spoiler. After multiple scattering in the spoiler material the shower of secondary particles arises with increased number of particles (the shower build-up factor is > 1) but with strongly decreased energy density. The secondary particles after the spoiler are very forward-peaked, and should be absorbed in the absorber at some distance from the spoiler.

For the protection collimation the spoiler survival problem exists. When the beam directly hits the spoiler, it should survive during a definite time period, sufficient for an emergency system to turn off the beam. For this purpose the beam spot-size should be increased by a special optics scheme to decrease the beam energy density. The rms beam spot-size $\sigma_x \cdot \sigma_y$ can be estimated as:

$$\sigma_x \cdot \sigma_y = \sqrt{(\beta_x \epsilon_x + (\frac{D_x \delta W}{W_0})^2) \beta_y \epsilon_y}, \quad (1)$$

where $\epsilon_{x,y}$ are the beam emittances in the x, y planes, $D_x, \beta_{x,y}$ are the dispersion and optics functions in the place of the spoiler position, $\delta W, W_0$ are the rms energy spread and the average energy, respectively.

2.1 Spoiler survival

The beam collimation should permit also the protection properties and the collimator hardware should survive if a certain amount of primary beam bunches strikes the spoiler directly. The number of these bunches should be sufficient to switch on an emergency system.

When a primary beam strikes the material, there is a sudden local temperature rise, that creates local thermal stresses. If the temperature rise leads to the exceeding of the stress limit, micro fractures can develop in the spoiler material. It has been observed in experiments, that if the local temperature rise exceeds four times the equivalent temperature T_{st} for the stress limit, a shock wave due to the very fast thermal rise will cause the material to fail completely or "delaminate" [2]. Thus, the allowed temperature rise is limited either by the melting point of the material T_{melt} or four times the stress limit at which the material will fail drastically. In the Table 2.1.1. the properties for possible spoiler materials are presented. Considering different materials, the titanium alloy, the same as the material for the conversion target in the TESLA positron injector, looks as the most practical choice for the spoiler material.

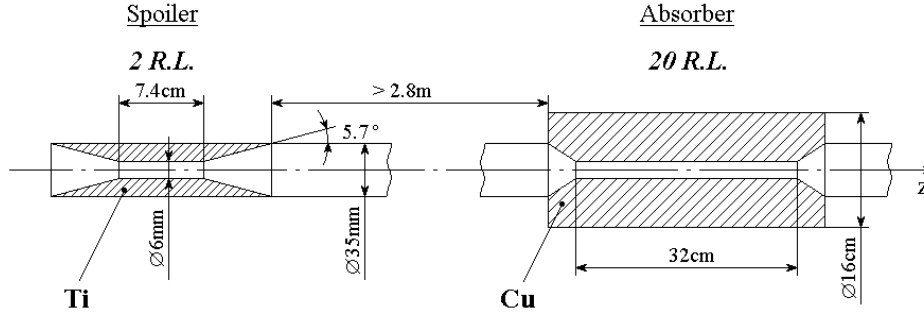


Figure 2.1.1: The spoiler and the absorber scheme. $RL=X_0$ - radiation length.

Table 2.1.1: Material parameters for the spoiler [3].

Material	Be	C	Al	Ti	Cu	Fe
Radiation length, cm	35.7	21.7	9.0	3.7	1.4	1.80
$(\frac{\partial E}{\partial x})_{min}, \frac{MeV}{cm}$	3.1	3.6	4.4	7.2	12.8	11.60
Specific heat $C_p, \frac{J}{cm^3 C^o}$	3.3	1.9	2.5	2.4	3.5	3.80
Melting point T_{melt}, C^o	1280	3600	660	1800	1080	1530
Stress limit temp. T_{st}, C^o	150	2500	140	770	180	135

The spoiler must be thick enough to separate beam halo particles from the beam. In a thick spoiler halo particles will lose enough energy to bring them on dispersion trajectories. It provides a high efficiency for separating spoiled particles from the beam. The spoiler with 2 Radiation Lengths (X_0) thickness, or 7.4 cm, is chosen, because the probability for a 50 GeV electron to travel through a 2 RL thick Ti spoiler, without losing more than 20% of its energy, is about 10^{-5} .

The temperature rise for M bunches of N electrons per bunch in the back halve of the spoiler can be calculated from a simple analytic model:

$$T = \frac{0.393NMK(\frac{\partial E}{\partial x})_{min}}{\pi\sigma_x\sigma_y C_p}, \quad (2)$$

where $(\frac{\partial E}{\partial x})_{min}$ is the electron stopping power, C_p is the specific heat of the material, the factor 0.393 describes fraction of e^- within a Gaussian beam spot area of $\pi\sigma_x\sigma_y, [cm^{-2}]$, K is the shower buildup factor.

Monte-Carlo calculations with the EGS4 code have been performed in order to determine the shower buildup factor. For a $2X_0$ thick Ti spoiler the shower buildup factor is equal to 5.

For a Ti spoiler the local temperature rise is limited by the melting of the material and must not exceed the melting point $T_{melt} = 1800C^o$.

Relation (2) combines material parameters and requirements to the beam spot size at the spoiler with the number of bunches. From (2) we obtain:

$$\sigma_x\sigma_y = \frac{0.393NM(\frac{\partial E}{\partial x})_{min}K}{\pi T_{melt}C_p}, \quad (3)$$

or $\sigma_x\sigma_y = 105M[\mu m]^2$. Supposing $\sigma_x = \sigma_y = \sigma$, for $M = 50$ bunches (it corresponds to the $\approx 4.6\mu s$ for the emergency system action) we obtain $\sigma_{x,y} = 72\mu m$. Assuming the response time for the emergency system electronic $\approx 300ns$, including the kicker rise time, and the signal velocity in the cable with the dielectric filling as a $\frac{3.0 \cdot 10^8 m}{\sqrt{2.5} s}$, one can estimate the tolerable kicker position at a distance of $\approx 825m$ from the spoiler.

After the spoiler it is necessary to install a block of material to absorb secondary particles. After consideration, copper was chosen for the absorber material. This material has a small radiation length and high electrical conductivity. These properties of *Cu* are useful to reduce the resistive wall wake-field kick.

For the *Cu* absorber the local temperature rise must not exceed four times the stress limit $4T_{st} = 720C^\circ$. The secondary particles after the spoiler are very forward-peaked, and the angular width at a half-intensity is $E_0\delta\phi = 0.1[GeV \cdot deg]$, where, $\delta\phi$ is the angular width at half intensity in degrees. The secondary beam spot size at the *Cu* absorber should exceed $250\mu m$. So, the *Cu* absorber will be damaged unless the distance between absorber and spoiler is greater than 285 cm.

The length L_a of an infinitely wide homogeneous absorber, absorbing 99% of the incident electron energy E_0 , can be estimated by the following expression [4]:

$$L_a = (1.52 \ln(E_0[MeV]) - 4.1 \ln(E_c[MeV]) + 17.6)X_0, \quad (4)$$

where E_c is the critical energy, X_0 is the radiation length of the absorber material. The radius R_a of an infinitely long cylinder absorbing 99% of incident energy must be equal to approximately 5 Moliere lengths $R_m = \frac{21.2[MeV]X_0}{E_c}$. For Copper $X_0 = 1.435cm$, $E_c = 18.8[MeV]$, and $R_m = 1.6cm$. To absorb secondaries, the *Cu* absorber is $22X_0$ thick (or 32 cm) and 8 cm in diameter.

The aperture of the absorber is chosen in a way, that the absorber is just in the shadow of the spoiler, i.e. it scrapes efficiently secondary particles but can not be hit by primaries. To minimize wake-fields, spoiler and absorber should be tapered. The optimum taper angle is estimated by using [5]

$$Q_{opt} = 1.6\left(\frac{\sigma_z\delta}{g^2}\right)^{\frac{1}{4}}, \quad (5)$$

where g is the spoiler gap, δ is the skin depth, and σ_z is the rms bunch length. In our case Q_{opt} is about 0.1 radian. The direct wake field effect measurements [9] allow to consider such choice for the spoiler and the absorber dimensions as reasonable.

2.2 Secondary particles

When a halo particle or a primary electron beam hits a spoiler, a secondary particles shower arises. Some amount of the secondary particles can be accepted by the downstream transport line and transported to the undulators. From this point of view secondary electrons and positrons are most dangerous. To estimate the efficiency of the primary particles collimation Monte-Carlo calculations by using the EGS4 code have been performed. The spoiler material and dimensions have been specified in the Section 2.1.

Despite of a shower buildup factor for the *Ti* spoiler of 5, the main amount of secondaries have a reduced energy. At Fig. 2.2.1 the energy distribution for secondary electrons is shown in the range $(5 \div 50)GeV$ supposing a primary beam with $5 \cdot 10^6$ particles distributed in a ring within diameters $(6 \div 12)mm$.

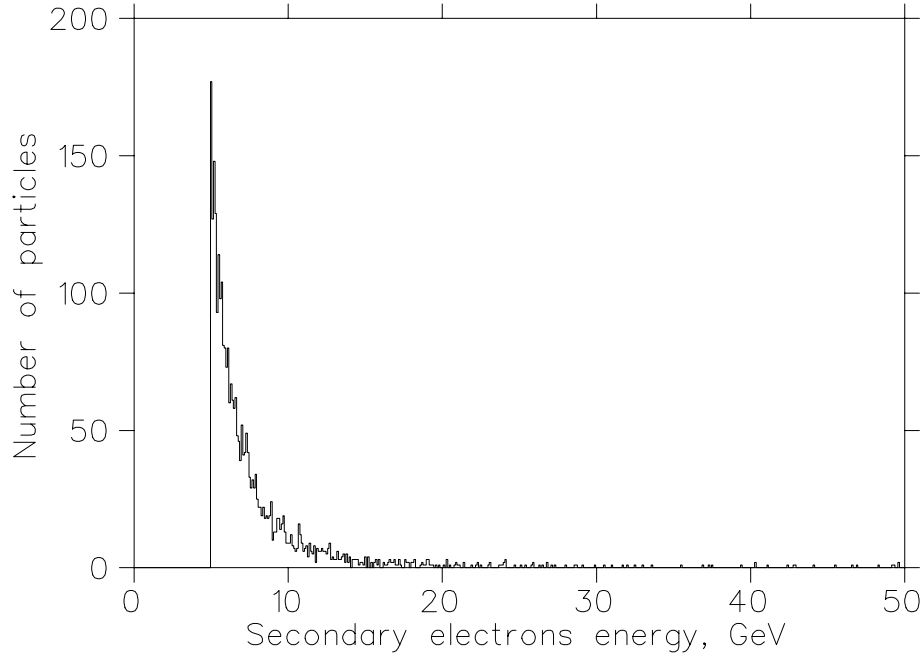


Figure 2.2.1: The energy distribution for secondary electrons in the range $(5 \div 50)GeV$ for the primary beam with $5 \cdot 10^6$ particles.

The number and the energy of secondary electrons depend also on the position of the primary beam. In Fig. 2.2.2 the secondary electron yield and energy distributions are illustrated for primary beams with $5 \cdot 10^6$ particles for different layers of the spoiler. Mostly dangerous are primary particles which hit the spoiler near the aperture.

To estimate finally the collimation efficiency, extensive simulations for the 50 GeV primary beam with $5 \cdot 10^9$ particles (total charge $0.8nC$, close to the total bunch charge of $1nC$), distributed in the ring between the diameters $(6 \div 8)mm$, have been performed. The high-energy tail of the secondary electron energy distribution is shown in Fig. 2.2.3. Not so many secondary particles are within the energy acceptance of the downstream line. To be accepted by the line, the secondaries should pass through the absorber aperture, so they should be inside a small solid angle of $\approx 2mrad$ (if there are no magnetic elements between the spoiler and the absorber). The angular distribution for secondary electrons is shown in Fig. 2.2.4. The relative amount of the secondary electrons which can be accepted by the downstream line (i.e have the energy within the energy acceptance) and the are distributed inside the solid angle $0.002rad$ is estimated as $< 5 \cdot 10^{-7}$.

From the point of view of the collimation efficiency, the spoiler thickness can be reduced to $(1.4 \div 1.5)X_0$, because the main part of secondary particles arises from the first part of the spoiler (Fig. 2.2.5). With the spoiler length reduction to $1X_0$, taking into account the practically linear energy deposition dependence for shorter than $2X_0$ spoilers, we can release requirement (3) approximately by 1.5 times. For this case the spoiler should be placed at a twice longer distance from the absorber, thus also reducing the angular acceptance of the absorber. Additionally it allows to increase the tolerable distance between the spoiler and the kicker. A further reduction of the spoiler length reduction will lead to a significant efficiency reduction, as described in [6].

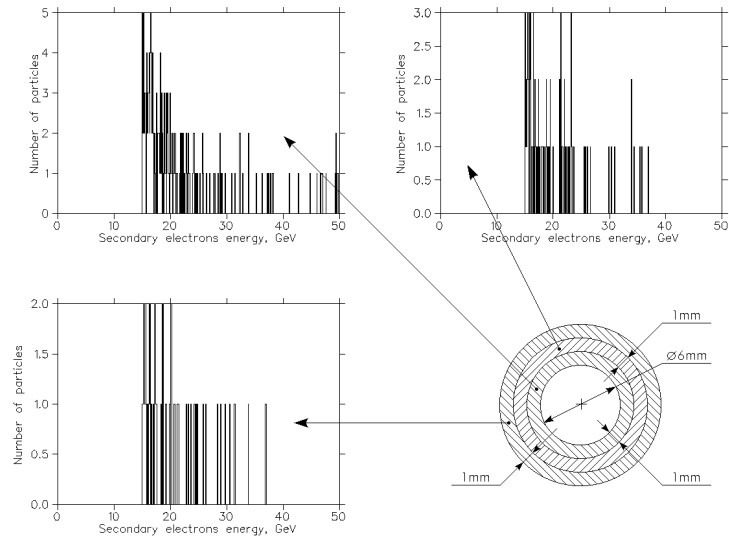


Figure 2.2.2: The energy distribution for secondary electrons from a primary beam with $5 \cdot 10^6$ particles for different spoiler layers.

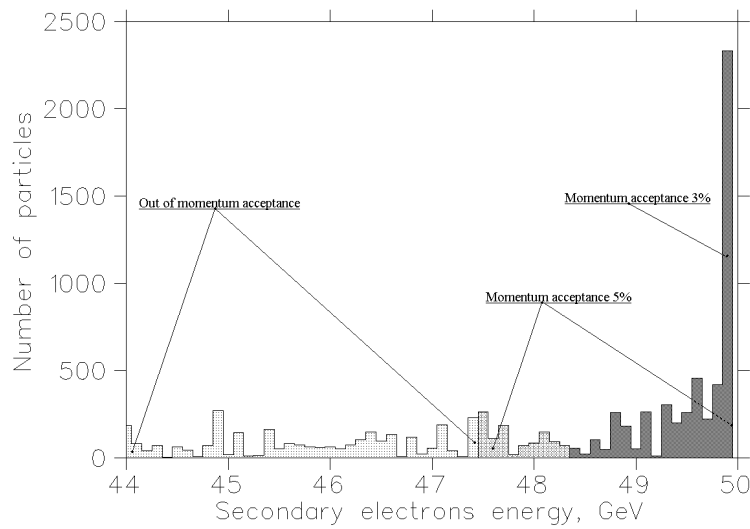


Figure 2.2.3: The high-energy tail of the secondary electron energy distribution.

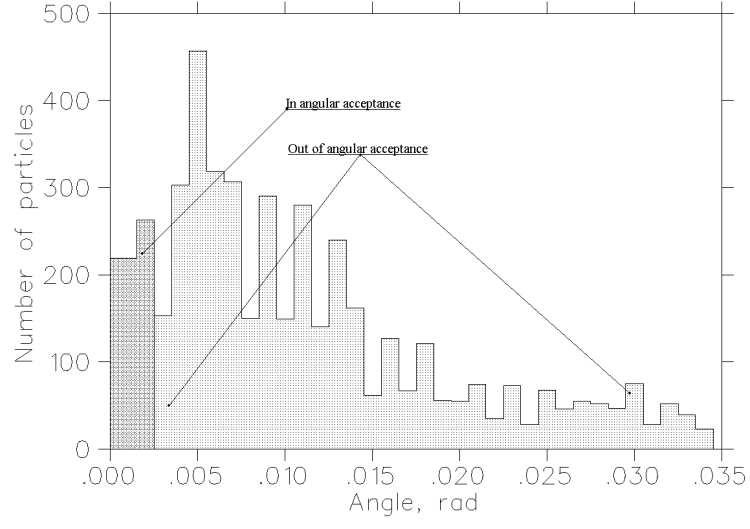


Figure 2.2.4: The angular distribution of the high-energy tail of the secondary electrons.

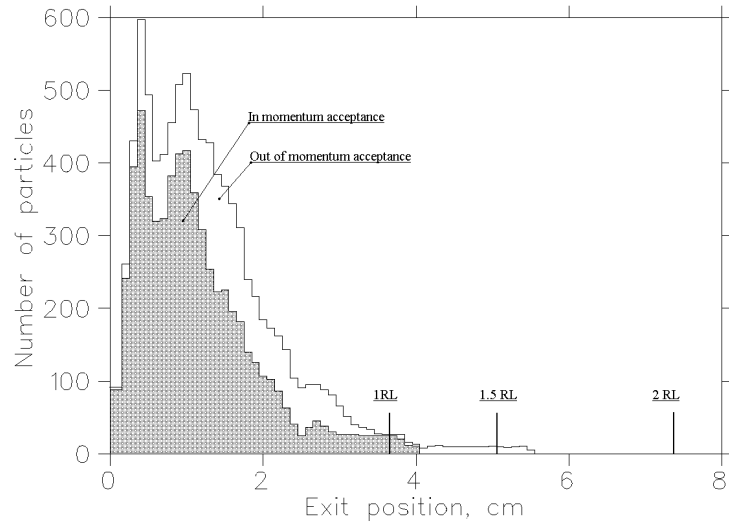


Figure 2.2.5: The exit position of high energy secondary particles.

2.3 Transverse phase space collimation

To allow a fine beam collimation in the transverse plane, the optics structure should represent a chain of cells with a definite phase advance per cell with the total phase advance of the chain equal to π . The optics functions should be large in the place of the spoiler positions, providing conditions for the spoiler survival. The length of the total chain should be reasonable and related to the emergency system response time. Different optics schemes are possible.

2.3.1 Triplet lattice

The scheme with triplets was applied at the TESLA Test Facility, is now under consideration both for the TESLA collider [1] and for the Next Linear Collider (NLC) [6]. Triplet optics ensures regions with large values of optics functions in both planes simultaneously, the chain is shorter as for other schemes and the cells are flexible in the achievable phase advance.

To understand the possibilities and the limitations, this scheme has been adopted to the FEL line parameters both in three-cell and in a four-cell option. Below a typical option is described.

Figure 2.3.1 shows the behavior of the beta functions for the three-cell triplet lattice. The phase advances are $2\pi + \pi/3$ and $\pi/3$ per cell in horizontal and vertical planes, respectively. There are three high-beta regions (for both planes). Thus this optics allows to collimate in two planes and in three iteration per each plane. The length of each cell is 150 m, that gives us the full length of the collimation section equal to 450 m. The maximum values of the beta functions in both planes are chosen to be equal to approximately 600 m. The spoilers (x and y) can be placed in the region after the weak triplet in each cell, where the values of the beta functions in both planes ($\beta_x \approx 550\text{ m}$, $\beta_y \approx 400\text{ m}$) allow to satisfy the requirements for the beam spot size at the spoilers (see Section 1.1) and even have some reserve. The cylindrical absorber is placed after each spoiler. The considered triplet lattice is flexible. By tuning of the quadrupole strengths in both triplets in the cell it is easily possible to vary the beta functions within wide bounds to obtain the needed beam size at the spoiler and to change the phase advances to organize different numbers of iterative collimation. But the considered triplet lattice has a large modulation of the beta functions in both planes, and at large values of the energy spread $> \pm 0.5\%$ such lattice has large chromatic effects.

The study confirms - the triplet scheme completely satisfies, even with some reserve in the optic functions and the total chain length, the requirements of collimation, but only for beams with narrow energy spread.

Because the energy acceptance is now an important requirement to the FEL transport line, the triplet scheme is not a good solution for the transverse collimation of the beam with the required value of the energy spread.

2.3.2 FODO lattice

The betatron collimation system has to be placed downstream of the long transfer line before the arcs which bring the beam to the surface. For the long transfer line a FODO lattice is proposed. It is logical to consider the possibility to use a FODO structure for the collimation system.

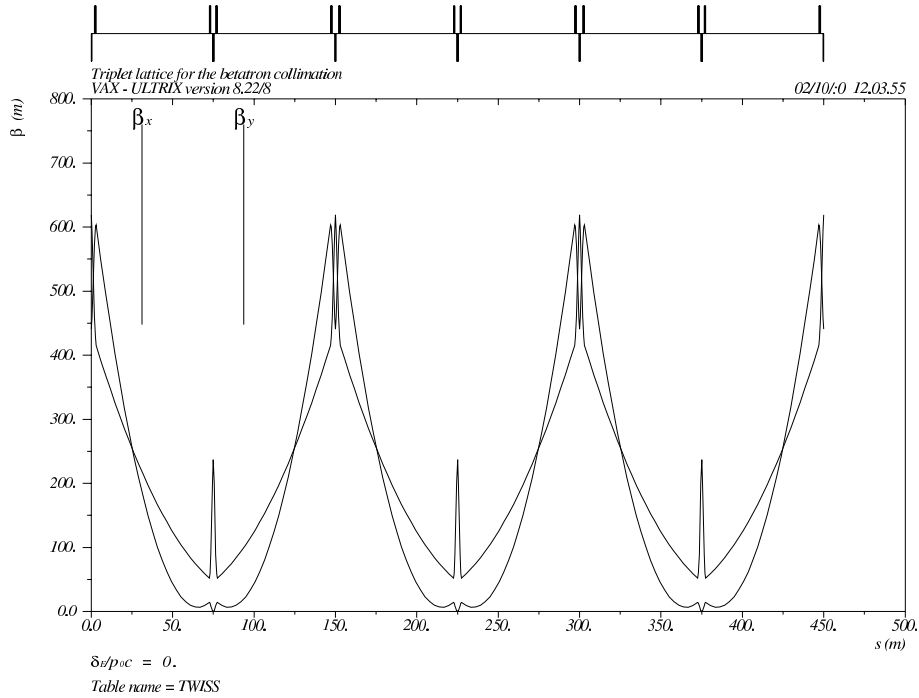


Figure 2.3.1: The optical functions for the triplet lattice for the transverse collimation.

A FODO lattice, which is very close to the lattice of the long transfer line [7], is considered. To satisfy the requirements for the beam spot size at the spoilers a FODO cell of 166 m length with a phase advances of $\pi/6$ per cell in both planes is suitable. The maximum beta function for such cell is 418 m. A weak quadrupoles with a gradient of $1.05T/m$ and effective length of $1.0m$ are used. For the FODO structure a maximum of the beta function in one direction corresponds to the minimum in the second direction. But, according to (1), we are interesting in the product $\beta_x\beta_y$, which varies along the FODO period not so strong as the beta functions. The spoilers can be placed between quadrupoles where the beam spot size at the energy of 50 GeV and the normalized emittance $\varepsilon_x = \varepsilon_y = 1.6 \cdot 10^{-6} m \cdot rad$ will be $\sigma_x\sigma_y \simeq 5245 \mu m^2$.

The full betatron collimation system will consist of 6 FODO cells of 996 m length and will collimate in two planes, with six iterations per plane. Fig. 2.3.2 shows the behavior of the beta functions for the six-cells FODO lattice.

The FODO chain also satisfies the requirements of the collimation. With the $\frac{\pi}{6}$ phase advance one can provide more precise collimation. As compared to the triplet chain with $\frac{\pi}{3}$ phase advance, the FODO chain with $\frac{\pi}{6}$ advance is twice longer. For the TESLA FEL transport system the length of the chain practically has no upper limit (it should be less than 12 km). For the protection collimation just one half of the chain is important. If the beam will hit the spoiler, it means the beam will have an off-set at the phase plane. One can check directly, four cells with phase advance $\frac{\pi}{6}$ are sufficient for the beam to meet necessarily one of four spoilers.

The FODO structure is chosen as a base option of the optic for the transverse phase space collimation.

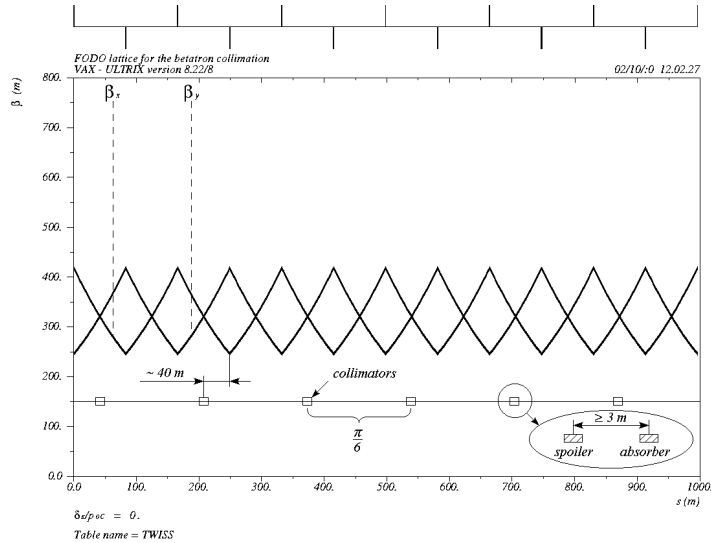


Figure 2.3.2: The optical functions of the FODO lattice for the transverse collimation.

2.4 Energy collimation

With the large momentum acceptance of the downstream arcs and the delivery system, an energy "halo" collimation has lost its importance. Only the protection energy collimation is reasonable. The energy collimation is possible at the transport line parts with nonzero dispersion. Together with a nonzero dispersion in one plane, a reasonable large beta function in the other plane should be realized to provide a tolerable beam spot-size at the spoiler. There are three possibilities for the energy collimation in the FEL transport line.

2.4.1 Collimation in the elevation arc.

There are points with a reasonably large dispersion $\approx 0.26m$ in the arcs (see Fig. 3.2.1) and the partial beam size σ_{xp} for the energy spread $\sim 2.0 \cdot 10^{-4}$ due to the dispersion is about $50\mu m$, for example, in the fourth cell of the first arc A1 (see Fig. 3.2.1). But the β_y function is very small $\beta_y \sim 6.5m$, providing a small beam spot size $\approx 50\mu m \cdot 7.5\mu m$ at the spoiler. According to (3) the spoiler will keep only three - four bunches. It is completely insufficient for the spoiler survival during the time to switch on the emergency system.

The arcs are designed for the enlarged momentum acceptance and essentially use the symmetry properties to improve it (see Chapter 3). The optics deterioration even for one arc cell (in the attempts to realize the space and optical functions required for energy collimation) leads to a symmetry deterioration and loss in the momentum acceptance of the arcs. The energy collimation in the arcs looks difficult to be realized without additional subsystems and leads to problems with the hardware survival.

2.4.2 Collimation in the extraction region.

Logically natural looks the energy collimation in the beam extraction region [7]. If something will happen and the beam will have a deviation in the energy, it is natural to

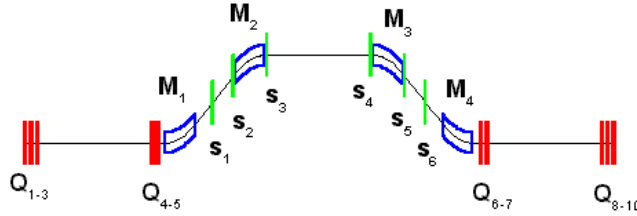


Figure 2.4.1: The possible magnetic system for the energy collimation.

collimate it as soon as possible, before passing the other parts of the transport line.

The space required $\approx (4 \div 5)m$ seems not to be a big problem for the long extraction region. The beam spot-size $\sigma_x \cdot \sigma_y \sim 80 \cdot 30 \mu m^2$ can be realized for $D_x = 0.36m, \beta_x = 65.0m, \beta_y = 50m, \epsilon_x = \epsilon_y = 1.6 \cdot 10^{-6}m$.

In this case there is no space for the emergency system, only the rf-gun switch-off can be realized.

To improve the spoiler survival, in this case one can apply either a sweep system in y direction or a "consumable spoiler" [8]. These are collimators where the jaws can be moved to a new position a finite number of times (~ 1000) after being damaged by the beam. They are suitable for use under conditions where damage will occur on occasional errant pulses. Another possibility for the spoiler improvement is the spoiler length reduction to $(1.0 \div 1.5)X_0$.

Moreover, differing from other proposals, the TESLA project is based on the application of super-conducting cavities, additionally low frequency (L-band). The energy deviation relates mainly to the behavior of the accelerating cavities. The characteristic time for super-conducting cavities is at least two orders larger as for normal-conducting cavities, all transient processes take place slowly. It means, that an energy deviation will arise in orders (as compared to normal conducting X-band or W-band colliders) slower and should be detected by other subsystems before collimation.

2.4.3 Energy collimation insertion in the long straight line.

A special structure can be designed, replacing the part of a long straight line, as it realized in [6]. But, differing from [6], this structure should have several a times enlarged momentum acceptance, equal to the momentum acceptance of the downstream arcs. It should

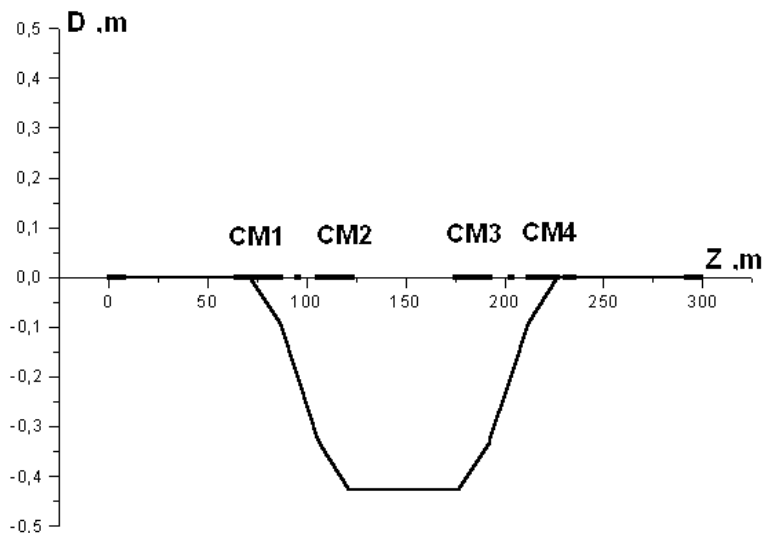


Figure 2.4.2: The dispersion function along the energy collimation system.

be pointed out, that we should try to combine in the structure logically contradictory purposes - enlarged energy acceptance and energy restriction (collimation).

The proposed scheme of such system is shown in Fig. 2.4.1. This system is a first order achromat with the total length of 300m and provides the unit $+I$ beam transformation. To prevent the energy spread growth and the emittance dilution 15 m long dipole magnets (as in the beam delivery system, Chapter 4) with a field of 0.13 T are applied. Two bending magnets $M1$ and $M2$ provide a beam displacement of a distance of 0.4 m and the magnets $M3$ and $M4$ return it to the reference axis. The dispersion function along the system is shown in Fig. 2.4.2 and the rms beam envelopes are shown in Fig. 2.4.3. As one can conclude, the beam spot size at the reference energy is sufficient for the spoiler survival. The space of $\approx 50m$ between magnets $M1$ and $M2$ is sufficient for the spoiler and the absorber placement. In the first order consideration this scheme totally satisfies the energy collimation requirements. The correction of second order effects is performed by the sextupoles $S1 \div S6$. With this correction no beam size growth appears in the y direction, but by ≈ 2 times in the dispersive direction, assuming $\pm 5\%$ average energy deviation. Because this effect is nonlinear, the system has acceptable parameters for a smaller deviation $\approx \pm 1\%$. To improve the energy acceptance up to $\pm 3\%$ the scheme needs more development.

As one can see from Fig. 2.4.3, the beam spot size between magnets $M2$ and $M3$ decreases with an energy offset of -5% . To ensure the spoiler survival conditions, a y -sweeping system should be installed in this drift region.

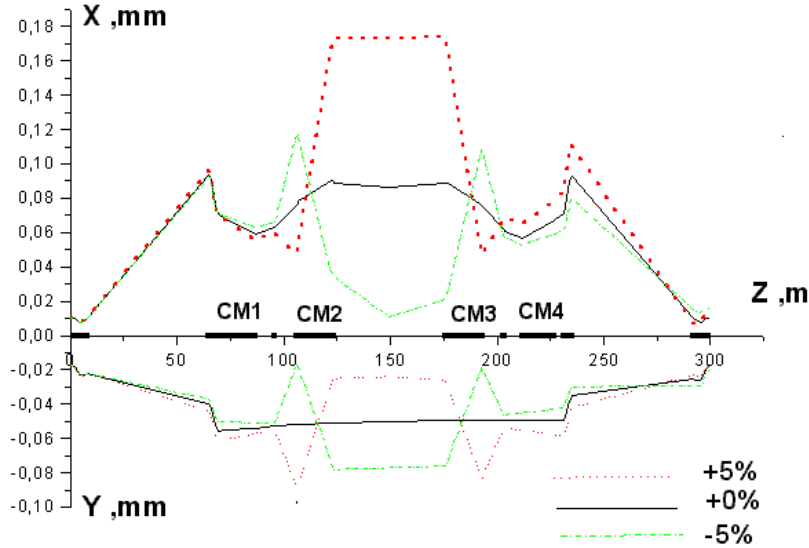


Figure 2.4.3: The beam envelopes along the energy collimation system.

2.4.4 The implementation of the sweeping system

Another way to improve the spoiler survival is a fast sweeping system. If the spoiler can withstand a few bunches, this system should be placed close enough to start a beam sweeping, thus increasing the effective beam spot size and providing a reserve in time for the activation of the emergency system. The efficiency of a such method depends on a deflection angle value after a kicker and an optics between the kicker and the spoiler.

Suppose the fast kicker is the same as for the fast feedback system, providing a beam deflection of $0.6\mu rad$ for a $50 GeV$ beam.

In the optics scheme for the energy collimation (see Section 2.4.4) such a kick after the bend magnet $M2$ results in a $\pm 25\mu m$ bunch shift at the spoiler (before the bend magnet $M3$), improving the spoiler survival conditions.

Such system can be considered for the spoiler survival improvement also for the energy collimation in the arc. We need to increase the effective beam spot size in the y direction. The beam displacement before the first focusing element is $\sigma_d = \phi l_d$, where ϕ is the kicker deflection angle, l_d is the drift length. At the plane of the foqucing element we can describe the effective beam size as $\sigma_d + \sqrt{\beta_y \epsilon_y}$ and the corresponding "effective" beam emittance ϵ_y^e :

$$\epsilon_y^e = \frac{(\sigma_d + \sqrt{\beta_y \epsilon_y})^2}{\beta_y}, \quad (6)$$

which will be transported by the foqucing system and transformed to the effective spot size at the spoiler.

According to (6), to have a significant increase of the spot size, we need in a large drift and a small beta function in the first lens after the kicker. The optics of the arcs is very

tight (see Chapter 3). Only shortened kicker with a length of 0.3 m can be placed into the existing scheme, and only a 6 m long drift is available. With such parameters the beam shift is only $12\mu\text{m}$, compared with a natural beam size of $7.5\mu\text{m}$, can be obtained. The sweeping system implementations provides a beam spot size increase, but one reduced fast kicker is not sufficient for the improvement of the spoiler survival. An application of several shortened fast kickers in upstream cells of the arc or combination of a fast weak kicker and a slower enforced kicker should be investigated additionally.

2.5 Radiation dose estimations.

The equivalent neutron component dose H_n estimation is based on a model described in [11] and is given by the following equation:

$$H_n = E_0 \frac{\cos^2 b}{L^2} \cdot 10^{-13} (13.69 A^{-0.65} e^{\frac{-dq}{l_1 \cos b}} (1 - 0.72 \cos w)^{-2} + \frac{44.3 A^{-0.37} e^{\frac{-dq}{l_2 \cos b}}}{1 - 0.75 \cos w} + 4.94 Z^{0.66} e^{\frac{-dq}{l_3 \cos b}}) \quad (7)$$

H_n is the equivalent neutron dose in [Sv] per electron, E_0 is the electron energy in GeV, L is the distance between the target and the shield surface, d is the shield thickness, w is the angle between the beam direction and the line connecting the target to the measurement point, b is the angle between the latter line and the normal to the shield from the target. Angles are in degrees, and distances are in [cm]. Z is the atomic number and A is the atomic mass number for the target material.

The three terms in the above equation represent the production and attenuation of High-Energy Neutrons (HEN), Mid-Energy Neutrons (MEN) and Giant Resonance Neutrons (GRN). Fluence-to-dose conversion factors of $6.7 \cdot 10^{-10} [\frac{\text{Sv}}{\text{cm}^2}]$ per neutron for HEN, $3.2 \cdot 10^{-10}$ for GRN and MEN were used in deriving the above equation. In these estimations the attenuation lengths in concrete ($q = 2.35 [\frac{\text{g}}{\text{cm}^3}]$) for HEN, MEN and GRN are $l_1 = 120 [\frac{\text{g}}{\text{cm}^2}]$, $l_2 = 55 [\frac{\text{g}}{\text{cm}^2}]$ and $l_3 = 30 [\frac{\text{g}}{\text{cm}^2}]$, respectively.

Corrections with appropriate attenuation lengths were applied for the attenuation in copper targets as well.

Without shielding the equivalent neutron dose component is given by the following equation:

$$H_n = E_0 \cdot 10^{-13} \frac{13.69 A^{-0.65} (1 - 0.72 \cos w)^{-2} + \frac{44.3 A^{-0.37}}{1 - 0.75 \cos w} + 4.94 Z^{0.66}}{r^2} \quad (8)$$

The equivalent photon dose H_{ph} (in [Sv] per electron) is given by the following equation [11]:

$$H_{ph} = E_0 \frac{\cos^2 b}{L^2} \cdot 10^{-13} (1.26 \cdot 10^6 E_0 e^{-tq m_1 - w^{0.6}} (1 - H_1) + 755 H_1 e^{-Rq m_1 - 1.4w}) e^{\frac{-dq m_2}{\cos b}}, \quad (9)$$

where m_1 and m_2 are the mass attenuation coefficients at the Compton minimum for the target and the shield materials, t is the target thickness and R is the target radius in cm. The values of $1/m$ for concrete and copper are 42.0 and $33.0 [\frac{\text{g}}{\text{cm}^2}]$, respectively. $H_1 = 1$ for $w > 5$ degrees and $= 0$ for $w < 5$ degrees. Without shielding:

$$H_{ph} = E_0 \cdot 10^{-13} (1.26 \cdot 10^6 E_0 e^{-w^{0.6} - tq m_1} (1 - H_1) + 755 H_1 e^{-Rq m_1 - 1.4w}) r^{-2} \quad (10)$$

Table 2.7.1: The distance (in meters) from the absorber to the points of the equal equivalent dose $H_t = 10$ [Sv] per year.

w , degree	1 W	10 W	100 W	1000 W
0	46.1	146	461	1460
2	43.1	136	431	1360
4	41.7	132	417	1320
10	4.25	13.44	42.5	134.4
20	3.97	12.55	39.7	125.5
40	3.44	10.88	34.4	108.8
60	3.06	9.68	30.6	96.8
80	2.81	8.89	28.1	88.9
100	2.65	8.38	26.5	83.8
120	2.55	8.06	25.5	80.6
140	2.48	7.84	24.8	78.4
160	2.45	7.75	24.5	77.5
180	2.43	7.68	24.3	76.8

The total equivalent dose is $H_t = H_n + H_{ph}$ (in [Sv] per electron). In our case:

$$H_t = 5 \cdot 10^{-12} \left(\frac{0.92}{(1 - 0.72 \cos w)^2} + \frac{9.53}{1 - 0.75 \cos w} + 45.59 + 1.88 \cdot 10^4 e^{-w^{0.6}} (1 - H_1) + (11) \right. \\ \left. + 86.64 H_1 e^{-1.4w} \right) r^{-2},$$

Table 2.7.1 presents the distances between the target and the points of equal total dose equivalent $H_t = 10$ [Sv] per year corresponding to different constant beam losses.

A 1 m thick concrete shield around absorber will decrease the total equivalent dose for angles between 5 and 60 degrees about 20 times, for angles between 60 and 180 degrees about 200 times and for angles between 0 and 5 degrees about 270 times.

In Fig. 2.6.1 the typical iso-dose contour corresponding to the total dose 10 [Sv] per year for 1W average beam losses power is shown. Fig. 2.6.2 represents the iso-dose contours for different average beam losses power. This value (10 [Sv] per year) is a practical limit for some kind of electronic devices.

Residual induced activity.

The dose rate must not exceed $100 \left[\frac{mrem}{h} \right]$ at a distance of 1 m near the absorber. Radionuclides mainly produced in the *Cu* absorber are $Cu_{61}, Cu_{62}, Cu_{64}$. For the *Cu* absorber an estimation of the dose rate can be made, by using the expression [12]:

$$\frac{dH}{dt} = \frac{1.4 \cdot 10^{-10} E_0 \frac{dN}{dt}}{r^2}, \quad (12)$$

where $\frac{dH}{dt}$ is the dose rate in $\left[\frac{mrem}{h} \right]$, E_0 is the electron energy in GeV, r is the distance in m, $\frac{dN}{dt}$ is the number of electrons per second. For these requirements $\frac{dN}{dt}$ for the *Cu* absorber must not exceed $14 \cdot 10^{10}$, or average beam losses must not exceed 110 W.

2.6 Summary

The titanium spoiler together with the copper absorber are chosen as a collimator for the FEL transport line. The spoiler with 1.5 radiation length thickness withstand 70

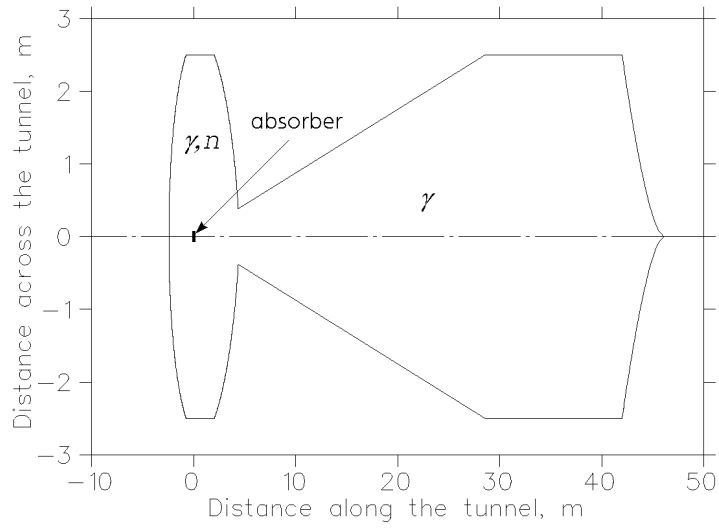


Figure 2.6.1: The typical iso-dose contour corresponding to the total dose 10 [Sv] per year for 1W average beam losses power.

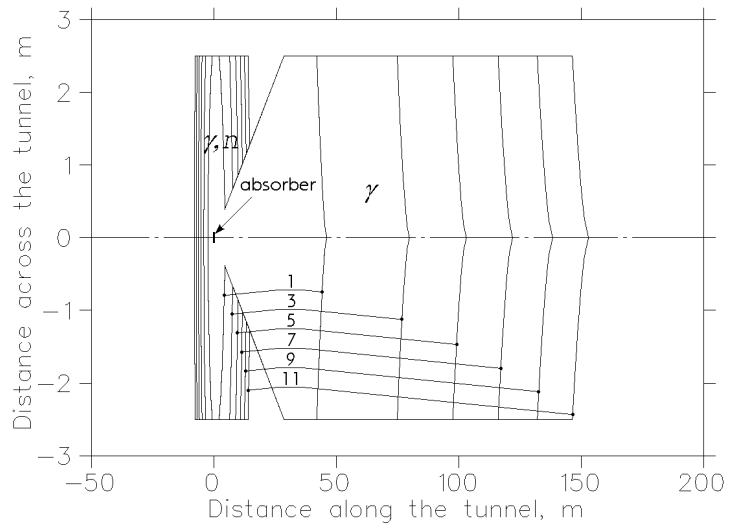


Figure 2.6.2: The iso-dose contours for different average beam losses power.

bunches with a spot size $\sigma_x \cdot \sigma_y \approx 72\mu m \cdot 72\mu m$. A copper absorber of 22 radiation length thickness should be placed at a distance of 6m behind the spoiler and is sufficient for the absorption of the secondary particles. The collimation efficiency is at least 10^{-6} if there are no focusing elements in between. The radiation dose distribution is estimated together with the safety requirements.

A FODO optics scheme is chosen for the transverse energy collimation combining the collimation efficiency, spoiler survival conditions and energy acceptance requirements.

A special optics for energy protection collimation is recommended.

3 Elevation of the beam to ground level

3.1 General requirements

This section discusses the problem of the elevation of the beam from the tunnel level to the ground level. The magnet lattice of this elevation system has to fulfill a number of requirements, both in terms of beam dynamics as well as geometry considerations. The general design requirements are:

- Provide a horizontal angle of about 10° between the linac and the mean axis of the user beam lines.
- Provide a vertical displacement of the beam for a distance of 15.154 m for a high energy beam line.
- Provide the protection of the wood area: the beam has to be under this wood area at a distance not smaller 6.8 m (between the beam and the ground level).
- Provide the required value of the energy acceptance.
- Introduce no significant transverse emittance dilution and additional energy spread.

Item 4 requires the design of the magnet optics of the total elevation system which allows to let pass the bunch train with an energy offset of different bunches in the train which is not smaller $\pm 3\%$. A more larger value of the energy acceptance is welcome.

Synchrotron radiation in bending magnets increases the transverse emittance, if the dispersion is nonzero, and the energy spread of the bunch. For the estimation of this effect the analytical formulae [1] are used. The particle beam which passes a bending magnet gains an additional rms energy spread of the value

$$\sigma_E = \sqrt{\frac{55C_\gamma \hbar c (m_0 c^2)^4}{32\pi\sqrt{3}}} \gamma^7 \frac{L_B}{\rho_B^3} = 1.94 \cdot 10^{-14} [MeV m] \sqrt{\gamma^7 \frac{L_B}{\rho_B^3}}. \quad (13)$$

The increase of the transverse beam emittance is

$$\Delta(\varepsilon\gamma) = \frac{55C_\gamma \hbar c (m_0 c^2)^2}{64\pi\sqrt{3}} \gamma^6 \frac{L_B}{\rho_B^3} H = 4.04 \cdot 10^{-8} \left[\frac{m^2}{GeV^6} \right] E^6 \frac{L_B}{\rho_B^3} H. \quad (14)$$

with

$$H = \frac{1}{L_B} \int_0^{L_B} \frac{1}{\beta(s)} \left(D(s)^2 + (\beta(s)D(s)' + \alpha(s)D(s))^2 \right) ds \quad (15)$$

where

$$C_\gamma = \frac{4\pi}{3} \frac{r_c}{(m_0 c^2)^3} = 8.8575 \cdot 10^{-5} \left[\frac{m}{GeV^3} \right]$$

is the radiation constant. \hbar is the Planck constant, c is the speed of light, m_0 is the electron mass, $\gamma = \frac{E}{m_0 c^2}$ is the Lorentz factor, E is a full particle energy, L_B is the length of the bending magnet, ρ_B is the bending radius, $\beta(s)$, $\alpha(s)$ are optical functions of the beam, $D(s)$ is the dispersion. Consequently, the last item results in a large bending radius of dipole magnets and in a matching of the optical functions to minimize the function H . In the proposed design the horizontal deflection and vertical displacement are separated and provided with the help of four identical arcs. The top and side views of the elevation system are shown in Fig. 3.1.1.

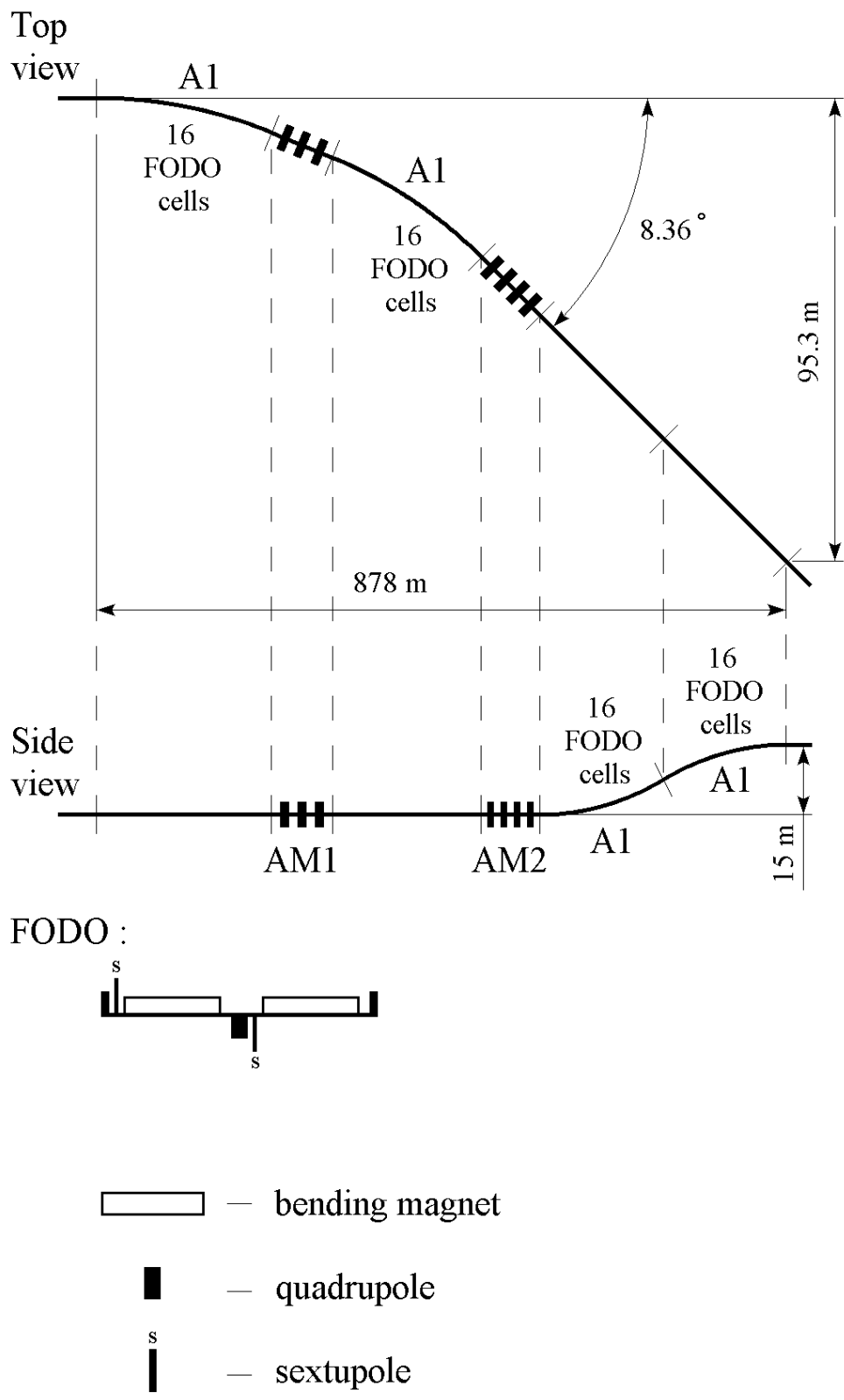


Figure 3.1.1: Schematic layout of the elevation system.

3.2 Design of arcs

The total elevation system of the beam from the tunnel to the ground level consists of the horizontal arc, the vertical arc and the matching section between them. The main parameters of the arcs are listed in Tables 3.2.1 - 3.2.5.

Both horizontal and vertical arcs are designed using the same A1 base arc. The design of the A1 arc is based, on the one hand, on geographical considerations of the experimental area for the beam distribution system, and on the other hand, on the beam dynamics properties: to provide the energy acceptance for the bunch train. The geometry considerations give us the requirement to organize the fast rise of the beam on the ground level for the protection of the wood area simultaneously minimizing the distance between the wood area and the point of the beam exit on the surface. The minimization of the distance is in some contradiction with the requirement to minimize the additional energy spread. Taking into account both requirements a bending radius of 2061.45 m has been chosen for the dipole magnets. Then according to formula (13) the additional energy spread in the A1 base arc will be $\sigma_E = 0.34 \text{ MeV}$ at the 40 GeV energy. In the proposed design within the distance of 200 m between the wood area and the beam exit on the surface the beam is lowered for 6.8 m that is the required value. In this case a distance of 800 m remains for the beam distribution lines to different users.

In terms of beam dynamics the A1 base arc consists of 16 FODO cells and has a length of 208.6 m. In both transverse planes the A1 arc constitutes a second-order achromat and has a mirror symmetry with respect to the center. The phase advances in both planes are chosen to obtain the second-order achromat. They are $\nu_x = 2$, $\nu_y = 3$ for the horizontal A1 arc and vice versa for the vertical one. A total of 32 sextupoles arranged in two families are positioned in all FODO cells. So two from four free spaces (the length of which is 0.51 m) in each FODO cell are occupied by two sextupoles. The another two free spaces may be used for the correcting elements. The parameters of the A1 base arc are listed in Table 3.2.1. According to formula (14) the transverse emittance dilution in the A1 base arc will be $\Delta(\varepsilon\gamma)/\varepsilon_n = 0.21\%$ at the energy of 40 GeV (in the assumption that the normalized emittance $\varepsilon_n = 1.6 \cdot 10^{-6} \text{ mrad}$).

Each arc, horizontal and vertical, is constructed from two A1 base arcs, which are second-order achromats, using additionally different types of symmetries to provide the required value of the energy acceptance for the bunch train. The horizontal arc consists of two A1 arcs with a special section between the arcs the transverse matrix of which is a minus identity matrix. The -I section contains 4 quadrupole magnets. The parameters of the horizontal arc are listed in Table 3.2.2. The horizontal arc provides the deflection angle of 8.36° between the linac and the mean axis of the distribution beam lines that satisfies the geometry requirements for the experimental area. The vertical arc is constructed from the same A1 arcs. The vertical A1 base arc is obtained by the rotation of the horizontal A1 arc by an angle of 90° . Two vertical A1 arcs are connected together to organize the rise of the beam to the ground level. The vertical arc provides the vertical displacement of the beam for the required height of 15.154 m (for the high energy beam). There is an AM2 matching section between the horizontal and vertical arcs. The proposed lattice of the total arc, horizontal and vertical together (see Table 3.3.5), fulfills the general design requirements. The question of the energy acceptance is discussed in the next section.

Fig. 3.2.1-3.2.2 show the optical functions along the horizontal and vertical arcs.

Table 3.2.1: Parameters of the A1 base arc.

	Value	Unit
Length	208.6	m
Number of FODO cells	16	
Horizontal deflection	7.6	m
Horizontal deflection angle	4.18	degree
Total number of dipoles	32	
Length of each dipole	4.7	m
Bending radius of each dipole	2061.45	m
Total number of quadrupoles	32	
Length of each quadrupole	0.8	m
Quadrupole strengths		
HQF	+0.176	$1/m^2$
HQD	-0.207	$1/m^2$
Total number of sextupoles	32	
Length of each sextupole	0.2	m
Sextupole strengths		
HSF	+6.15	$1/m^3$
HQD	-10.94	$1/m^3$
Maximum horizontal β -function	27.83	m
Maximum vertical β -function	20.03	m
Maximum horizontal dispersion	0.26	m
Momentum compaction R_{56}	-0.0075	m
Additional energy spread at 40 GeV	0.34	MeV
Transverse emittance dilution at 40 GeV	0.21	%

Table 3.2.2: Parameters of the horizontal arc.

	Value	Unit
Total length	458.46	m
Number of A1 arcs	2	
Horizontal deflection	33.39	m
Horizontal deflection angle	8.36	degree
Length of -I section	41.26	m
Quadrupoles number in -I section	4	
Length of each quadrupole	0.8	m
Quadrupole strengths in -I section		
HQFF	+0.176	$1/m^2$
HQDF	-0.176	$1/m^2$
Maximum horizontal β -function	43.76	m
Maximum vertical β -function	35.12	m
Maximum horizontal dispersion	0.26	m
Momentum compaction R_{56}	-0.015	m
Additional energy spread at 40 GeV	0.48	MeV

Table 3.2.3: Parameters of the vertical arc.

	Value	Unit
Total length	417.2	m
Number of A1 arcs	2	
Vertical displacement	15.154	m
Maximum horizontal β -function	20.03	m
Maximum vertical β -function	27.83	m
Maximum vertical dispersion	0.26	m
Momentum compaction R_{56}	-0.015	m
Additional energy spread at 40 GeV	0.48	MeV

Table 3.2.4: Parameters of the AM2 matching section.

	Value	Unit
Total length	8.88	m
Number of quadrupoles	4	
Length of each quadrupole	0.8	m
Quadrupole strengths		
QF1	+0.033	$1/m^2$
QD1	-0.100	$1/m^2$
QF2	+0.100	$1/m^2$
QD2	-0.033	$1/m^2$
Maximum horizontal β -function	27.83	m
Maximum vertical β -function	27.83	m

Table 3.2.5: Parameters of the total arc.

	Value	Unit
Total length	884.54	m
Number of A1 arcs	4	
Horizontal deflection	95.3	m
Vertical displacement	15.154	m
Horizontal deflection angle	8.36	degree
Total number of dipoles	128	
Total number of quadrupoles	128 + 8	
Total number of sextupoles	128	
Maximum horizontal β -function	43.76	m
Maximum vertical β -function	35.12	m
Maximum horizontal dispersion	0.26	m
Maximum vertical dispersion	0.26	m
Momentum compaction R_{56}	-0.03	m
Additional energy spread at 40 GeV	0.68	MeV

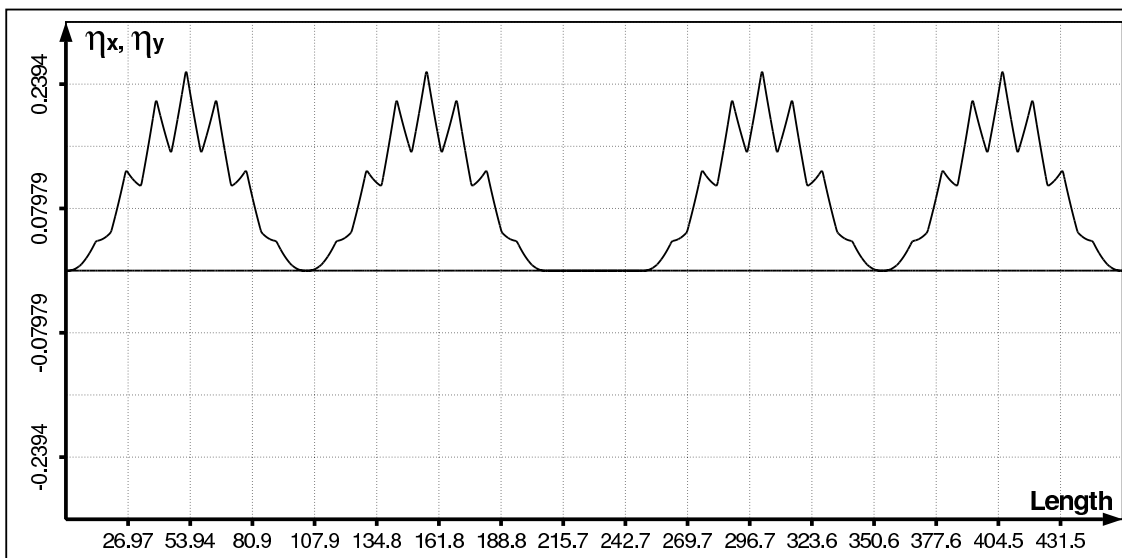
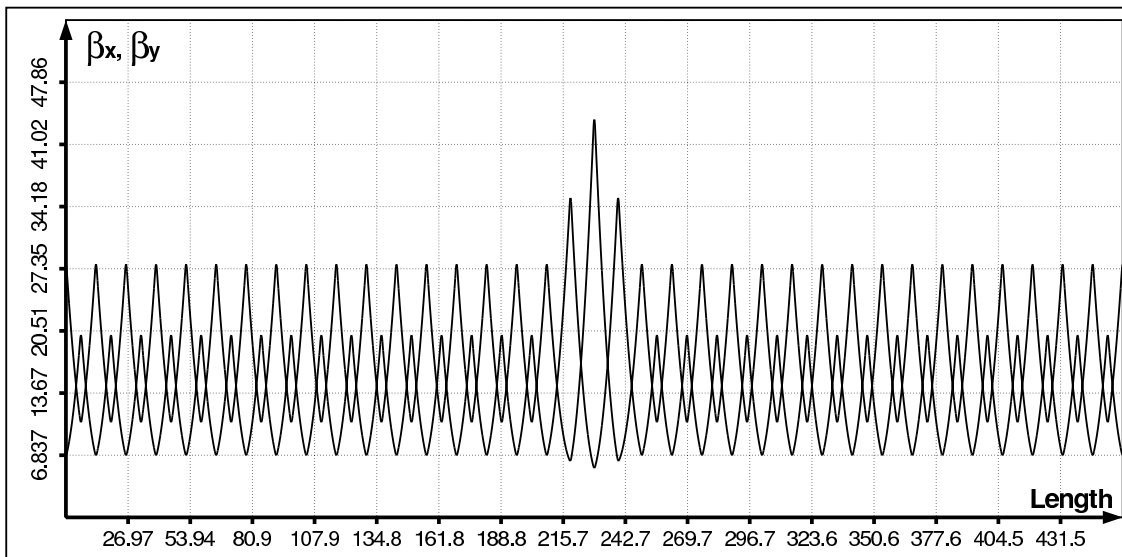


Figure 3.2.1: Behavior of dispersion and beta functions along the horizontal arc.

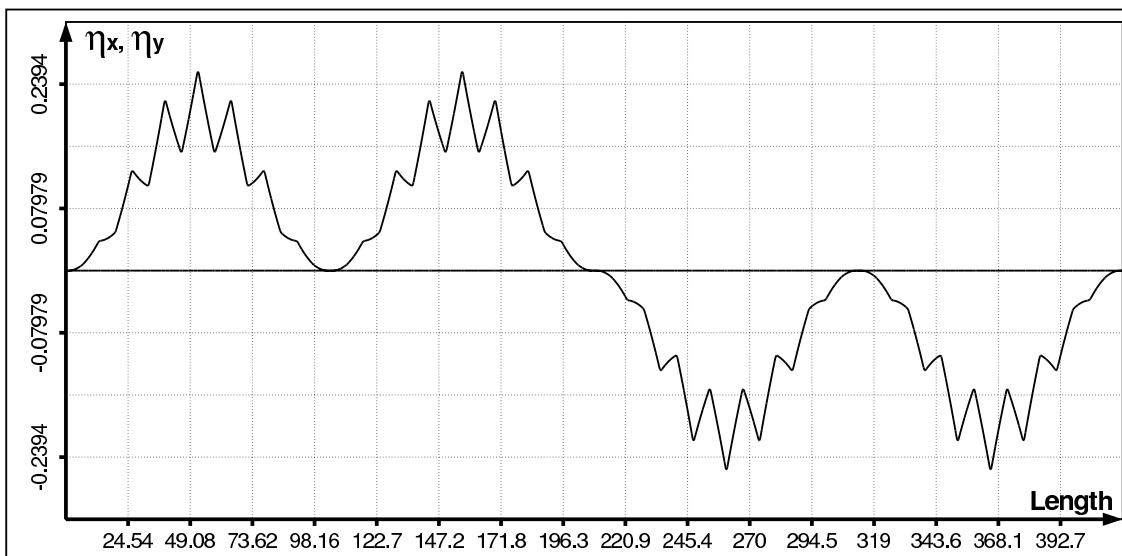
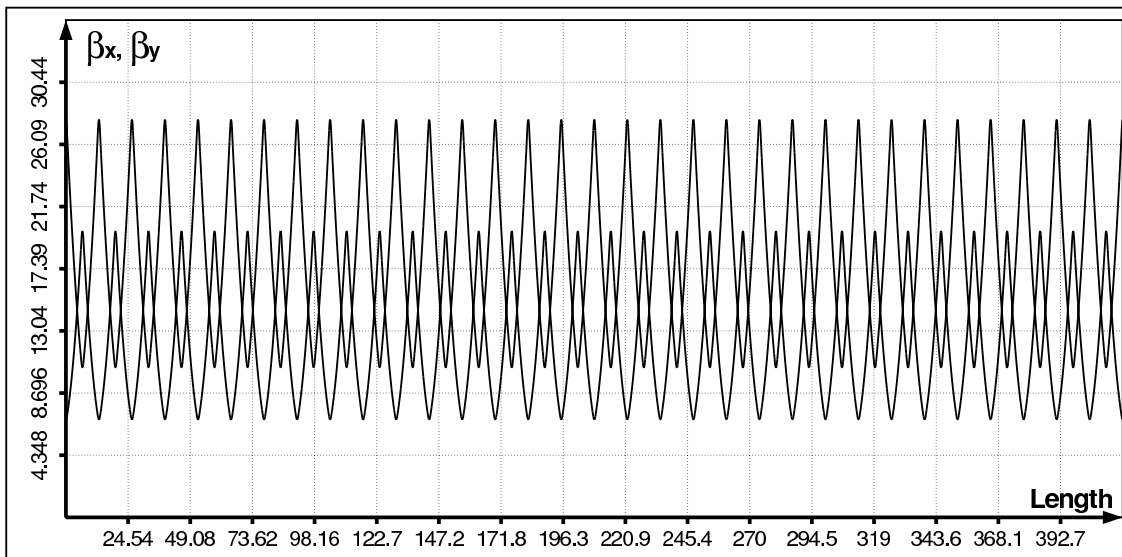


Figure 3.2.2: Behavior of dispersion and beta functions along the vertical arc.

3.3 Tracking studies

One of the requirements in the arc design is the provision of the energy acceptance for the proposed lattice. Beam dynamics studies have been carried out to define the value of the energy acceptance of the proposed arc for the elevation system. These studies have been done with the orbit-tracking and mapping modules of the program TrackFMN [32]. Additional optics analysis tools and procedures have been developed in the process. For the tracking and mapping studies the non-expanded Hamiltonian is used in a SCOFF approximation.

At the present stage the analysis of the magnet lattice without misalignments and field errors has been done. For the analysis of the arc lattice with the point of view of the energy acceptance, the following tracking investigations are made. The particles, which are initially distributed uniformly along the perimeter of the phase space ellipses corresponding to the rms normalized emittance $\varepsilon_{x,y} = 1.6 \cdot 10^{-6} m \cdot rad$, are tracked through the considered optics. Three phase space ellipses with the same value of the transverse emittance are set: the energy spread of particles on one ellipse is zero, on the second ellipse is $+n\%$ and on the third ellipse is $-n\%$. In the starting point these ellipses coincide. In the final point a comparison of the location of these ellipses is made. The value of the energy spread $\pm n\%$ at which both ellipses (with $+n\%$ and $-n\%$) coincide (or almost coincide) with the phase space ellipse of particles with zero energy spread (with the phase space ellipse of particles with the nominal energy), is defined as the energy acceptance of the considered beam line.

Fig. 3.3.1-3.3.3 show the transverse phase space plots of the tracking results for the horizontal, vertical and both arcs together at an energy of 20 GeV. The top figures are the phase space plots in the horizontal and vertical planes at the entrance of the considered beam lines. The bottom figures are the phase space plots at the exit of the lines.

The tracking results show that the energy acceptance of the horizontal arc achieves a value of $\pm 5\%$ (see Fig. 3.3.1). The energy acceptance of the vertical arc is larger approximately by two times (see Fig. 3.3.2). The energy acceptance of the total arc is $\pm 5\%$ (see Fig. 3.3.3). Fig. 3.3.4 shows the trajectories of particles in four bunches with different energy offset ($\pm 3\%$, $\pm 5\%$) along the total arc. The inner trajectories are for bunches with the $\pm 3\%$ energy offset. We see that the maximum value of the bunch trajectory shift in the arc is approximately $\pm 0.013 m$ for a $\pm 5\%$ energy offset.

3.4 Summary

The proposed magnet lattice for the elevation of the beam from the tunnel level to the ground level fulfills the general design requirements, both in terms of beam dynamics as well as geometry considerations. The horizontal deflection and vertical displacement are separated in the proposed design and provided with the help of four identical arcs. The horizontal arc consists of two A1 base arcs with the -I section between them and gives the horizontal angle of 8.36° between the linac and the mean axis of the distribution beam lines that satisfies the geometry considerations for the experimental area. The vertical arc, which is also constructed from two A1 base arcs, provides the vertical displacement of the beam on the ground level for the required height of 15.154 m (for the high energy line). At the present stage the analysis of the magnet lattice of the total arc without misalignments and field errors has been done. The tracking results show that the energy

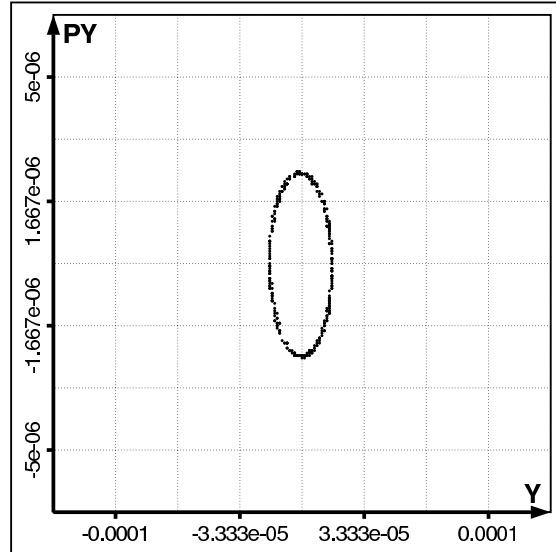
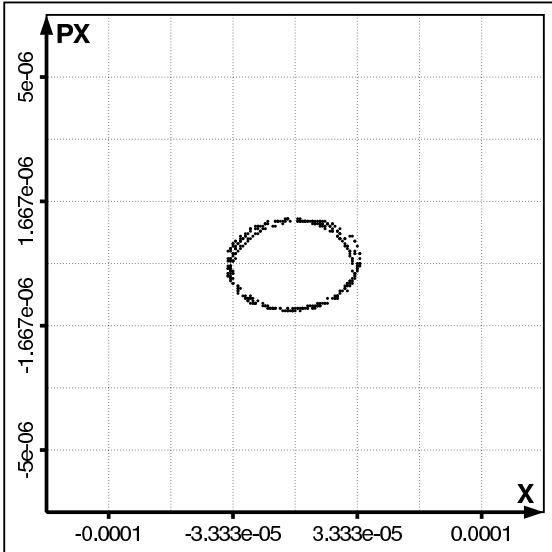
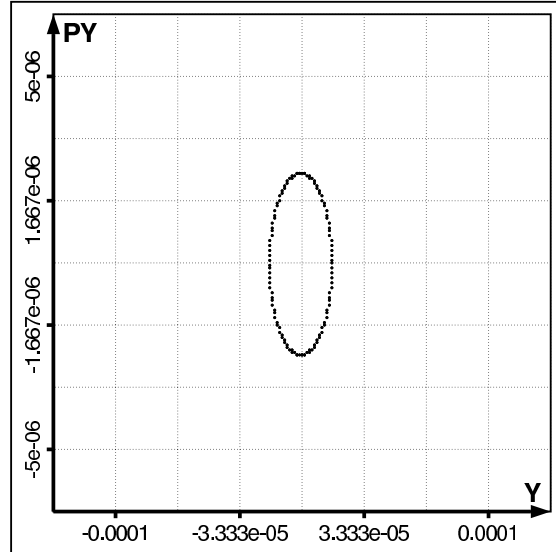
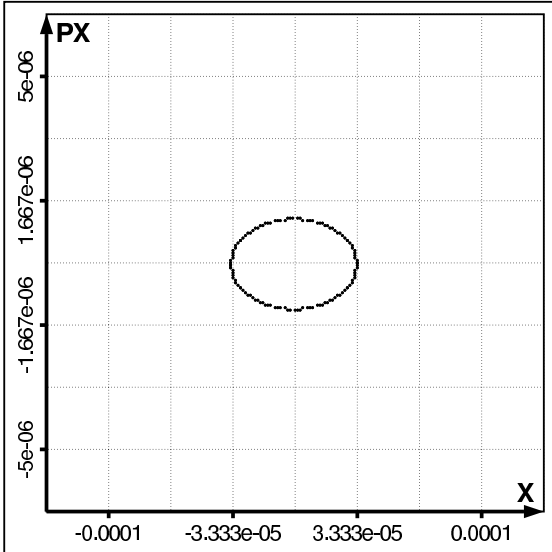


Figure 3.3.1: Tracking results for the horizontal arc. The energy spread is $\pm 5\%$.

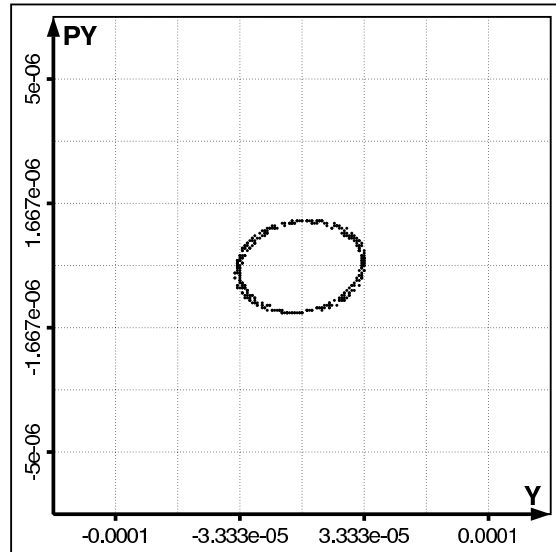
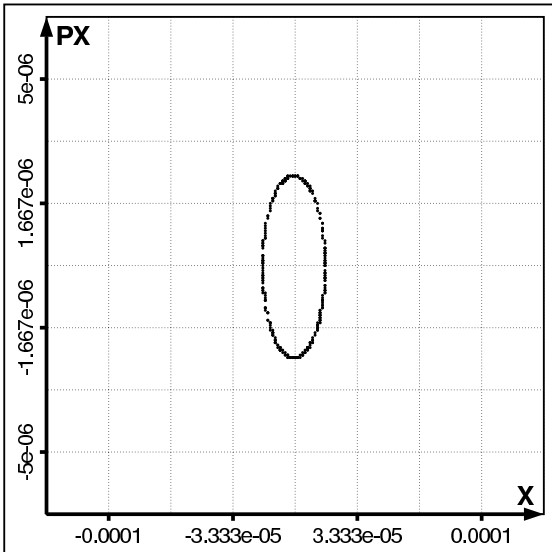
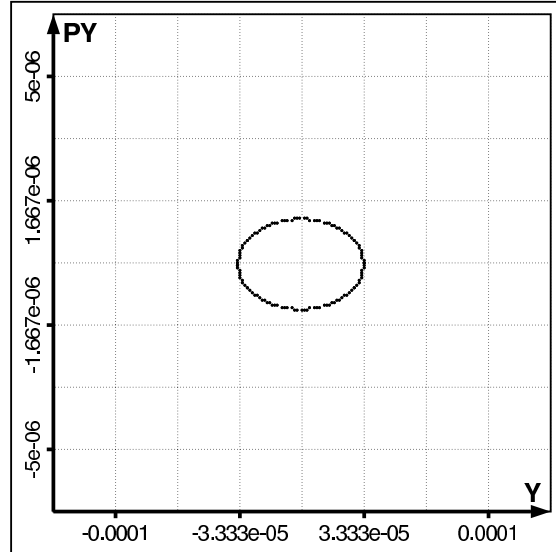
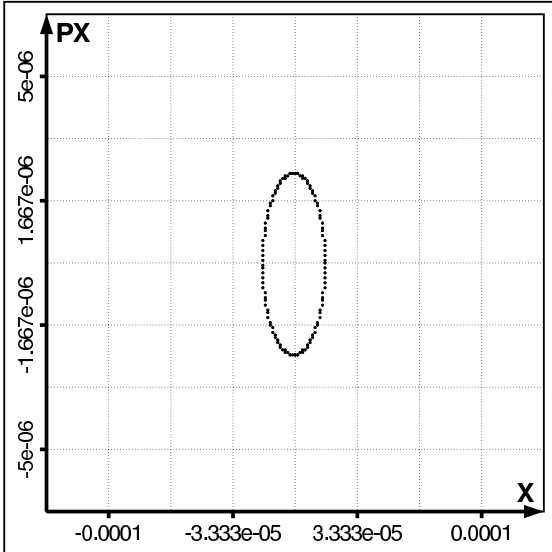


Figure 3.3.2: Tracking results for the vertical arc. The energy spread is $\pm 10\%$.

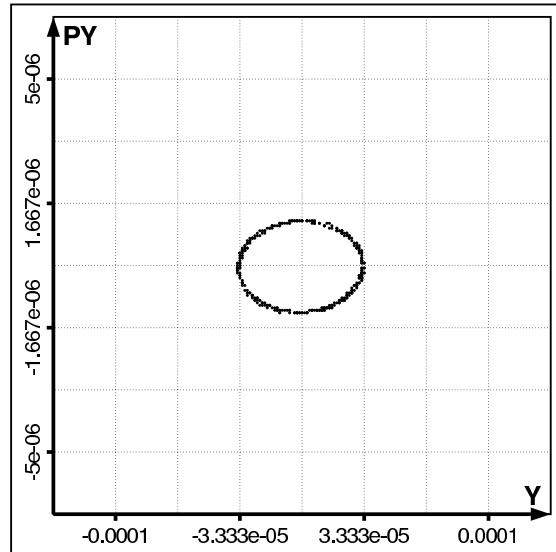
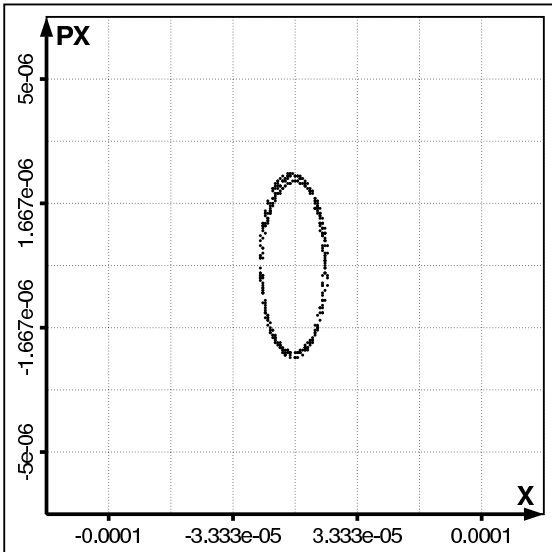
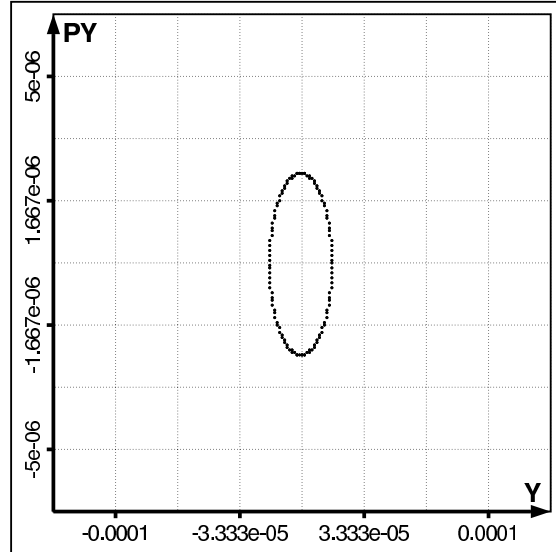
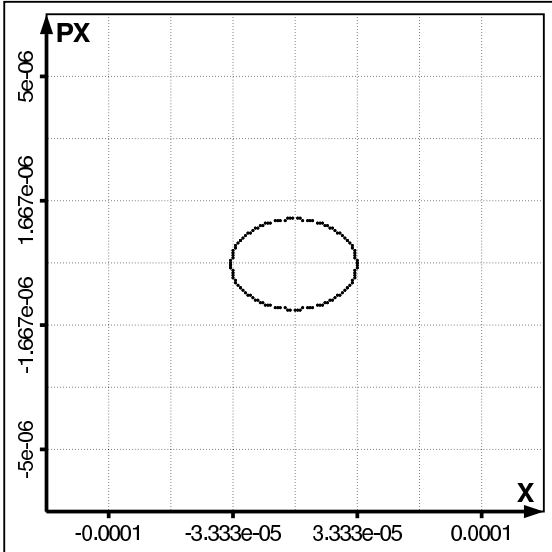


Figure 3.3.3: Tracking results for the total arc. The energy spread is $\pm 5\%$.

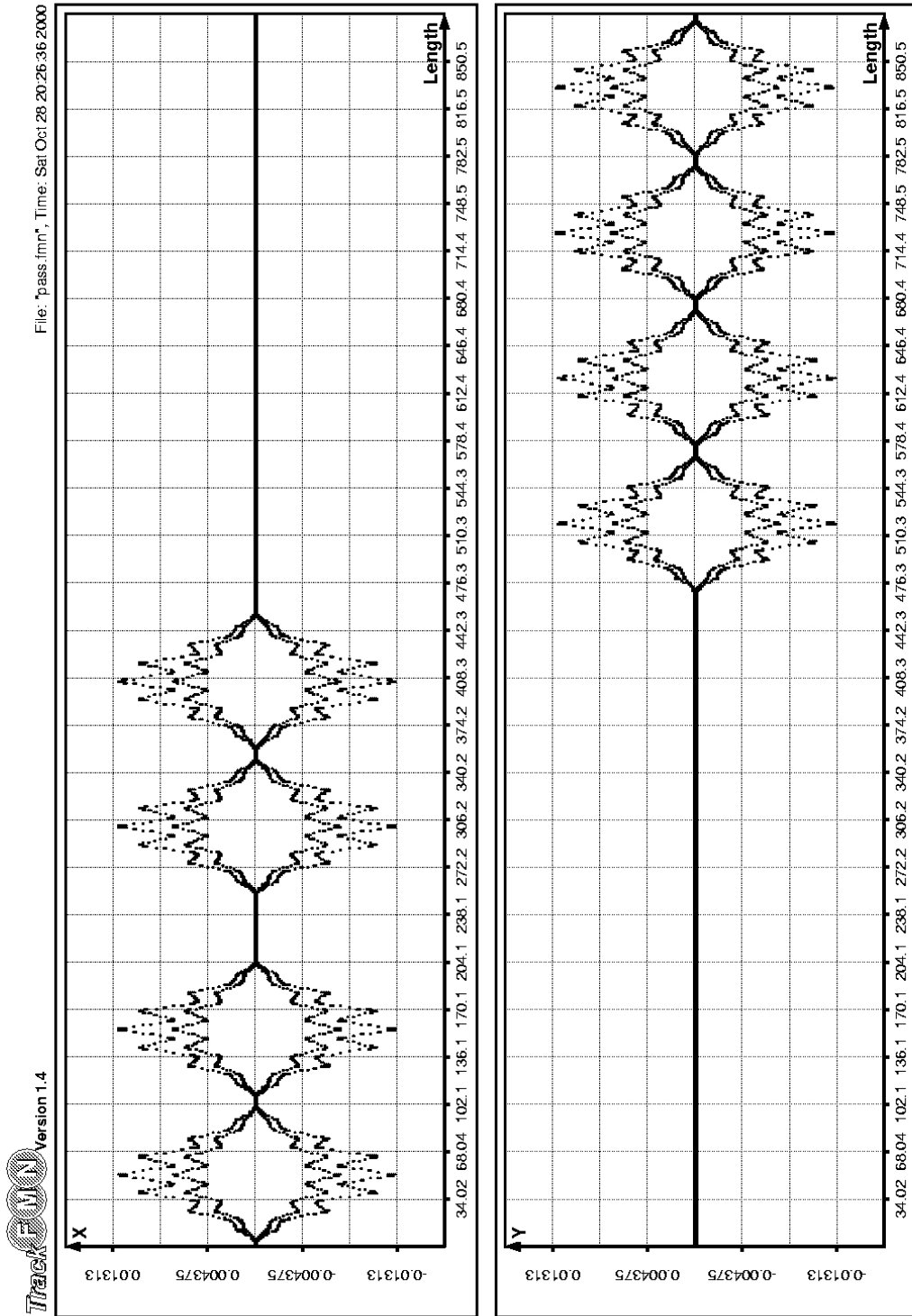


Figure 3.3.4: Trajectories of particles in four bunches along the total arc. The energy spread is $\pm 3\%$ and $\pm 5\%$.

acceptance of the total arc is $\pm 5\%$.

4 The electron beam distribution system

4.1 General requirements

This section discusses the design of the high energy transport lines for the separation of the bunch trains and distribution them to several FEL-users. The schematic layout of the FEL beam transport lines is shown in Fig. 4.1.1. The design requirements are:

- Provide a horizontal separation of the bunch trains with 1.4° bend for one branch of the transport line to deliver beam for two distinct FEL-undulators (SASE1 and SASE2 in Fig. 4.1.1). Pulsed magnets are used for the separation of the trains.
- Provide a horizontal deflection of $\approx 2.6^\circ$ between undulators.
- Provide an energy acceptance not smaller $\pm 3\%$.
- Introduce no significant transverse emittance dilution and additional energy spread.
- Provide a section for the integration of the fast feed back system.

The beam distribution system to distinct undulators contains two transport lines. The first beam line (BDL1) is used to take one of two following bunch trains, which came from the arc onto the surface, to deliver the beam to SASE1 and undulators U1 and U2. The second line (BDL2) takes the second bunch train and delivers it to SASE2 and undulator U3.

There are two parts of the transport lines which include bending magnets:

- the separation section (D1) which uses the pulsed dipoles;
- the section between undulators (D2) with DC dipoles.

The main concept of the beam line design is to find a solution for these two sections with dipole magnets, which satisfy the above mentioned requirements, and then to match them to the magnet optics of the undulators.

4.2 Optics for the separation of the bunch trains (D1)

The photon beams from the different undulators have to be separated by a distance of 17 m in the experimental hall. This requirement gives us the values of the horizontal angles for which the beam has to be deflected in the different parts of the beam delivery lines. For the separation section this deflection angle has to be equal to 1.4° .

For the dipole magnets of this separation we chose a bending radius of 1227.8 m. Using equation (13), the additional energy spread is $\sigma_E = 0.33 \text{ MeV}$ for an energy of 40 GeV.

A system that satisfies these conditions is composed of two pulsed dipole magnets of a length of 15 m separated by two quadrupole triplets to produce a linear achromat. The optics has mirror symmetry with respect to the center. To provide the required value of the energy acceptance the correction of the dispersion of second and third orders is made by two sextupoles and two octupoles using the TrackFMN Program [32]. The length of the D1 beam line is defined by the condition to have a horizontal beam inflection of $\approx 0.5 \text{ m}$ at the entrance of the second dipole magnet in order to have the suitable space for placing of the elements in both lines, BDL1 and BDL2.

The main parameters of the D1 beam line are summarized in Table 4.2.1. The dispersion and beta functions along the D1 section are shown in Fig. 4.2.1. The choice of two triplets between the dipoles was made to facilitate beam matching into and out of the system and to obtain such a behavior of the beta functions which allows to provide an acceptable value of the energy acceptance. Fig. 4.2.2 shows the results of the numerical tracking of

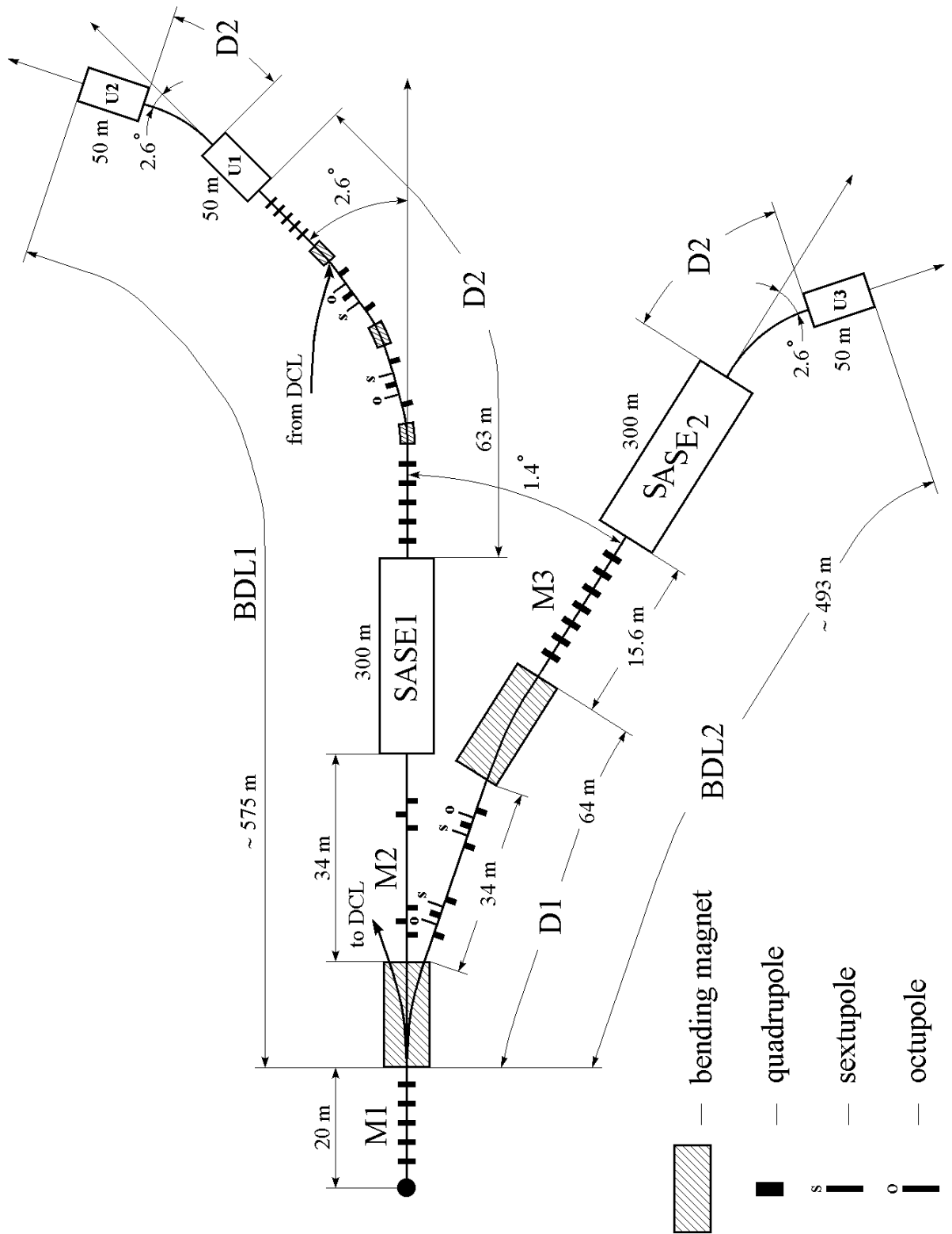


Figure 4.1.1: The layout of the beam delivery system.

Table 4.2.1: Parameters of the D1 beam line.

	Value	Unit
Length	64.0	m
Total number of dipoles	2	
Length of each dipole	15.0	m
Bend angle of each dipole	0.7	degree
Bending radius of each dipole	1227.77	m
Total horizontal inflection	0.78	m
Total number of quadrupoles	6	
Length of each quadrupole	0.8	m
Maximum quadrupole strength	0.35	$1/m^2$
Total number of sextupoles	2	
Length of each sextupole	0.4	m
Sextupole strength	3.68	$1/m^3$
Total number of octupoles	2	
Length of each octupole	0.4	m
Octupole strength	45.55	$1/m^4$
Maximum horizontal β -function	36.51	m
Maximum vertical β -function	23.83	m
Maximum horizontal dispersion	0.19	m
β_x at the entrance	20.05	m
β_x at the exit	20.05	m
α_x at the entrance	0.576	m
α_x at the exit	-0.576	m
β_y at the entrance	23.78	m
β_y at the exit	23.78	m
α_y at the entrance	0.444	m
α_y at the exit	-0.444	m
Additional energy spread at 40 GeV	0.33	MeV
Transverse emittance dilution at 40 GeV	0.13	%

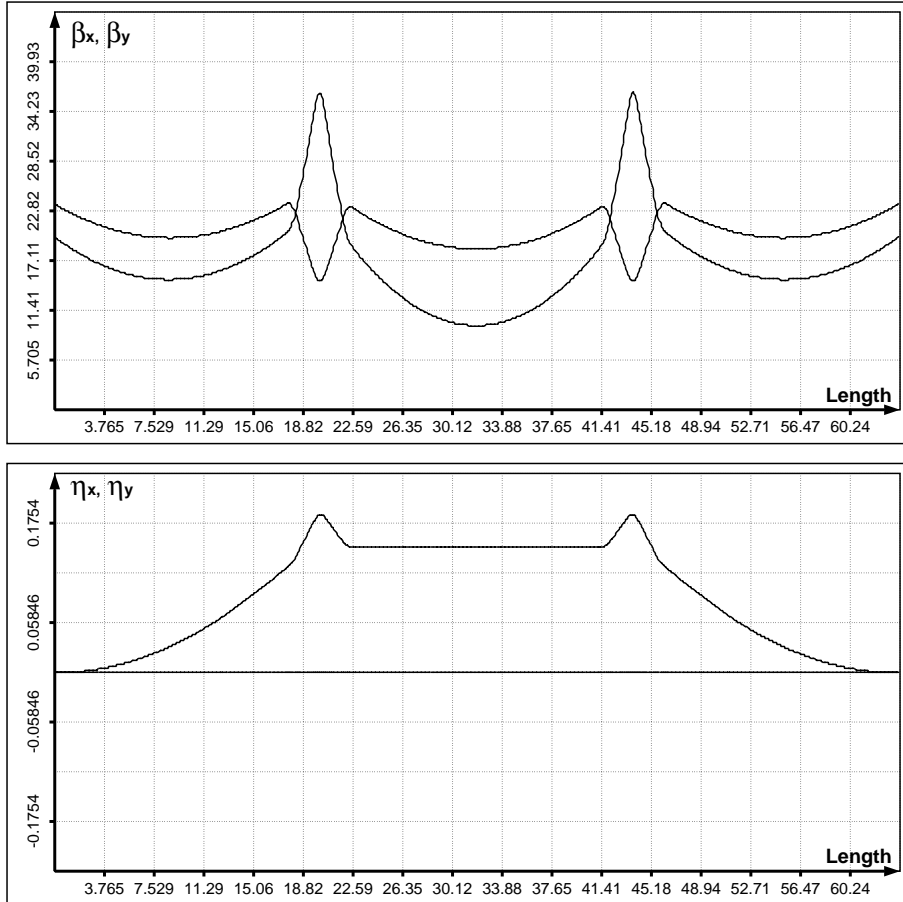


Figure 4.2.1: Dispersion and beta functions along the D1 transport line.

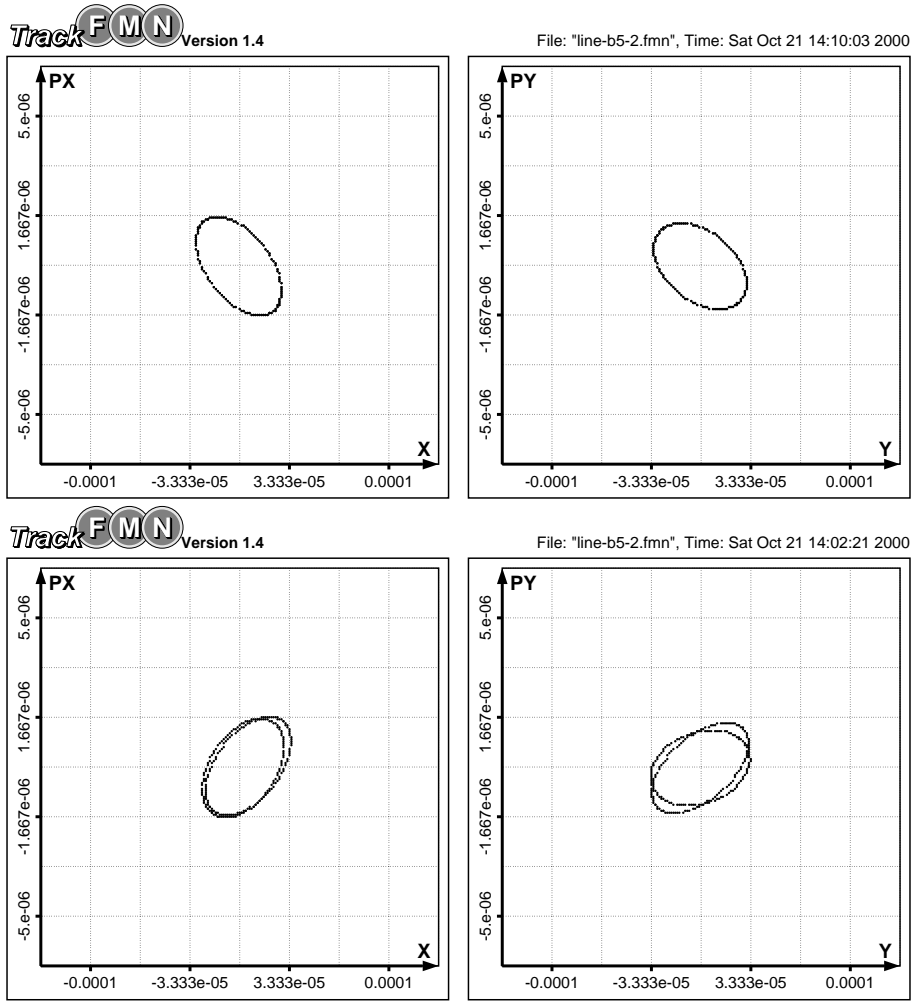


Figure 4.2.2: Tracking results for the D1 line. The energy spread is $\pm 5\%$.

particles, which are initially distributed uniformly along the perimeter of the phase space ellipses corresponding to the rms normalized emittance $\varepsilon_{x,y} = 1.6 \cdot 10^{-6} m \cdot rad$ at the energy of 20 GeV. The energy spread of particles on one ellipse is $+5\%$, on the second ellipse is -5% . The top figures show the phase space plots in the horizontal and vertical planes at the entrance of the first dipole. The bottom figures shows the ellipses at the exit of the second dipole. We see that the proposed magnet optics allows to let a bunch train with an energy offset of $\pm 5\%$ pass through with negligible distortion of the beam parameters.

4.3 Optics between undulators (D2)

The beam optics between distinct undulators has to deflect the beam for the different horizontal angles to bring the photon beams from distinct undulators to points in the experimental hall which are separated by the same distance of 17 m. In the present stage the average value of this angle is taken to be equal 2.6° to design the D2 transport line which satisfies the requirements pointed out in Section 4.1.

A triple-bend structure is proposed for the D2 beam line. Two quadrupole triplets are

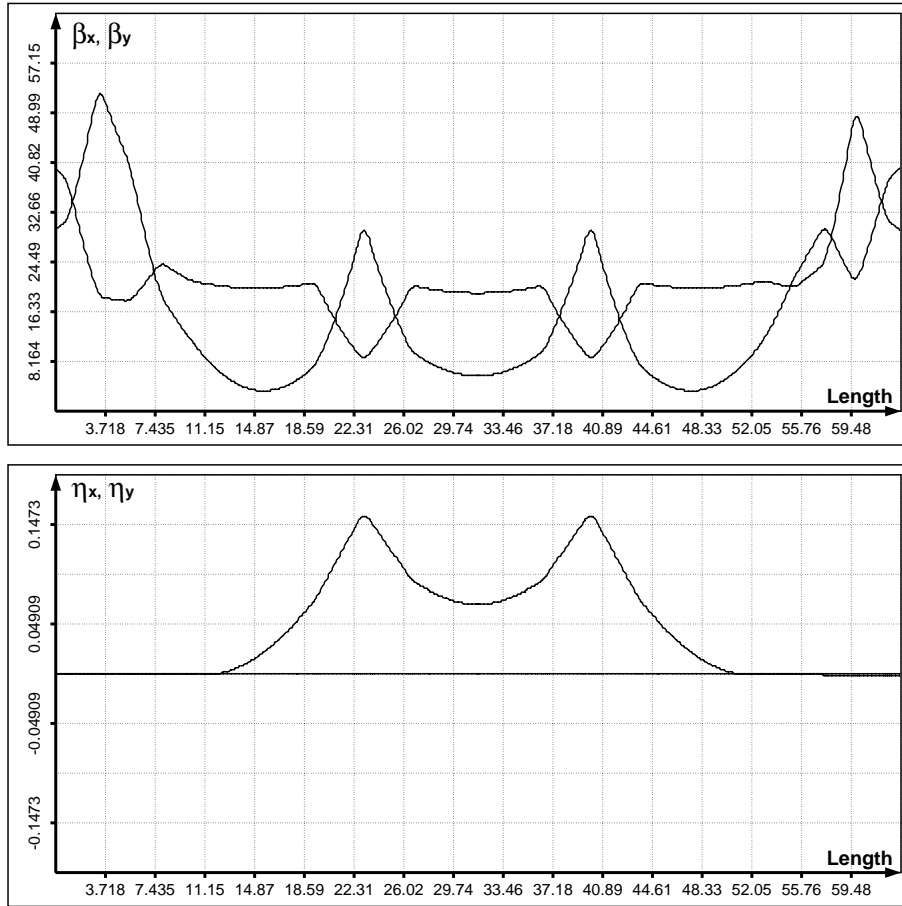


Figure 4.3.1: Dispersion and beta functions along the D2 line.

used between the dipole magnets, one sextupole and one octupole are placed between the quadrupole lenses in each triplet. The matching sections between the bend section and the exit of the undulator and the entrance of the following undulators have the same length of 11 m. Both of them are composed of five equally spaced quadrupoles ($\Delta l = 1.5$ m). For the matching we propose that the undulators have the separate quadrupole magnets (separated function undulators) and may be started with focusing or defocusing quadrupole. For all undulators the maximum beta function in both transverse planes is proposed to be equal to 40 m. The main parameters of the D2 beam line are summarized in Table 4.3.1. The optical functions at the entrance and exit are pointed out in the quadrupole center of the undulator. The dispersion and beta functions along D2 section are shown in Fig. 4.3.1. The maximum beta functions in the triple-bend section of the D2 beam line do not exceed 30 m in the horizontal and 21 m in vertical plane. In the matching sections the beta functions are larger.

Fig. 4.3.2 shows the results of the numerical tracking of particles with an energy spread of $\pm 3\%$ through the D2 line in the assumption that we start the tracking in the beginning of the D2 line. The top figures show the phase space portraits of particles in the beginning of the D2 beam line (the exit of SASE). The bottom figures show the phase portraits in the end of the D2 line (the entrance of U1 undulator). We see that the proposed

Table 4.3.1: Parameters of the D2 beam line.

	Value	Unit
Total length	63.0	m
Length of bend section	41.0	m
Length of each matching section	11.0	m
Number of dipoles	3	
Length of each dipole	7.0	m
Bend angle of each dipole	2.6/3	degree
Bending radius of each dipole	462.8	m
Total horizontal inflection	1.43	m
Total number of quadrupoles	16	
Length of each quadrupole	0.8	m
Maximum quadrupole strength	0.2	$1/m^2$
Total number of sextupoles	2	
Length of each sextupole	0.4	m
Sextupole strength	7.66	$1/m^3$
Total number of octupoles	2	
Length of each octupole	0.4	m
Octupole strength	137.5	$1/m^4$
Maximum horizontal β -function	52.25	m
Maximum vertical β -function	48.54	m
Maximum horizontal dispersion	0.16	m
Horizontal β -function at the entrance	29.96	m
at the exit	40.0	m
Horizontal α -function at the entrance	0.0	
at the exit	0.0	
Vertical β -function at the entrance	40.0	m
at the exit	29.96	m
Vertical α -function at the entrance	0.0	
at the exit	0.0	
Additional energy spread at 40 GeV	1.2	MeV
Transverse emittance dilution at 40 GeV	1.13	%

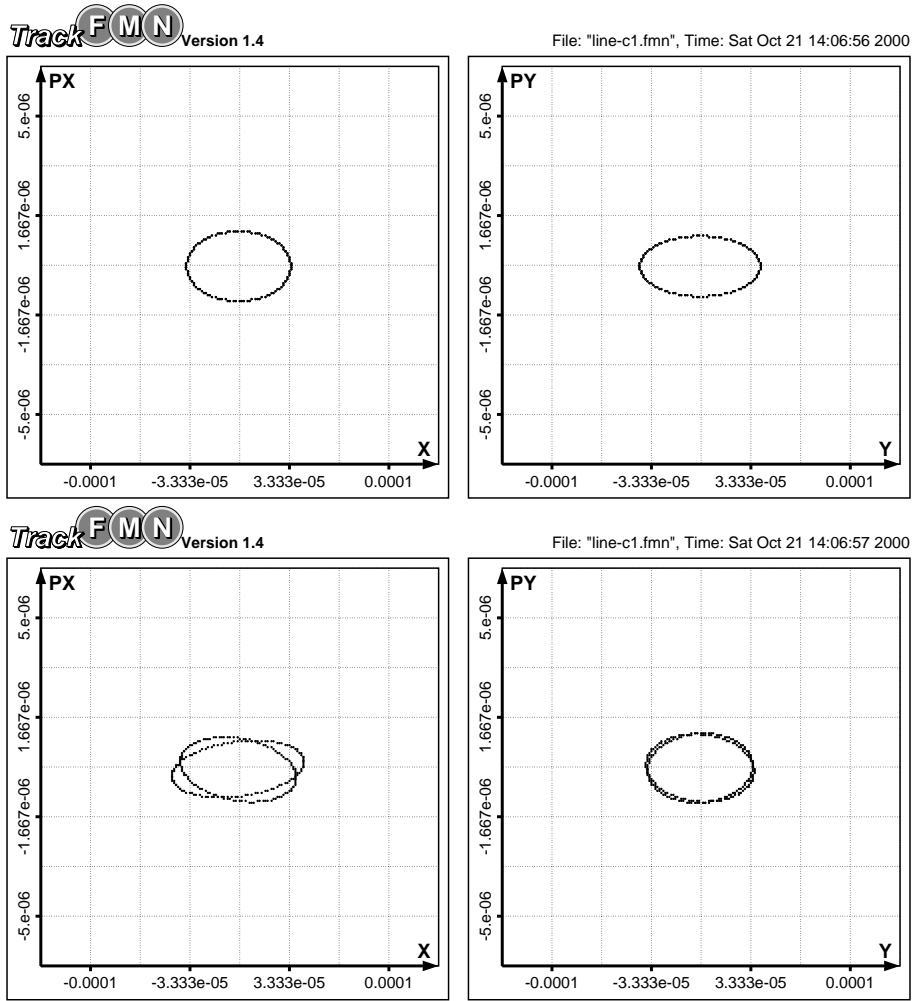


Figure 4.3.2: Tracking results for the D2 line. The energy spread is $\pm 3\%$.

magnet optics allows to let a bunch train with an energy offset of $\pm 3\%$ pass through with negligible distortion of the beam parameters.

4.4 Matching sections

There are three matching sections in the beam distribution system (see Fig. 4.1.1):

- between the vertical arc, which brings the beam onto the surface, and the entrance of the first pulsed magnet: the M1 matching section;
- between the entrance of the first pulsed magnet (which will be a drift for the BDL1 line) and the entrance of SASE1: the M2 matching section;
- between the exit of the second pulsed magnet and the entrance of SASE2: the M3 matching section.

Besides the simple requirement to match the beam parameters, there are additional conditions for the matching sections which have to be satisfied. The first condition is to integrate a fast feed back system in the M1 matching section. This question will be discussed in Section 4.5. The second is the protection collimation of undulators in the M2 and M3 matching sections. Some aspects of this problem will be pointed out in the end

Table 4.4.1: Parameters of the M1 matching section.

	Value	Unit
Total length	20.0	m
Number of drift spaces	4	
Drift space between quadrupoles	3.5	m
Total number of quadrupoles	5	
Length of each quadrupole	0.8	m
Maximum quadrupole strength	0.235	$1/m^2$
Maximum horizontal β -function	21.26	m
Maximum vertical β -function	60.4	m
Horizontal β -function		
at the entrance	7.06	m
at the exit	20.05	m
Horizontal α -function		
at the entrance	-0.550	
at the exit	0.576	
Vertical β -function		
at the entrance	27.06	m
at the exit	23.78	m
Vertical α -function		
at the entrance	1.908	
at the exit	0.445	

of this section. It is desirable that the optics of the matching sections provide an energy acceptance not smaller $\pm 5\%$. Then the energy acceptance of the BDL1 beam line before SASE1 and the BDL2 beam line before SASE2 will be $\pm 5\%$ too.

The M1 matching section has a length of 20 m and contains 5 quadrupoles, equally separated ($\Delta = 3.5 m$). The main parameters of the M1 matching section are summarized in Table 4.4.1.

The M3 matching section has a length of 15.6 m and contains 7 equally separated quadrupoles ($\Delta l = 1.5 m$). This optics allows to match the beam parameters to the entrance of SASE2 without fixing the quadrupole type at the beginning: it may be the focusing or defocusing quadrupole in case of a separate function undulator. The main parameters of the M3 matching section are summarized in Table 4.4.2.

The dispersion and beta functions along the M1 matching section and the part of the BDL2 line up to SASE2 are shown in Fig. 4.4.1. The full length of the transport line from the arc exit up to the entrance of SASE2 is 99.6 m. The tracking results for the BDL2 line are shown in Fig. 4.4.2. The energy spread of particles is $\pm 5\%$. The bottom figures represent the phase space plots at the entrance of SASE2.

The length of the M2 matching section has to be equal to 34 m to provide a horizontal separation of the beams of 0.5 m between the BDL1 and BDL2 lines at the entrance in the second dipole in the D1 line (see Fig. 4.1.1). The first dipole will be a drift for the BDL1 transport line. To provide the required energy acceptance the M2 section has been composed from 7 equally separated quadrupoles that allows easily to do the matching

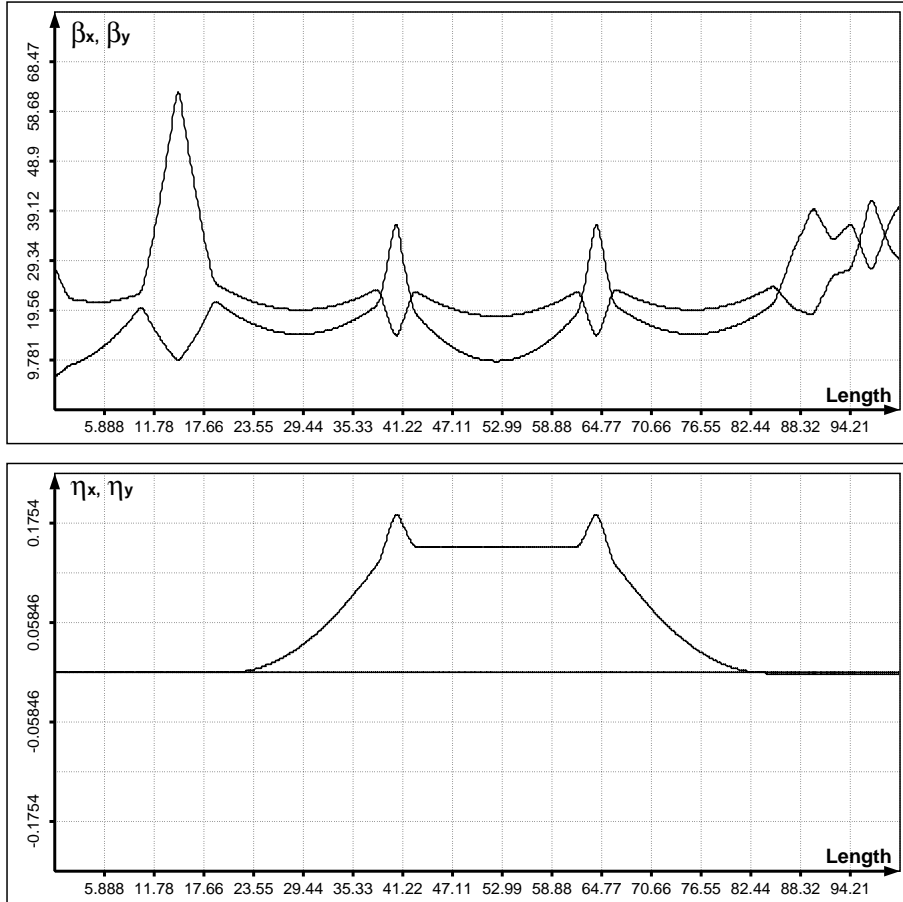


Figure 4.4.1: Dispersion and beta functions along the BDL2 beam line up to SASE2.

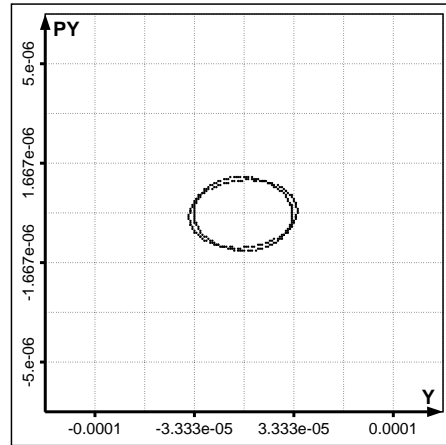
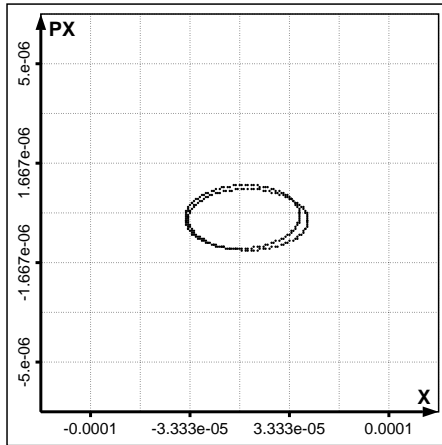
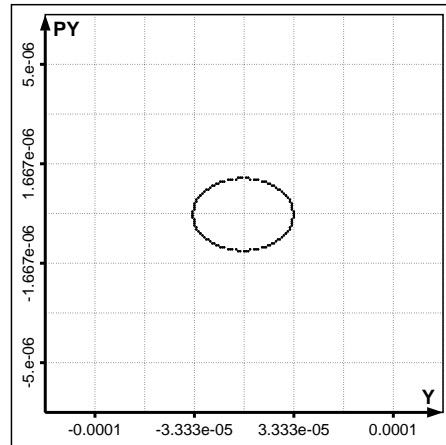
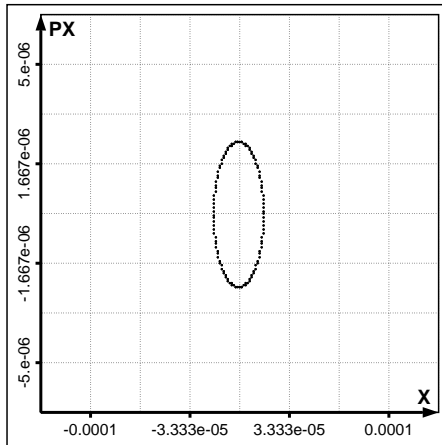


Figure 4.4.2: Tracking results for the BDL2 line up to SASE2.
The energy spread is $\pm 5\%$.

Table 4.4.2: Parameters of the M3 matching section.

	Value	Unit
Total length	15.6	m
Drift space between quadrupoles	1.5	m
Total number of quadrupoles	7	
Length of each quadrupole	0.8	m
Maximum quadrupole strength	0.18	$1/m^2$
Maximum horizontal β -function	40.0	m
Maximum vertical β -function	41.3	m
Horizontal β -function		
at the entrance	20.05	m
at the exit	40.0	m
Horizontal α -function		
at the entrance	-0.576	
at the exit	0.0	
Vertical β -function		
at the entrance	23.78	m
at the exit	29.96	m
Vertical α -function		
at the entrance	-0.445	
at the exit	0.0	

taking into account the drift space of the length of 15 m for the pulsed dipole. The main parameters of the M2 matching section are summarized in Table 4.4.3. The dispersion and beta functions along the BDL1 beam line up to SASE1 are shown in Fig. 4.4.3. Fig. 4.4.4 shows the tracking results for the BDL1 line. The energy spread of particles is $\pm 5\%$. The bottom figures show the phase space portraits at the entrance of SASE1.

The proposed solutions for the M1, M2 and M3 matching sections allow easily to do the matching of the beam parameters between the vertical arc exit and the entrances of SASE1 and SASE2. The energy acceptance of the proposed transport lines up to SASE1 and SASE2 is $\pm 5\%$.

The problem of the protection collimation before the undulators (SASE1 and SASE2) was not investigated in detail. An attempt has been done to design the optics of the M2 matching section with the additional requirements to organize some modulation of the beta functions in these sections without changing the section length. But the numerical investigations of the particle motion in the considered schemes show an essential reduction of the energy acceptance. For example, using two quadrupole triplets in the M2 section it is possible to obtain the modulation of the beta functions in both planes (horizontal and vertical) with a maximum value which does not exceed 45 m. The energy acceptance of such optics for the M2 section decreases up to approximately $\pm 3\%$. At the present stage of the study one may say that the problem of the protection collimation together with the task of the energy acceptance requires an additional detailed investigation.

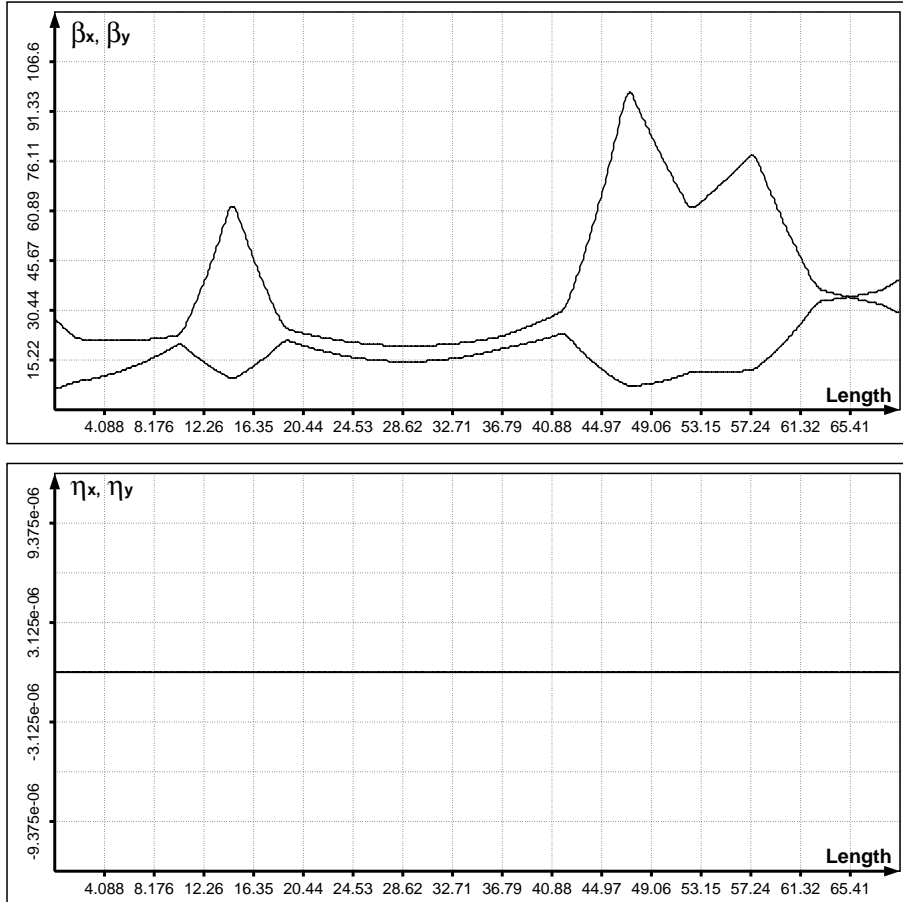


Figure 4.4.3: Dispersion and beta functions along the BDL1 line up to SASE1.

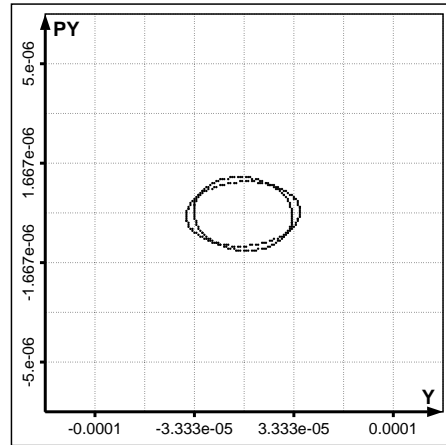
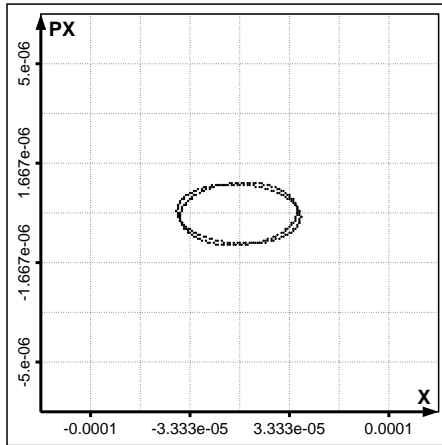
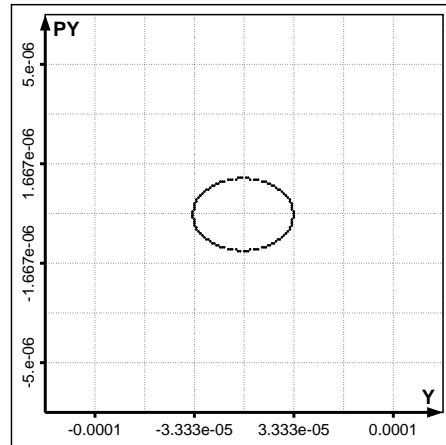
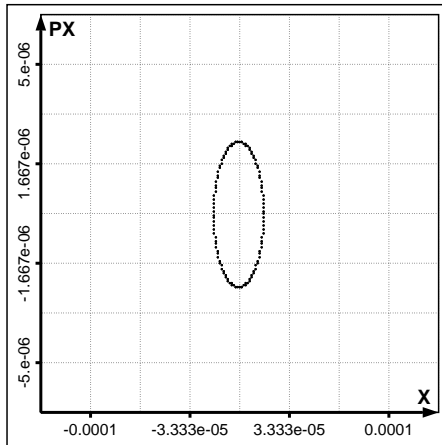


Figure 4.4.4: Tracking results for the BDL1 beam line up to SASE1.
The energy spread is $\pm 5\%$.

Table 4.4.3: Parameters of the M2 matching section.

	Value	Unit
Total length	34.0	m
Drift space between quadrupoles	4.4	m
Total number of quadrupoles	7	
Length of each quadrupole	0.8	m
Maximum quadrupole strength	0.15	$1/m^2$
Maximum horizontal β -function	40.0	m
Maximum vertical β -function	97.4	m
Horizontal β -function		
at the entrance	20.05	m
at the exit	40.0	m
Horizontal α -function		
at the entrance	-0.576	
at the exit	0.0	
Vertical β -function		
at the entrance	23.78	m
at the exit	29.96	m
Vertical α -function		
at the entrance	-0.445	
at the exit	0.0	

4.5 Integration of the fast feedback system

Disturbances like fast vibrations of dipoles and quadrupoles can not be detected and controlled by the usual correction scheme. In order to correct the position and the angle of every bunch in a train, a fast feedback is required. This fast feedback system is foreseen to be located in the M1 matching section. It will contain four fast kickers to steer the beam, two kickers for the horizontal plane and two kickers for the vertical plane. The length of each kicker is assumed to be equal to 1.1 m, the maximum magnetic field is up to 0.008 T.

The optics of the M1 matching section has been optimized taking into account the matching properties, the requirement to obtain the desirable value of the energy acceptance and the possibility to use it for the integration of kickers. As a quality criteria for the optimization of the efficiency of the feed back system we have chosen the area of the initial beam displacements which can be corrected to zero at the entrance of an undulator, assuming that the optics between kickers and undulator is linear and does not contain any misalignments. Fig. 4.5.1 shows the results of the optimization at an energy of 50 GeV. The inner ellipses in Fig. 4.5.1 are the phase space plots of a beam corresponding to $5\sigma_{x,y}$ at the entrance of the first of each pair of kickers (for the horizontal and vertical planes). The rectangles show the boundaries of phase spaces (also at the entrance of the first of each pair of kickers), in which the beam can be corrected. In the linear estimation this phase space region seems to be large that gives us the hope that taking into account the misalignments it will be still enough for the correction.

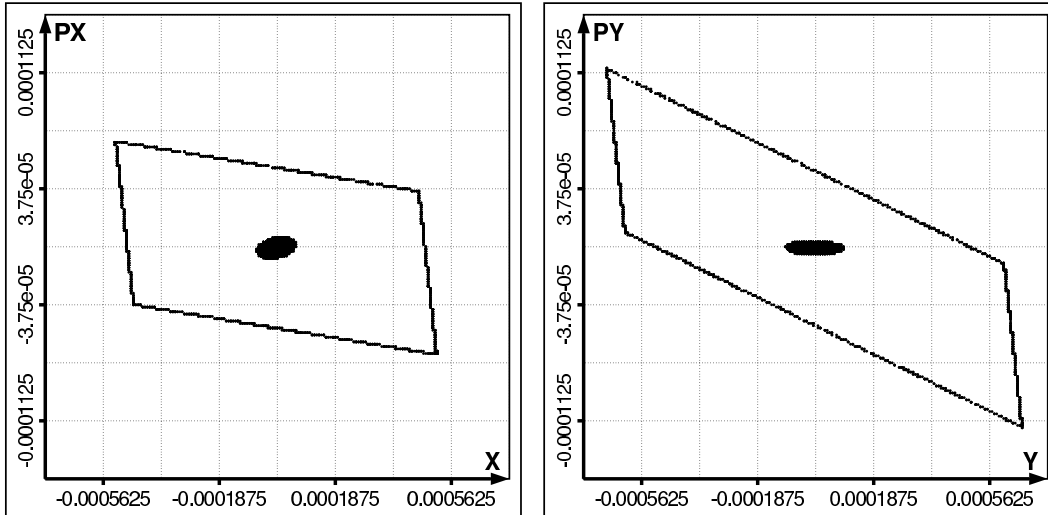


Figure 4.5.1:

Phase space plots at the entrance of the first kicker.

4.6 Summary

The proposed magnet lattice for the separation of the high energy beam and distribution to several FEL-users satisfies the general design requirements. The beam distribution system to distinct undulators contains two transport lines. The first line is used to take one of two following bunch trains to deliver the beam to SASE1 and undulators U1 and U2. The second line takes the second bunch train and delivers it to SASE2 and undulator U3. The horizontal separation of the bunch trains (with 1.4° bend for one branch of the transport line) is provided with the help of the pulsed dipole magnets. A triple-bend lattice is proposed for the horizontal deflection of $\approx 2.6^\circ$ between undulators. The proposed magnet optics for the beam lines up to SASE1 and SASE2 allows to let a bunch train with an energy offset of $\pm 5\%$ pass through with negligible distortion of the beam parameters. The energy acceptance of the beam lines up to U1, U2 and U3 undulators is $\pm 3\%$. The optics of the M1 matching section between the arc and the entrance of the first pulsed dipole has been optimized to have the possibility to use it for the integration of the feedback kickers. At the present stage of the study the problem of the protection collimation in the M2 and M3 matching section (before the undulators SASE1 and SASE2) together with the task of the energy acceptance requires an additional investigation.

5 The Diagnostic Commissioning line

The performance of the FEL radiation is very sensitive to the parameters of the electron beam. It is important to know the beam parameters just before (or as close as possible) to the undulators. The optics before and in the beam delivery system is specially designed to ensure the desired beam parameters in the restrictions of the space requirements and there is no sufficient space to organize complete beam measurements. For this purpose a special Diagnostic Commissioning Line (DCL) is designed in the beam delivery system. The main DCL purpose is to provide a possibility for precise measurements of all beam parameters. A DCL layout and general position scheme is shown in Fig. 5.1.

The DCL is placed at a distance of 1.135 m from the undulator SASE1. The bend magnet CM_1 ordinary operates in pulse mode distributing the electron beam between SASE1 and SASE2 undulators. To turn the beam into the DCL, it operates in a DC mode with improved field stability (see Chapters 8.1, 8.2). After the parameter measurements in the DCL the electron beam returns to the branch of the ordinary delivery system by using the bend magnet CM_5 .

5.1 The DCL structure

The initial beam and optic parameters at the entrance of the dipole CM_1 are assumed as follows: $\alpha_x = 0.5759, \beta_x = 20.045m, \alpha_y = 0.4449, \beta_y = 23.779m$, the rms transverse emittance of the beam is $\epsilon_x = \epsilon_y = 1.6 \cdot 10^{-6}m$, the average energy is $W_0 = 50GeV$, and the rms energy spread is $\frac{\Delta W}{W_0} = 2 \cdot 10^{-4}$. The DCL characteristics were calculated by using the TRANSPORT code [13].

The DCL consist of different parts designated to the different beam parameter measurements.

In the first DCL section, Fig. 5.1.1, the bend magnets CM_1 and CM_2 provide a parallel shift of the beam axis by a distance of $\approx 1.135m$. The doublet of quads CQ_{1-2} focuses the dispersion function of the DCL in the midpoint between the magnet CM_1 and CM_2 . The doublet of quads CQ_{4-5} focuses the dispersion function in center of dipole CM_2 .

The DCL dispersion function is shown in Fig. 5.1.2 . The quad lens CQ_3 is placed in position where the dispersion is zero and doesn't disturb it.

The beam average energy W_0 is measured by means of two pairs of the Beam Position Monitors (BPMs), installed before and behind dipole CM_2 , (Fig. 5.1). The mean energy deviation $\Delta W = W - W_0$ is related to the angular deviation of the beam center from a reference trajectory and the dipole field inductance B . In a 'thin' magnet approximation $\Phi_0 \ll 1.0, \cos \Phi \approx 1$, the mean energy deviation ΔW depends on the entrance angle θ_{in} and the exit angle θ_{out} of the beam center as:

$$\frac{\Delta W}{W_0} = \frac{\theta_{out} - \theta_{in}}{\Phi_0}, \quad (16)$$

where $\Phi_0 = 1.22 \cdot 10^{-2} rad(0.7^\circ)$ - is the bend angle of the reference trajectory in the dipole magnet CM_2 . The precision of the average energy measuring due to the precision of the dipole field measuring and the field stability is $\frac{\delta W_B}{W_0} = \frac{\delta B}{B_0} + \frac{\Delta B}{B_0}$. The dipole magnet field can be measured by an Nuclear Magnetic Resonance probe with an accuracy of $\approx 10^{-5}$ and the stability of dipole field may be $\frac{\Delta B}{B_0} \approx 10^{-5}$ (see Chapter 8.2). It provides the lower limit for the energy measurement resolution $\frac{\delta W_B}{W_0} \sim 1.4 \cdot 10^{-5}$.

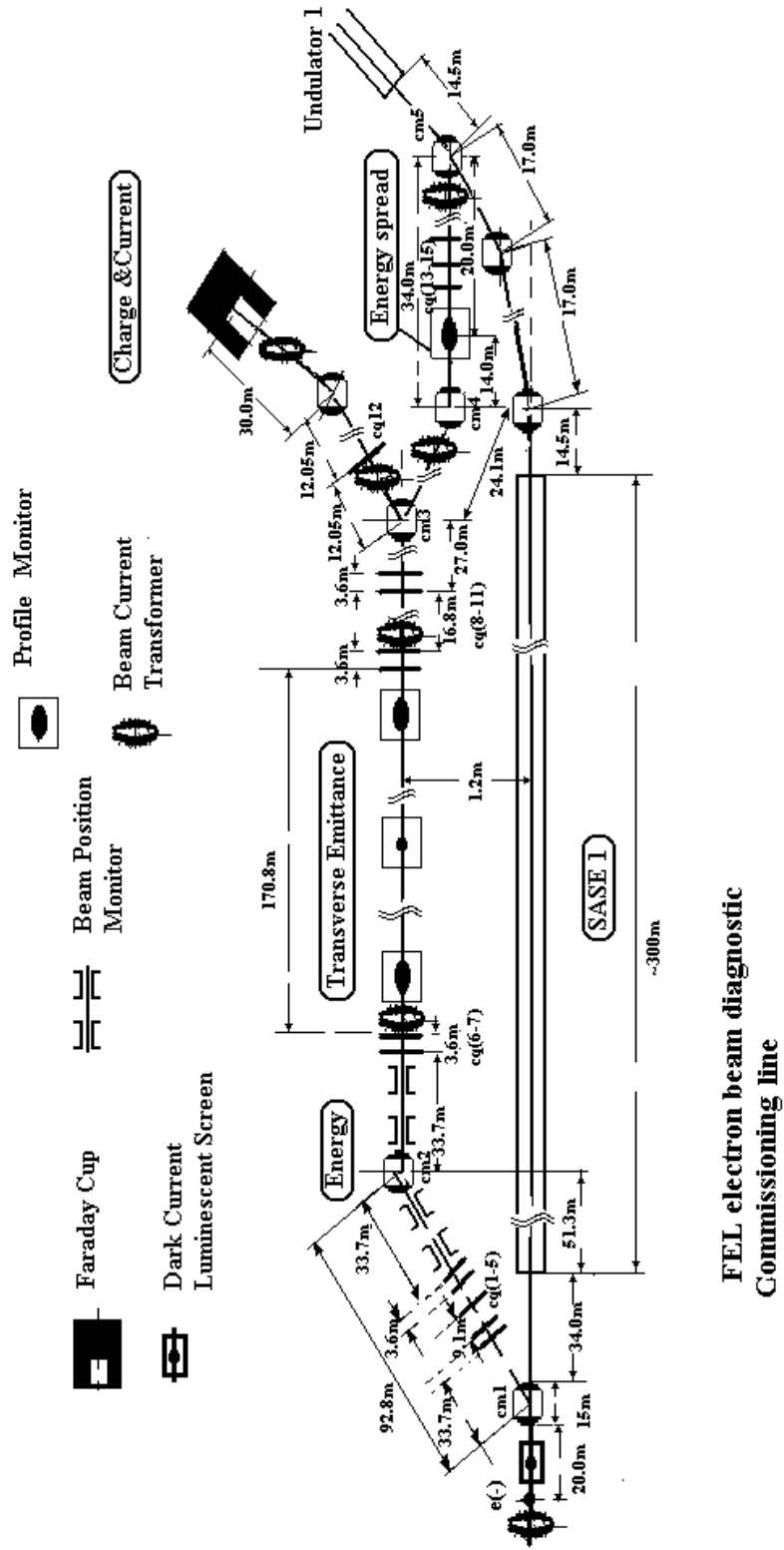


Figure 5.1: The DCL layout and general scheme.

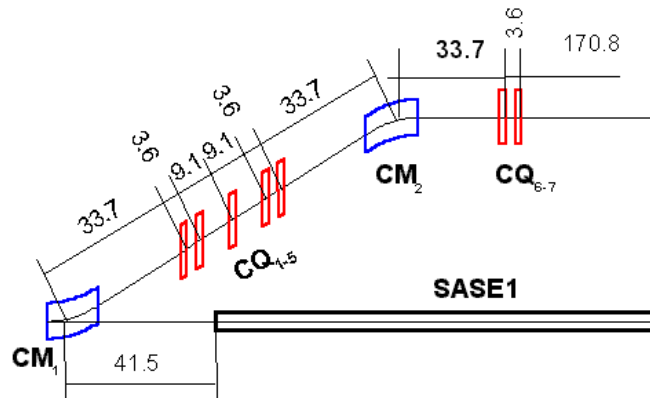


Figure 5.1.1: The DCL first section.

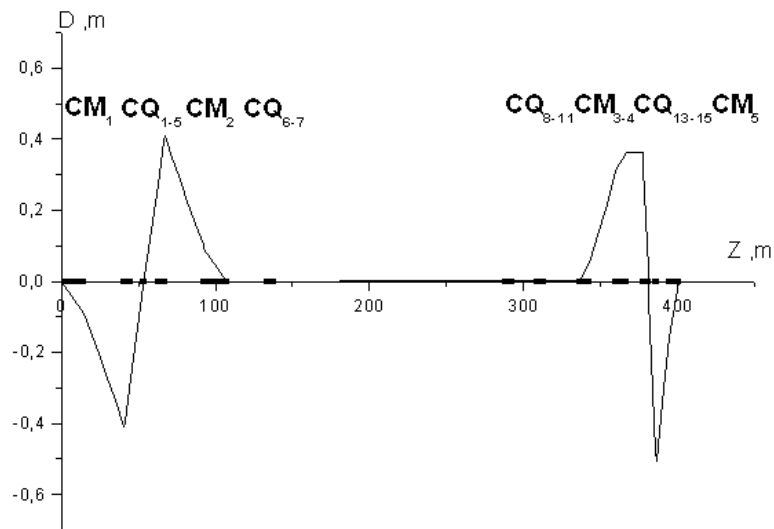


Figure 5.1.2: The dispersion function along the DCL.

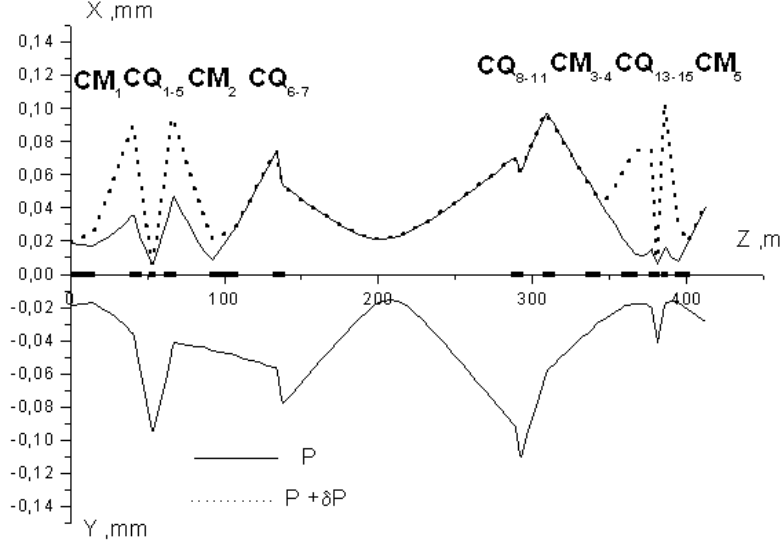


Figure 5.1.3: The rms beam envelope in the DCL.

The beam center angle is measured by means of two BPMs with an accuracy $\delta\eta = \frac{\sqrt{2}\delta x}{L_b}$, where δx is the BPM resolution, L_b is distance between BPMs. The accuracy of the average energy definition due to the finite BPMs resolution is $\frac{\delta W}{W_0} = \frac{2\delta x}{L_b\Phi_0}$. In our case $L_b = 25m$. To reach the average energy measuring accuracy better than $\frac{\delta W}{W_0} \sim 2.0 \cdot 10^{-5}$ one needs in the BMP resolution better than $2\mu m$.

The next DCL part, the drift space between doublets CQ_{6-7} and CQ_{8-9} is devoted to the transverse emittance measurement. In general, in the DCL it is possible to measure components of the total beam parameters matrix, taking into account the coupling of the particle motion in the x and y plane. Such methods are known, (see, for example, [15]) and need at least 10 transverse profile measurements and a special probe placement. The DCL length is large enough to realize such approach, but the optics design should be subject of development.

Because a beam with equal emittances in both planes is foreseen for TESLA, the coupling parameters are not relevant and the $2D$ projected beam emittances ϵ_x and ϵ_y are measured in the drift space with a length $2L_d = 150m$ between the doublets CQ_{6-7} and CQ_{8-9} . The lenses CQ_3 , CQ_6 and CQ_7 match the beam to the double-waist in the center of this drift with rms radii $\sigma_x \approx \sigma_y \approx 20\mu m$. At a distance of $L_d = 75m$ from the waist the beam has rms radii $\sigma_x \approx \sigma_y \approx 80\mu m$. The rms beam envelopes in the DCL are shown in Fig. 5.1.3.

Three transverse beam profiles are measured in three locations with Wire Scanners (WS) to determinate three independent elements of the 2×2 symmetrical beam matrix Σ and rms emittance ϵ of the beam :

$$\Sigma = \begin{pmatrix} \langle x^2 \rangle & \langle xx' \rangle \\ \langle xx' \rangle & \langle x'^2 \rangle \end{pmatrix}, \epsilon_2 = \langle x^2 \rangle \langle x'^2 \rangle - \langle xx' \rangle^2$$

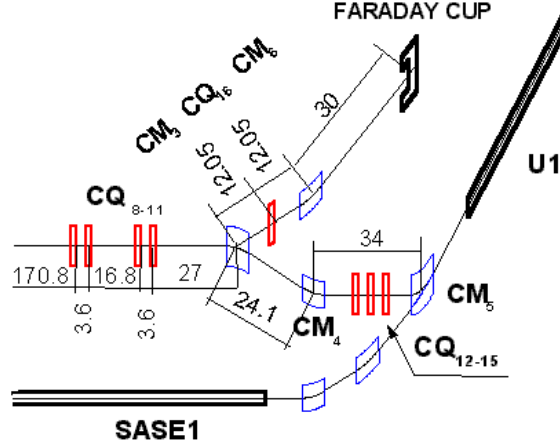


Figure 5.1.4: The last DCL section.

If one of the WSs is placed just in the waist of the beam and the second WS at distance L_d from the waist, where $r(L) \gg r(0)$, the rms emittance ϵ and the precision of the measurement $\frac{\delta\epsilon}{\epsilon}$ are:

$$\epsilon^2 = \frac{\sigma(L_d) - \sigma(0)}{L_d^2} \sigma(0), \quad \frac{\delta\epsilon}{\epsilon} = \frac{1}{2} \left(\frac{\delta\sigma(L_d)}{\sigma(L_d)} + \frac{\delta\sigma(0)}{\sigma(0)} \right), \quad (17)$$

where $\sigma(L_d), \sigma(0)$ are the standard deviations of the transverse beam profile distribution. To measure the transverse emittance with a precision of $\approx 5\%$ one needs to measure the standard deviation of the beam spatial distribution with the same accuracy in a wide range of beam radii ($20 \div 80$) μm .

The last DCL section, Fig. 5.1.4, delivers the beam to the undulator $U1$ and further to the in beam-dump. The dipole magnets CM_3 and CM_4 provide the parallel beam axis shift at a distance of $\approx 0.36m$, than the beam reaches the dipole CM_5 entrance. During the DCL operation the dipole CM_5 bends the beam at an angle of 2.6° , during standard beam delivery operation the bending angle of this dipole is 0.867° .

The triplet of lenses $CQ_{12} - CQ_{15}$ ensures an achromatic beam delivering from the dipole CM_3 entrance to the exit of the dipole CM_5 . The dispersion at this DCL section is shown in Fig. 5.1.2.

The energy spectrometer is organized behind the dipole CM_4 . The lenses $CQ_8 - CQ_{11}$ match the beam to the double-waist at a distance of $\approx 7m$ behind the dipole CM_4 . The magnets CM_3 and CM_4 produce the dispersion equal to $0.36m$ in this point. The beam radius in the bending plane is equal to $\sigma_x = 7\mu m$ and in the perpendicular plane is equal to $\sigma_y = 30\mu m$. The resolution R_e of the spectrometer is $R_e = \frac{2\sigma_x}{D} = 0.4 \cdot 10^{-4}$.

For absolute bunch charge measurements and Beam Current Transformer (BCT) probe calibrations a Faraday Cup is used. The DCL branch - magnets CM_3, CM_6 and quad

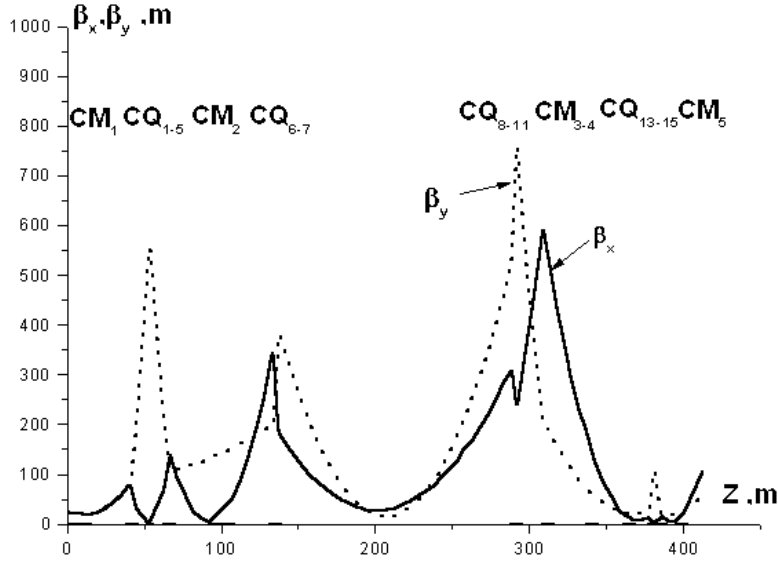


Figure 5.1.5: The optic functions along the DCL.

Table 5.1.1: The DCL dipole magnets specification.

Dipole	Bending radius, m	angle, deg angle, deg	Pole field, T	Length m
CM_1	1226	0.7	0.136	15.0
CM_2	1226	0.7	0.136	15.0
CM_3	463	0.867	0.36	7.0
CM_4, CM_6	463	0.867	0.36	7.0
CM_5	154	2.6	1.08	7.0

CQ_{16} - achromatically delivers the beam to the Faraday Cup. Each dipole, CM_3 and CM_4 , bends the beam at an angle of 0.867° in the same direction. At the Faraday Cup entrance the beam is de-focused with $\sigma_x = \sigma_y = 300\mu m$.

The optics beta functions along the DCL are shown in Fig. 5.1.5. The specifications for the dipole magnets and the quads of the DCL are presented in Table 5.1.1 and Table 5.1.2, respectively. The effective length for all quadrupoles is equal to $0.8m$, the aperture diameter is equal to $35mm$.

5.2 Diagnostic tools and methods

The TESLA FEL electron beam is unique in its parameters - the transverse and longitudinal bunch dimensions and bunch charge. The time separation between bunches of $\approx 93ns$ is also not so large. Together with a slow operating mode - during the bunch train, the diagnostic equipment should allow to perform fast - "bunch to bunch" measurements.

Table 5.1.2: The DCL quads specification.

Quad	Gradient, T/m	Quad	Gradient, T/m	Quad	Gradient, T/m
CQ_1	24.040	CQ_6	21.486	CQ_{11}	0.001
CQ_2	-2.137	CQ_7	-19.543	CQ_{12}	61.566
CQ_3	-19.143	CQ_8	10.263	CQ_{13}	-60.000
CQ_4	-2.137	CQ_9	-16.611	CQ_{14}	52.293
CM_5	24.040	CQ_{10}	8.069	CQ_{15}	35.383

5.2.1 The beam intensity measurements

Beam Current Transformer (BCT). BCTs are used for ordinary bunch charge and average current measurements in the bunch train. BCTs have both fast and slow operating modes. The fast mode is for bunch by bunch measurements. In this case the BCT signal is damped enough in the interval between bunches. A slow - resonant mode is for the Faraday Cup (FC) efficiency measurements on different beam energies and is used in the shortened train (several hundred of bunches) mode. The BCT behind CM_6 (Fig. 5.1) is used for this aim. When the FC efficiency is measured according to the standard zero-method, calibrations of the DCLs BCTs should be done. The precision of the bunch charge measurements is better than 0.1% [16] for the BCT resonant mode.

Faraday Cup. FC is necessary for the calibration of other beam intensity monitors by means of an absolute bunch charge measurements. The Faraday Cup is installed at the end of the DCL and measures a charge of a single or a few bunches in the shortened bunch train mode.

The FC was designed and tested for high energy electron beam with an energy of 15 GeV [17]. At this energy the effects of secondary emission and back-scattering of primaries was found less than 0.1%. The FC's absolute efficiency is $(100.0 \pm 0.2)\%$ at energies from a few hundred MeV up to 15 GeV.

With the rms spot-size $\sigma_x \cdot \sigma_y \approx 300\mu m \cdot 300\mu m$ the FC with titanium core can withstand ≈ 800 bunches and a survival problem doesn't exist for the shortened bunch train. But for the FEL beams and energies up to 50 GeV the technical FC development is necessary.

Dark current measurements. The dark current can reduce strongly the signal to noise ratio of beam monitors at the TESLA linac exit. With the transverse phase space collimation and due large difference in energy with the main beam, the dark current should be reduced strongly at the exit of the transport system. Very sensitive probes should be used to estimate the dark current value. It is possible to use the movable luminescent screen. For a low intensity signal observations $AL_2O_3(Cr)$ screens were used with the intensified CCD camera. The $AL_2O_3(Cr)$ screens have a sensitivity $\approx 2.0 \cdot 10^6 \frac{part.}{mm^2}$ without an intensifier or more with an intensifier $\approx 2.0 \cdot 10^2 \frac{part.}{mm^2}$ [18].

The Cryogenic Current Comparator (CCC) has not such a high sensitivity, and it is a more complicated device. But it also can be used for dark current measurements at the exit of the TESLA Linac as non-destructive monitor. The CCC has a noise level of $\approx \pm 1.5 \cdot 10^{-9} A$ for 100Hz bandwidth and pulse duration $\approx 2.5s$. For 1 ms pulse the CCC bandwidth should be of 10.0kHz or more and the CCC resolution will be worse correspondingly for this conditions [19].

Due to the higher sensitivity and lower costs the movable luminescent screen is recommended for the dark current intensity measurements in the DCL. The calibration of this

probe can be performed with the help of the Faraday Cup, similar to the BCTs calibration.

5.2.2 Beam Position Monitors (BPMs)

The transverse beam position measurements with the high precision are of major importance both for the TESLA FEL beams and for the TESLA collider too. The main point are the BPM resolution and response time. To ensure the required beam parameters, the BPMs with a resolution of order of a few μm in the fast (bunch to bunch) mode are required. The strip line BPM can be intended for these measurements. The maximal estimated strip line BPM resolution [20] is μm for a chamber diameter of $50mm$. At present the best resolution of a strip line wide bandwidth BPM achieved for bunch by bunch measurements is $\approx 20\mu m$ in the interaction region of the SLC for $5 \cdot 10^9$ particles per bunch. The development of a fast BPM with a few μm resolution is a general problem for the TESLA collider.

For the slow mode of measurements the resonant BMPs [21] may be used, providing better than $1\mu m$ resolution. Such BMPs are foreseen for the average energy measurements in the DCL. It is possible to use other methods for high resolution beam position measurements. Wire Scanners were used at CEBAF for this purpose in the average beam energy measurements by means of the beam angle measurement behind dipole magnet [22].

5.2.3 Transverse beam profile measurements

Beam profile measurements. Transverse beam profile monitors are used in the DCL for the beam emittance and the energy spread measurements (see Section 5.1). The beam profile instruments are Wire Scanners (WS).

There are two possibilities to detect the signal - secondary emission electrons and bremsstrahlung. It was observed in experiments, that the secondary emission signal from high density positron and electron primary beams differs by a factor 5 [25]. The scaling to the FEL beam parameters, according to [25], shows also a strong space charge influence. The direct numerical simulations (with some simplified assumptions) also confirm a strong profile difference between primary and secondary electrons [26]. The secondary electron emission signal can hence not be recommended at the FEL beam parameters and the bremsstrahlung radiation measurements should be used. Bremsstrahlung radiation is emitted in direction of the incident beam and is free of the space charge problem. The radiation intensity is sufficient to be detected.

The wire temperature is also very important. The key problem is an energy deposition during the high energy electron beam interaction with the wire material. The direct calculations of particle energy losses were done by using the EGS4 code, providing an upper estimation. Additional estimations have been performed by using micro-dosimetry methods. Both approaches provide similar results. The wire temperature simulations, taking into account results obtained for an energy deposition, gives a wire temperature value of $\approx 1150^\circ C$, coinciding with the results, obtained basing on experimental data [24] and scaling results from [23]. So, for a flying wire of $4\mu m$ in diameter, a velocity of $5\frac{m}{s}$, a bunch train average current of $11mA$ and a beam $\sigma_x, \sigma_y \approx 25\mu m$ the maximal wire temperature is estimated $\approx 1150C^\circ$. In these estimations [23], it was taken into account that only 30% of the particle energy losses in a wire volume convert to the wire heating [24]. The alternative calculations for 50% energy conversion show for the same conditions

that maximal the wire temperature is $\approx 1450C^\circ$ [26], also within the tolerable limits. During the duration of the beam-wire interaction of $\approx 30\mu s$, the radiative temperature decrease is small and practically cannot decrease the wire temperature. The thermal electron emission and the material evaporation at these temperatures have also small enough values. So, the wire temperature is not the problem at the FEL beam parameters.

However, the WS cannot measure the bunch profile of every single bunch. It is possible in principle by means of a Multi-wire Grid (MG) detector or Optical Transition Radiation (OTR) detector on a metal foil. The MG detector has the same problems with the space charge effect and temperature as WS, and the OTR foil has the problem with the temperature. So MG and OTR detectors should be also implemented with a mechanism for flying through the beam. For the FEL beam parameters the space charge influence on the secondary emission is strong and in measurements with the MG or OTR foil the Bremsstrahlung or back OTR radiation should be used. Moreover, special detectors are needed to measure the radiation behind the MG or OTR foil. This technique needs more development.

Transverse beam emittance recovering. The well known method of the three transverse profile measurements is realized in the DCL. It is based on measurements of the beam profile at three locations for a few bunches in the train by WS's with step wise transverse movements. The rms spot-size σ_m recovered with this technique is determined by the rms beam size σ_x and the wire diameter d [25]. $\sigma_m^2 = \sigma_x^2 + \frac{d^2}{4n}$ where $n = 3 - 4$. For $\sigma_x = 20\mu m, d = 4\mu m, n = 4, \sigma_m = 20.025\mu m$ and the error for the σ_x evaluation is 0.125%. For a larger beam size the error is smaller. In the DCL the beam spot-size at the emittance station PM's are of $80\mu m$ on the first and the third PMs, and $20\mu m$ on the central PM. The drift length is $150m$. If the distances between the PM's are known with an accuracy of 0.1% and the beam jitter is of $\approx 1\mu m$, the precision of the emittance recovering is $\approx 1\%$ as the sum of all errors. This technique needs several shortened bunch trains. It is possible also to use the flying WS for profile measurements during one bunch train, but with an improved velocity control.

5.2.4 Energy spread and longitudinal bunch shape estimation

. The energy spectrum measurements are developed in the energy spectrometer at the DCL end which may also be used for calibration of the radiation bunch length probe which can measure bunch length without linac phase adjustment. The energy spectrometer consists from the dipole magnet CM_4 and a PM installed behind CM_4 at the focal plane (Fig. 5.1). The dispersion in the place of the profile monitor is $0.36m$. With the energy spread $\frac{\delta W}{W} \sim 2.0 \cdot 10^{-4}$ the spot-size is about $\sim 72\mu m$, which is sufficient for reliable measurements.

The longitudinal bunch size can be estimated by registration of the beam radiation at wavelength equal and longer than the bunch length. Cherenkov, synchrotron, OTR or undulator radiation emitted by the bunch are possible radiation sources. But these methods provide estimations of the bunch length that should be compared with more precise technique based, for example, on streak camera measurements. At present the best streak camera resolution for the bunch radiation pulses is about $\approx 0.5ps$. For a streak camera resolution improvement the method with secondary electrons longitudinal rf energy modulation was proposed in [27]. At present this promising method is known at the level of the proposal and needs more development both in simulations and in experimental

verification.

Hence, another methods, with higher level of development, are required. The first one is Zero-Phasing (ZP) [28] method. The details of this technique are described in [28]. The bunch duration as short as $84fs$ rms have been measured on the CEBAF injector by means of this method. A similar technique was used for bunch shape measurements at the exit of the SLAC Linac.

Estimations, following to [28], shows the energy spread increasing to $\approx 7.0 \cdot 10^{-4}$ with a corresponding spot-size increasing to $\approx 250\mu m$ if one half of the linac is in ZP mode. It allows reliable estimations for the bunch length.

5.3 Summary

The DCL beam line has all possibilities for the measurements of all relevant beam parameters and calibrations of another beam diagnostic monitors. The beam charge and current can be determined with the Faraday Cup and the Beam Current Transformers. The FC efficiency will be defined by using the BCT in resonant mode according to the well known 0-method. After this procedure the calibration of all another BCTs by means of the FC can be performed. These measurements are possible in the shortened bunch train mode due to the possibility of the FC destruction. The calibration of the radiation bunch length monitors and the bunch length estimation can be performed by applying the zero-phasing technique with the energy spectrometer. The transverse profile and emittance measurements can be performed with high accuracy by means of wire scanners.

6 The beam transport to the dumps

After the undulators U2 and U3 (see Fig. 4.1.1) the electron beam should be transported to the dumps and absorbed. In this path there are no strong requirements for the beam emittance preservation as before the SASE undulators (see Chapters 3,4), but severe limitations still exist.

To prevent the dump destruction by a single bunch, the bunch spot size must be large $\sigma_{x,y} \geq 1.8mm$. This requirement should be fulfilled all times both for a narrow $\approx 2.0 \cdot 10^{-4}$ and for a wide $\pm(3 \div 5)\%$ energy deviation.

The beam transport line should accept the electron beam in the energy range (20 \div 50)GeV.

The dump position and orientation before the experimental hall is defined by the radiation safety requirement that the secondary muonen cone should pass below the hall.

The beam dump is an expensive device and the number of dumps has to be minimized while fulfilling all the above mentioned requirements.

The particularity of the beam dump transport line is in the wide "dynamical" range of the beam parameters. To provide the required beam spot size one can use different approaches. But if the bunch spot size of 1.8mm in one direction will be done by dispersion for an energy spread of $2.0 \cdot 10^{-4}$, than for the energy deviation of 5% the beam spot size will be 450mm, an intolerable value. If one will use the transverse emittance growth (see Section 3.1) at an energy of 50 GeV to provide the required beam spot size, at an energy of 20 GeV this growth will be of ≈ 250 times smaller, according to (14), resulting in a 15 times spot size reduction. The optics scheme for the dump line should ensure the required bunch spot size parameters for all beam parameters and control it during a wide range of parameters. It means that the emittance growth should be restricted and the dispersion in the lines should be limited also.

6.1 The basic layout of the optics

Possible schemes of the Beam Dump Transport Lines (BDTLs) are shown in Fig. 6.1 for different options. For the Beam Dump Transport Lines (BDTLs) a block structure is proposed. The BDTL after each undulator consists of several unified blocks:

- a matching section to match the undulator optics with the optics of a downstream bending arc;
- a bending sections consisting from the vertical and horizontal bending arcs to direct the beam into a beam dump;
- a defocusing section with integrated sweeping system to increase both the bunch spot size and the effective beam spot size of a bunch train too.

The BDTL characteristics were calculated by using the TRANSPORT code [13].

6.1.1 Matching Section

The Matching Section (MS), (Fig. 6.2b) behind the undulators (Fig. 6.2a), adjusts the beam for transport in the bending section. The parameters of the beam at entrance of the D2 line in the distribution system (see Chapter 4, the Table 4.3.1) are used as initial beam parameters at the entrance of the matching section. Beta functions are reduced in the matching section from $\beta_x \sim \beta_y \approx 40m$ in the undulators to $\beta_x = \beta_y = 7m$

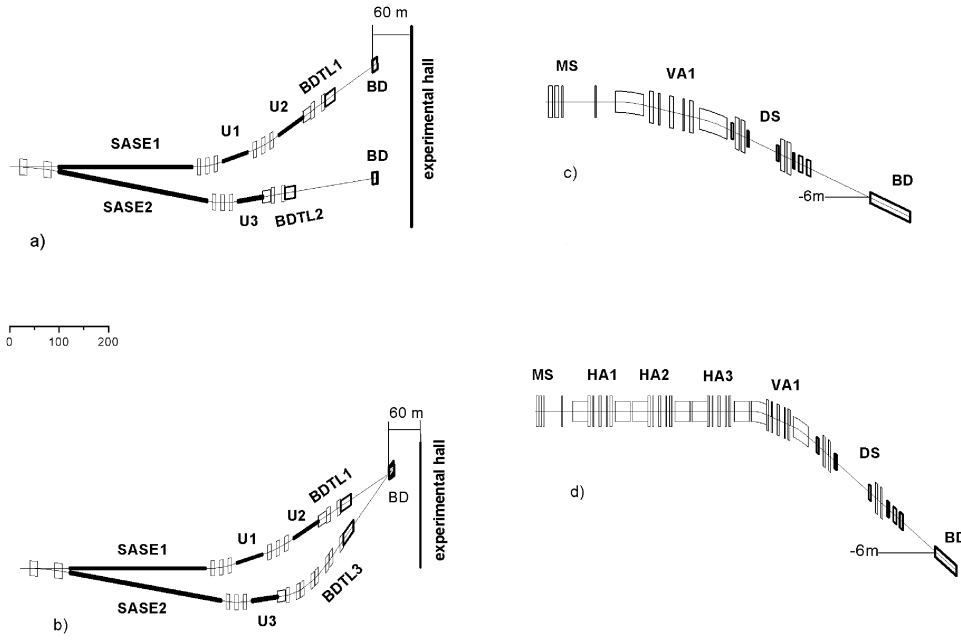


Figure 6.1: Layout of possible Beam Dump Transport Lines together with the beam distribution system. a,b - top views, c,d - side views.

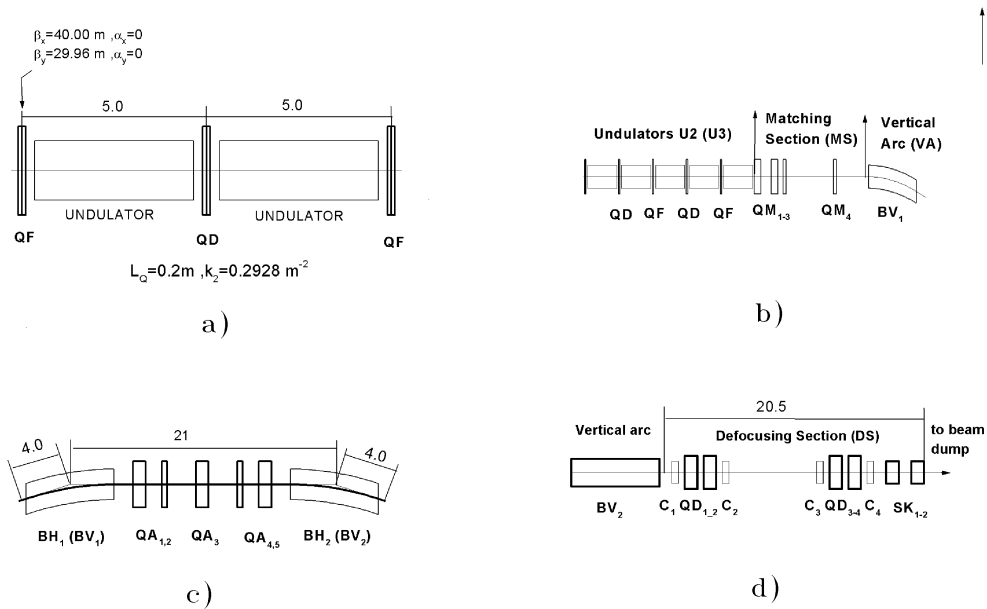


Figure 6.2: The optics schemes for the BDTL unified blocks. a) - undulator section, b) - matching section, c) - horizontal bending arc, d) - defocusing section.

Table 6.1: The optics specification for the Matching Section of the BDTL

Element	Length, m	Field gradient, T/m
Quad QF (undulator)	0.2	48.8317
Drift (undulator)	4.8	
Quad QM1	1.0	27.3714
Drift	0.56	
Quad QM2	1.0	-15.4286
Drift	0.8	
Quad QM3	0.4	-57.4143
Drift	7.94	
Quad QM4	0.4	61.1829
Drift	4.3	

at the entrance of the bending section of the BDTL. The initial values of the optical functions $\beta_x = \beta_y = 7m, \alpha_x = \alpha_y = 0$ are initial values of the periodic solution in the bending section. The beta functions along the MS are shown in Fig. 6.3 b. The optics specification for the MS is listed in the Table 6.1.

6.1.2 Bending arc

The bending part of the BDTL directs the beam to a beam dump input window and consists from a combination of several Vertical bending Arcs (VA) and Horizontal bending Arcs (HA). The bending arc (VA or HA) has a special design to preserve a drastic emittance growth. A two-bend, first-order achromatic system, Fig. 6.2c, is used as a unified block for a bending arc. The gradients of quads and the distances between magnetic elements are chosen to have equal beta functions ($\beta_x = \beta_y = \beta_{x0} = \beta_{y0}, \alpha_x = \alpha_y = \alpha_{x0} = \alpha_{y0}$) at a input and an output of a bending arc . It allows us to connect several bending arcs without any matching. Moreover, if the first arc serves for a vertical bend (VA), the second arc can be used for a horizontal bend (HA).

The specification of the bending arc of the BDTLs is listed in Table 6.2 (see also Fig. 6.1 for the BDTLs identification). The dispersion and the beta functions in one vertical arc are shown in Fig. 6.3a,6.3b , and these functions for the arcs sequence HA-HA-HA-VA are shown in Fig. 6.4a, Fig. 6.4b. Small values of beta functions in the bending magnets provide the reasonable $\approx 10\%$ beam emittance growth in each dipole due to synchrotron radiation. The second order rms beam envelopes are shown in Fig. 6.3c, along the sequence MS-VA and the sequence MS-HA-HA-HA-VA (Fig. 6.4c) for the beam energy spread of $\frac{\delta W}{W_0} = 2.0 \cdot 10^{-4}$, and beam reference energy $W_0 = 50GeV$ and $1.03 \cdot W_0$. The emittance dilution, taking into account second order effects, is less than two for a channel with four bending arcs.

6.1.3 Defocusing section

The bunch spot size should be increased to the required value by a special Defocusing Section (DS), Fig. 6.2d. To increase the beam spot size, further a sweeping system should be implemented in this section to shift the beam along the beam dump window within $\pm 10mm$ in a bunch train. The same kickers [29] as for the TESLA collider are used for

Table 6.2: Optics specifications for the Arc of the BDTL

Element	Length, m	Pole field, T Gradient, T/m	Bending angle degrees
Drift	0.5		
Dipole BV (BDTL1)	7.0	0.64484	1.551
Dipole BV (BDTL2)	7.0	0.37353	0.898
Dipole BH (BDTL3)	7.0	0.68040	1.636
Dipole BV (BDTL3)	7.0	0.66821	1.607
Drift	1.5		
Quad QA1	1.0	37.7503	
Drift	1.0		
Quad QA2	0.4	28.9143	
Drift	2.336		
Quad QA3	1.0	-51.0777	
Drift	2.336		
Quad QA4	0.4	28.913	
Drift	1.0		
Quad QA5	1.0	37.7503	
Drift	1.5		
Dipole BV (BDTL1)	7.0	0.64484	1.551
Dipole BV (BDTL2)	7.0	0.37353	0.898
Dipole BH (BDTL3)	7.0	0.68040	1.636
Dipole BV (BDTL3)	7.0	0.66821	1.607
Drift	0.5		

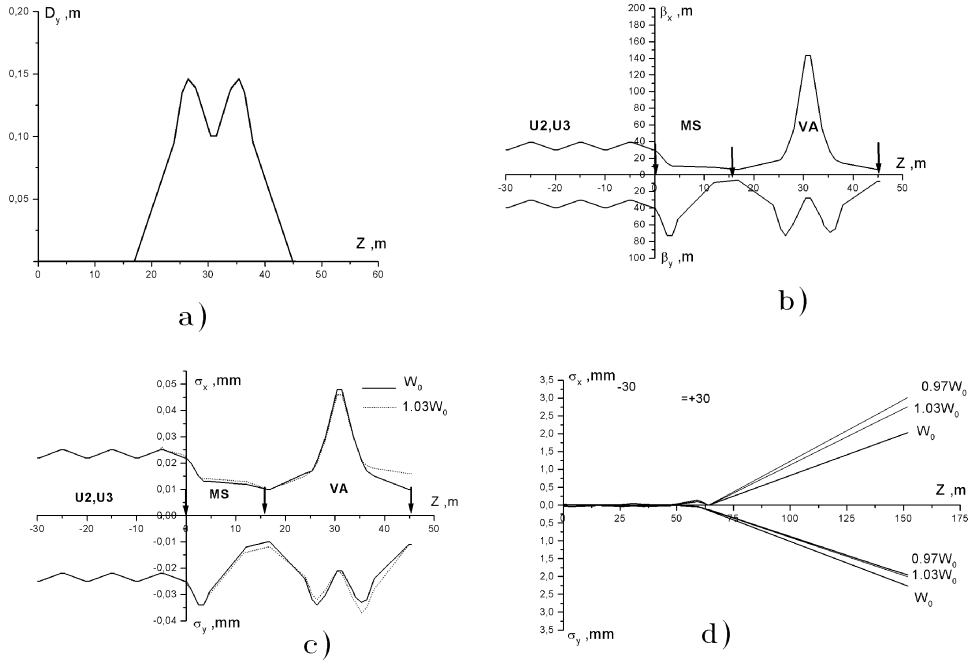


Figure 6.3: The optics properties for the matching and the bending sections of the BDTL1. a) - dispersion functions along bending arc, b) - beta functions along the MS-VA sequence, c) and d) - the second order rms beam envelopes along the MS-VA sequence and the total BDTL1.

this purpose. But the kicker length can be reduced to $1m$ to provide the necessary beam deflection.

The quads QD1 and QD2 have the same field gradient, as the quads QD3 and QD4, so this four quads are working as quadrupole doublets. The second order rms envelopes of beams with energies of $0.97W_0$, W_0 and $1.03W_0$ are shown in Fig. 6.3d in the BDTL1.

With a large magnification of the transverse bunch dimensions, the defocusing doublet increases in the same ratio also a beam center misalignment at the entrance of the defocusing section. Four $x - y$ steering magnets C1-C4 are used to correct the position of the beam center on the beam dump. The possible displacements of the beam center at the entrance of the defocusing section in $(x - x')$ and $(y - y')$ planes which can be corrected by the steering magnets with a bending angle $\sim 0.5mrad$ are shown in Fig. 6.5.

Two sweeping kickers [29] SW1 and SW2, vertical and horizontal with a bending angle of $0.24mrad$, are located about $70m$ upstream from the beam dump. Powered with $1kHz$ sinusoidal current with a phase shift of 90° between horizontal and vertical kickers, the pair of kickers provides a distribution of the beam in a circle with a radius of $16mm$. The optics specification of the defocusing section of the BDTL is listed in Table 6.3 .

6.2 Scheme1: One beam dump for one beam line

To ensure the radiation safety requirements, the beam dump should be placed $6m$ deeper than beam delivery system (see Chapter 4) and $60m$ before the experimental hall. A

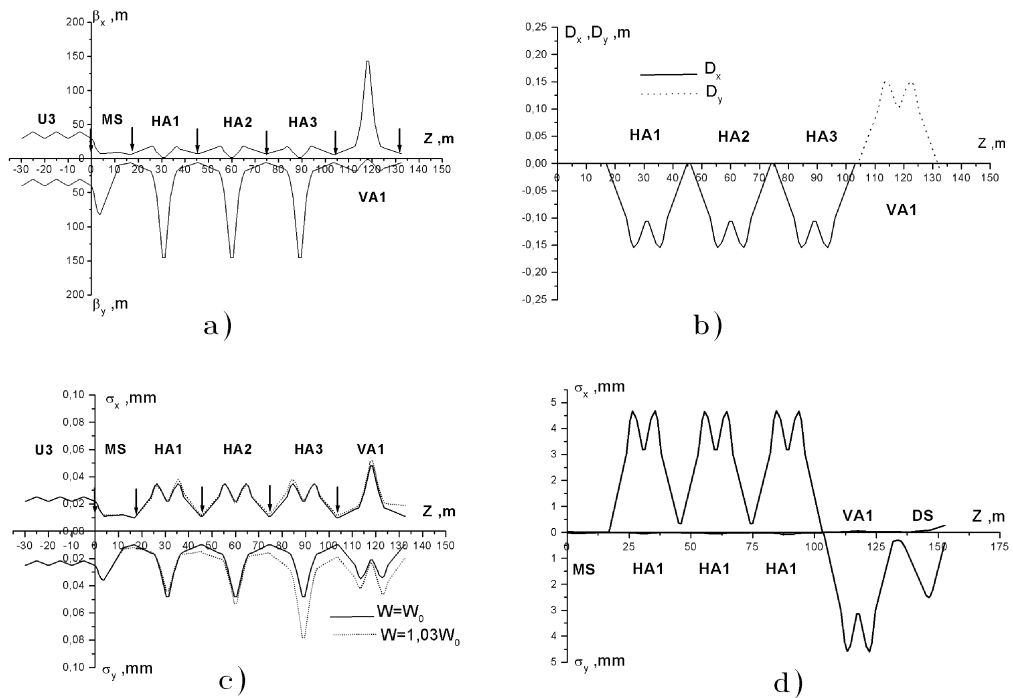


Figure 6.4: The optics properties for the matching and the bending sections of the BDTL3. a) - the beta functions, b) - the dispersion, c) - the partial rms beam envelopes (without DS), d) - the bunch displacement and spot size.

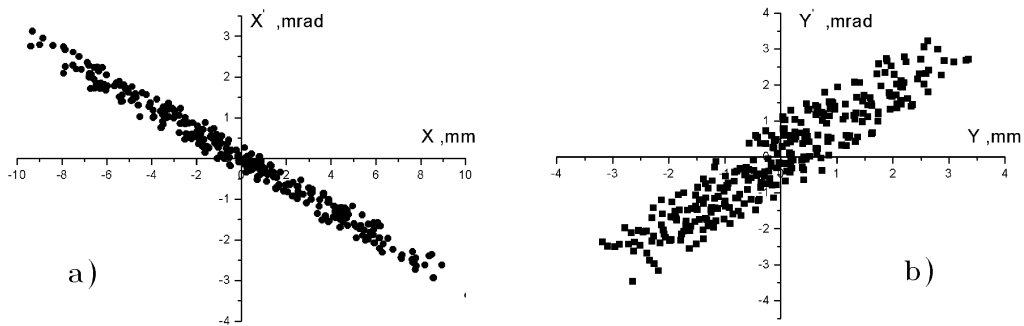


Figure 6.5: Entrance alignments of a beam axes at an entrance of defocusing section which can be corrected by steering system.

Table 6.3: Optics specifications for the Defocusing Section of the BDTL

Element	Length, m	Pole field, T Gradient, T/m	Bending angle, mrad
Drift	0.5		
Corrector C1	0.5	0.16	0.5
Drift	1.5		
Quad QD1	1.0	-60.00	
Drift	0.5		
Quad QD2	1.0	-60.0	
Drift	0.5		
Corrector C2	0.5	0.16	0.5
Drift	7.0		
Corrector C3	0.5	0.16	0.5
Drift	0.5		
Quad QD3	1.0	45.0	
Drift	0.5		
Quad QD4	1.0	45.0	
Drift	0.5		
Corrector C4	0.5	0.16	0.5
Drift	1.0		
Sweeping kicker SK1	1.0	0.04	0.24
Drift	1.0		
Sweeping kicker SK2	1.0	0.04	0.24
Drift to BD (BDTL1)	75.86		
Drift to BD (BDTL2)	156.35		
Drift to BD (BDTL3)	71.98		

relatively simple way is to have a beam dump for every distribution line BDTL1 and BDTL2. (Fig 6.1a, 6.1c). Both beam lines the BDTL1 and the BDTL2 contain matching, vertical bending arcs and defocusing sections. The optical properties of these sections are described above in this chapter. The lines BDTL1 and BDTL2 differ in the length by $\approx 100m$ (see Fig. 6.1) and the critical case is the BDTL1 line after the undulator U2.

6.3 Scheme2: One beam dump for two beam lines

The beam dump is an expensive device and it is necessary to consider the case of the beam absorption in one dump of at least from two lines - BDTL1 and BDTL2. Additionally to the vertical bends, a horizontal bend is required. The side and top views of beam transport from undulators U2 and U3 in a common beam dump are shown in Fig 6.1b, 6.1d. The beam transport line from the undulator U2 doesn't change. In the beam transport line from U3 three horizontal arcs are added. The first order transformation matrix of the three arcs is equal to $+I$ in both x and y -planes. So, the first order properties of BDTL3 is very close to that of BDTL1. The second order calculations give 1.3 times increasing of the beam spot size on the beam dump input window as compared to BDTL1.

The angle between the axes of BDTL1 and BDTL3 on the input of the beam dump is equal $\approx 100mrad$. It looks like the minimal value to be achieved within the given space restrictions. However, the beam dump can be further displaced along the experimental hall. In this case the BDTL1 lines should be changed by adding a HA arc, but the angle between the beams axes of BDTL1 and BDTL2 doesn't decrease.

The envelopes in the matching, bending and defocusing section of the channel for a beam with energy spread of $\pm 3\%$ are shown in Fig. 6.4d.

6.4 Summary

The optical scheme for the beam dump lines has a block structure. Several unified blocks - a matching section, a bending arc and a defocusing section, allow to construct practically arbitrary lines. The option 'one line one dump' is the simplest one. Taking into account the high dump cost, the option 'two lines in one dump' is also proposed. Solutions are found for both options within the space limitations and can be fitted for larger distances with a relaxation of the magnet parameters.

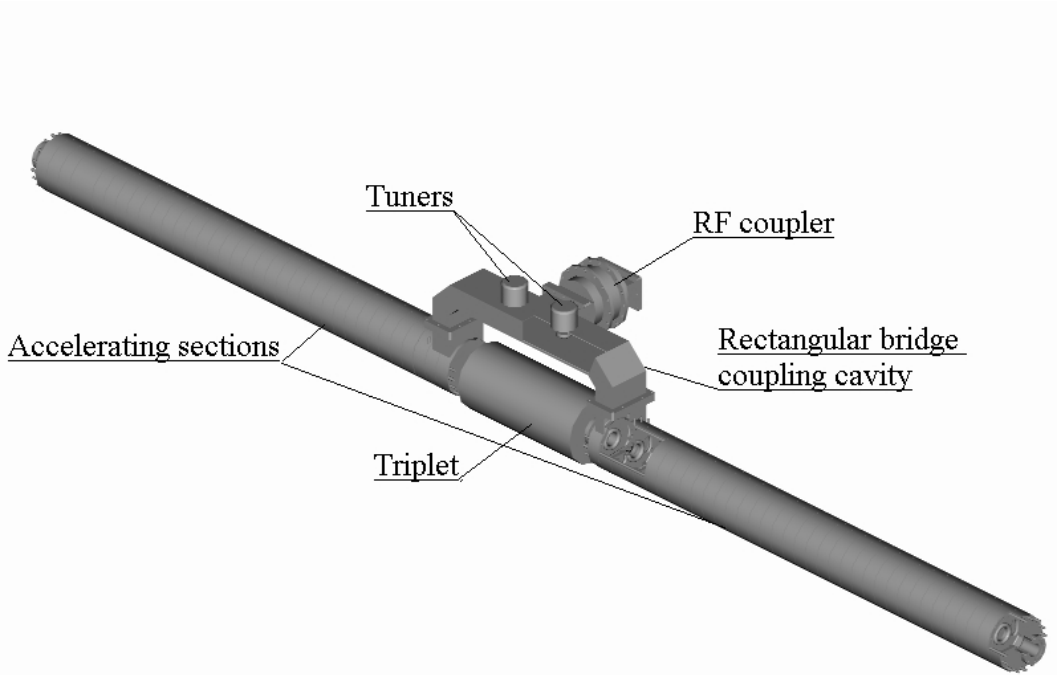


Figure 7.1.1: The normal conducting accelerating cavity for the TESLA Positron Pre-Accelerator.

7 Post accelerator

The energy modulation for the electron beam can be performed either by changing the accelerating field in the TESLA main linac (before the e^- beam extraction) or by a special post-accelerator. The energy modulation depth and velocity depend on rise time of the accelerating cavities τ_l and achievable accelerating gradient $E_0 T$.

As compared to super-conducting cavities, the normal conducting cavities have a much smaller rise time of $\tau_l \approx 3\mu s$ for L-band operation and can provide a faster energy modulation.

7.1 Accelerating structure and RF system

Normal conducting accelerating cavities are foreseen in special points of the TESLA linear collider, for example in the Positron Pre-Accelerator (PPA) of the TESLA positron source, see [30], [31]. The CDS accelerating structure (see [30] and related references) is proposed for the PPA accelerating system. A general view of the cavity for the second PPA part is shown in Fig. 7.1.1.

For possible applications as post-accelerator it is reasonable to use the same normal conducting accelerating structure as for other specific parts of the TESLA and the standard TESLA rf hardware, including a 10 MW klystron.

The shape of the CDS structure cells were optimized to yield a maximum effective shunt impedance Z_e at the given values of the aperture diameter $2a$ and accelerating gradient

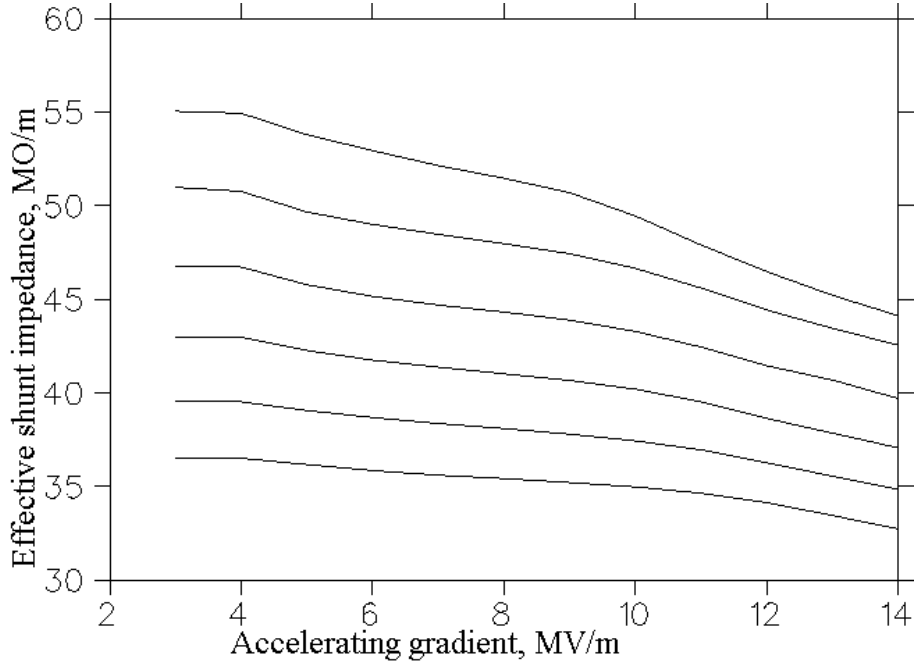


Figure 7.1.2. Z_e dependencies on E_0T for a CDS cell with different aperture radii. Up to down - $a = 12mm, 15mm, 18mm, 21mm, 24mm, 27mm$.

E_0T [30]. The dependencies of the effective shunt impedance Z_e on E_0T for a CDS cell with different aperture radii are shown in Fig. 7.1.2. For the post-accelerator we don't need the large aperture diameter of 46 mm as for the PPA [31] and a value of $2a = 24mm$ is possible. For $E_0T \sim (8 \div 10)MeV/m$ one has $Z_e \approx 50M\Omega/m$.

7.2 Energy modulation depth

Let consider some general relations to understand the limitations for the depth and the velocity of the beam energy modulation. With the rf power P_{rf} available from the klystron the energy gain ΔW_a obtained with the accelerating cavity L_c in length is:

$$\Delta W_a = \sqrt{P_{rf} Z_e L_c}. \quad (18)$$

Any energy gain can be obtained at the expense of the required length (with an accelerating gradient E_0T as a parameter). Because the space is limited, lets consider a reasonable case when the klystrons are placed horizontally in the same tunnel as the accelerator. The length of the klystron hardware (together with a pulse transformer) is about $\approx 6m$. Lets consider this value as the length of one module - accelerating cavity and the rf hardware. Supposing a length of 0.5 m for focusing elements, the cavity length L_c is $\approx 5.5m$, $P_{rf} = 9.0MW$, $E_0T = 9MV/m$, $\Delta W_a = 50MeV$. Under these assumptions an energy modulation of $\pm 50MeV$ can be obtained with one module.

7.3 Energy modulation velocity

The electron energy modulation follows the electric field amplitude and phase change. The possible velocity of the field change depends on the available rf power, because for

the time of the energy modulation one needs to withdraw "old" electro-magnetic field from the cavity and replace it by a "new" field, within the cavity and rf system bandwidth. In case of the TESLA normal conducting cavities the limiting factors are the rf power and the cavity bandwidth, because the klystron bandwidth of $7MHz$ exceeds the own cavity bandwidth of $65kHz$ several times. Together with the fast modulation, we need a controllable field change in the cavity. The control can be performed either by amplitude or phase modulation of the driving rf power. The phase modulation has a wider spectrum and is more complicated in the practical realization.

Lets consider the algorithm for the TESLA rf system with digital control. It means that the rf control system has small, but finite time steps of discretization t_d to represent any signal. During this time step every driving signal is assumed as constant value. Let us describe the driving signal $E^{dr}(t)$ as a sum of several steps. After n steps, during the time $(n-1)t_d \leq t \leq nt_d$ the driving rf signal is:

$$E^{dr}(t) = 1 + \sum_{k=1}^n \Delta_k, \quad (19)$$

where Δ_k is the change for the rf driving signal during the k -th step. The field amplitude in the cavity is:

$$E_c(t) = 1 + \sum_{k=1}^{n-1} \Delta_k (1 - e^{-\frac{t}{\tau}}) + \Delta_n (1 - e^{-\frac{t-(n-1)t_d}{\tau}}) \quad (20)$$

Suppose we want to realize the time dependence of the field amplitude in the cavity as $F(t)$. Lets choose the steps in the driving rf signals Δ_n to minimize the deviation between $F(t)$ and $E_c(t)$ during the time $(n-1)t_d \leq t \leq nt_d$ as:

$$\frac{\partial \int_{(n-1)t_d}^{nt_d} [F(t) - E_c(t)]^2 dt}{\partial \Delta_n} = 0 \quad (21)$$

with the limitation $|\Delta_n| \leq 1.0$ from the rf power capability. Lets consider two examples with the parameter α , describing the modulation velocity in terms of the cavity rise time τ :

$$F(t) = \cos\left(\frac{\pi}{\alpha\tau}\right), \quad (22)$$

$$F(t) = 1 - \frac{2}{\alpha\tau},$$

At Fig. 7.3.1 the plots for the deviation Δ_S :

$$\Delta_S = \frac{\int_0^{\alpha\tau} [F(t) - E_c(t)]^2 dt}{\int_0^{\alpha\tau} [F(t)]^2 dt} \quad (23)$$

in the dependence on α are shown for both cases. From these plots one can conclude, that during the time interval $(3 \div 4)\tau$ or $\approx (9 \div 12)\mu s$ the field in the cavity can be changed by the standard rf channel with a small deviation from the desired voltage dependence.

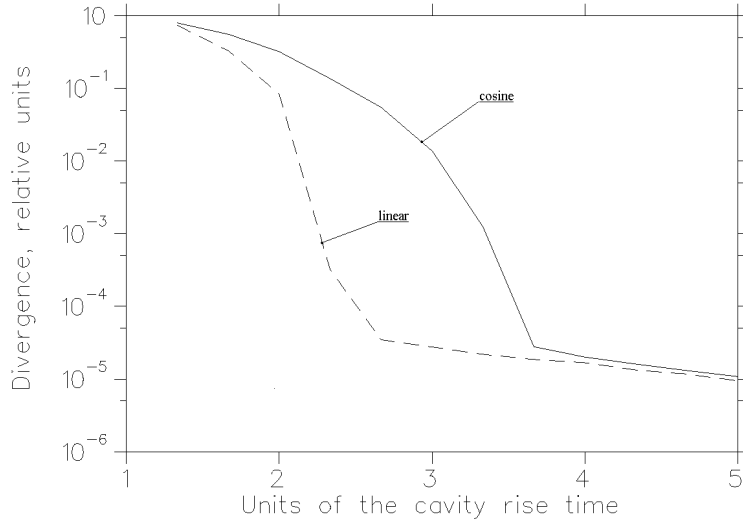


Figure 7.3.1: The relative deviation between driving signal and cavity voltage.

7.4 Summary

The post accelerator before the FEL beam delivery system has all rights to be considered as a solution to provide the electron beam energy modulation. Before the post accelerator the transfer line, collimation system and arcs are simplified, because the well known solutions for beams with a narrow energy spread can be applied. The accelerator can be placed in the tunnel replacing two vertical arcs. These arcs have to be combined with the post accelerator. It is attractive to consider the same accelerator simultaneously for two lines - the high and the moderate energy lines, combining the beam before the accelerator and splitting after them. In this case the combined arc-accelerator optics should be pulsed. Additionally the post accelerator can be used to correct the beam loading change in the main TESLA linac, for example for increasing of the bunch number in the train.

The post accelerator is not the cheapest solution, because one rf channel needs to change the beam energy $\pm 50 MeV$. For a wide range of $\pm 5\%$ energy modulation of the $50 GeV$ beam it is an impractical option, because 50 rf channels distributed in a more than 300 m long tunnel are required. For a narrower range and lower energy $\approx \pm 3\%$ at $30 GeV$ it can be considered, at least to understand the price for different options.

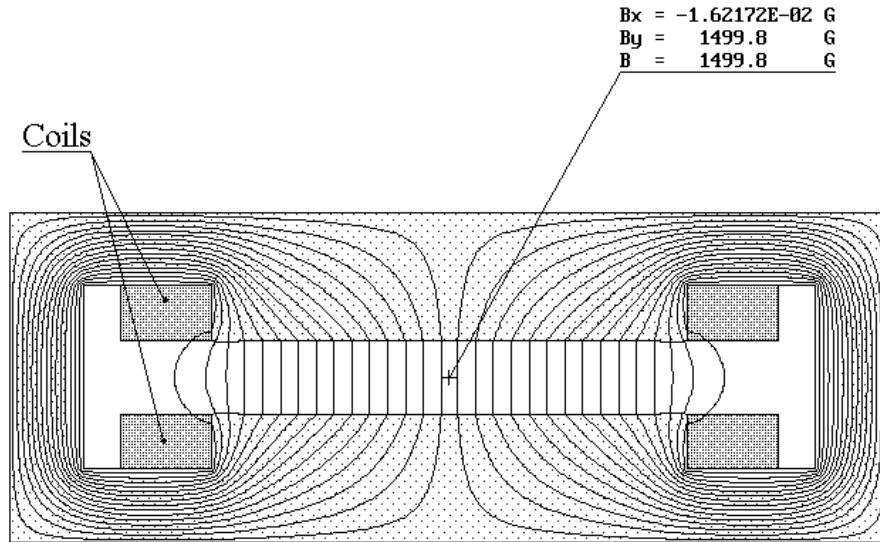


Figure 8.1.1: The cross-section and the field distribution for the dual mode magnet design.

8 Magnetic elements

8.1 Pulsed magnets

The pulsed magnets in the beam distribution system should operate with a repetition rate of 2.5Hz and have a flat-top $\approx 1\text{ms}$. To prevent emittance and energy spread growth, the magnetic field inductance is chosen not so high, $B = 0.015\text{T}$ at the expense of the magnet length $L = 15\text{m}$. These parameter specification allows to propose a dual mode pulsed magnet design for operation both in pulsed and in DC mode. The dual mode operation allows us to use the same bending magnet in the beam delivery system (pulsed mode) and to bend the beam to the commissioning beam line.

For pulsed mode operation the magnet yoke should be made from low-carbon steel laminates and the coil winding should have an electrical insulation to keep a high pulsed voltage during the pulse. These requirements are usual for pulse magnets. In the DC mode the total power, dissipated in the coil, is high and water cooling is necessary. During the pulsed mode operation the coil cooling is useful for the stabilization of the coil resistance. To bend a beam in different directions, the magnet poles should have a sufficient width.

The proposed design of the magnet is shown in Fig. 8.1.1. The main parameters are listed in Table 8.1.1. To reduce the coil inductance, the number of windings is chosen to be 4. The winding are made from square cable $16 \cdot 16\text{mm}$, with a cooling channel (diameter 10 mm) inside. In the 22cm wide region the field uniformity is better than $0.07 \cdot 10^{-4}$. Due to the low operating field, there are no limitations due to saturation in the steel. The outer dimensions of the yoke are small ($\approx 0.2 \cdot 0.4\text{m}$) and the main problem in the design and construction of this magnet is the large length. During the technical development

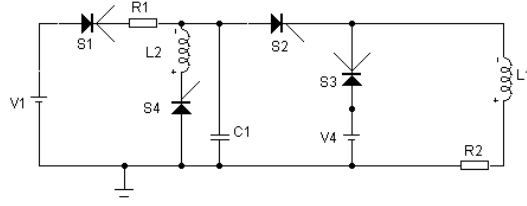


Figure 8.2.1: The general scheme of the pulse power supply.

the possibility to divide this magnet in several sections should be considered.

8.2 Pulse power supply scheme.

The pulsed power supply source, together with the pulsed magnet, should realize the field pulse with stable (field stability $\approx 10^{-4}$) and long (not less than $1ms$) flat-top with a repetition rate of $2.5Hz$.

The scheme for the pulse power supply is shown in Fig. 8.2.1. Such schemes are widely used for pulse power sources if a long pulse flat-top is required.

The design idea of the scheme is the oscillating discharge of capacitance C_1 into the magnet coils, represented as the inductance L_1 and resistance R_2 . The capacitor C_1 is charged in the time frame between pulses from the main power source V_1 to a high voltage, defined by the pulse length and the coils inductance L_1 through the switch S_1 . This switch is

Table 8.1.1: Dual mode magnet design.

Parameter	Unit	Pulsed mode	DC mode
Magnetic field inductance	T	0.15	0.15
Field stability	%	0.01	0.01
Length	m	15	15
Gap	mm	40	40
Current	A	605	605
Voltage at the coils	V	2450	15.2
Average power dissipation	kW	0.1	9.50
Inductance	mH	9	9
Coil resistance	Ω	0.025	0.025
Number of windings		4	4
Cooling water consumption	$\frac{m^3}{h}$	-	1.2

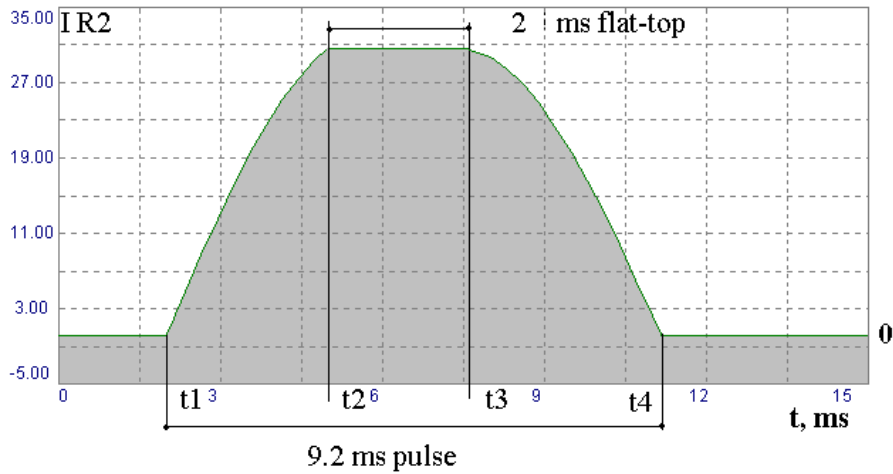


Figure 8.2.2: The pulse shape for the current in the pulse magnet coils.

closed during the pulse, and the switch S_2 is opened. The capacitor discharge begins at the time t_1 (see Fig. 8.2.2). When the discharge current (the current through the magnet coils) practically reaches a maximal value, and hence the voltage at the coils is low, the DC stabilizing source V_4 connects through the switch S_3 to the coils, providing the flat-top formation and stabilization, at the time t_2 . During the time period from t_2 to t_3 (the pulse flat-top), a DC current flows through the coils, depending on the coil resistance R_2 and the source voltage of V_4 . After the time t_3 the switch S_3 closes and the capacitor discharge continues to the time t_4 . When the current pulse formation finishes ($t \geq t_4$, the voltage at the capacitance C_1 has the opposite sign. To reduce the charge current from the main power source V_1 , the recuperation branch (the inductance L_2 and switch S_4) are foreseen.

To reduce the pulse voltage at the coils, the pulse length is chosen large ($9.2ms$). As the switches S_1, S_2, S_3 either GTO thyristors, or IGBTs may be used.

The total pulse shape for the current (for the $R_2 \cdot I_c$ product) in the magnet coils is shown in Fig. 8.2.2.

The main parameters of the pulse power supply are as follows - the main power supply voltage is $4.9kV$, maximum current (taking into account the recuperation scheme) is $1A$, the voltage of the DC power supply is $33.6V$, the current is $605A$, the maximal current through the coils. The capacitor C_1 has $320\mu F$ capacitance, the current pulse is $9.2ms$ with a flat-top of $2.0ms$.

The parameters of all elements are adjusted to have the highest pulse flat-top stability within reasonable specifications. The current stability is defined by the precision of the voltage set-up and the DC power supply stability, the precision of the time control for the switches (mainly S_3), the magnet parameter stability and the precision of the current and voltage measurements. The usual modern DC power supplies have a stability of the

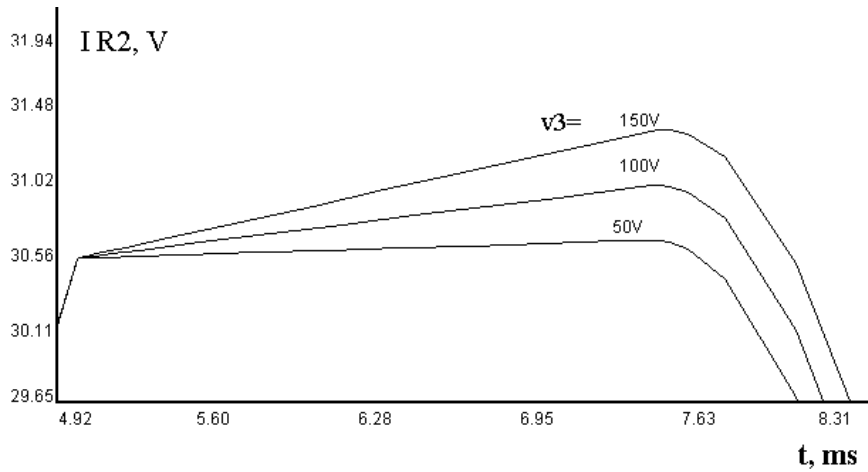


Figure 8.2.3: The pulse flat-top change with the increasing of the DC power supply voltage.

order 10^{-4} and of the order 10^{-5} in the case of a special order. With modern digital technique the voltage can be measured with a precision of the order 10^{-5} . The magnet design parameters ensures comfortable operating conditions - far from the iron saturation point and with low coil temperature.

As for the DC source V_4 parameters, the requirements for the stability are not rigid, due to the parameters of the other elements. To provide a visible change in the output current and a linear change of the flat-top in time, a significant change in the voltage V_4 is needed, as it is shown in Fig. 8.2.3.

Simulations with the Micro-Cap V code for the pulse formation process and flat-top stabilization show the possibility to fulfill the design parameters with a flat-top stability of the order 10^{-5} . Taking into account realistic parameters of elements for modern power electronic components, a flat-top stability 10^{-4} is possible.

The same DC power supply as for the pulse flat-top stabilization is supposed for DC operating mode of the magnet. If the pulsed magnet together with the power supply V_4 will be used in DC mode to bend the electron beam to the diagnostic commissioning line, an improved stability for the DC source is required and the DC source should be ordered specially. For example, the NTN 28000 DC power source, manufactured by F.uG Elektronik GmbH, has a voltage and current stability of the order $< 10^{-4}$ ordinary and of the order 10^{-5} with special order.

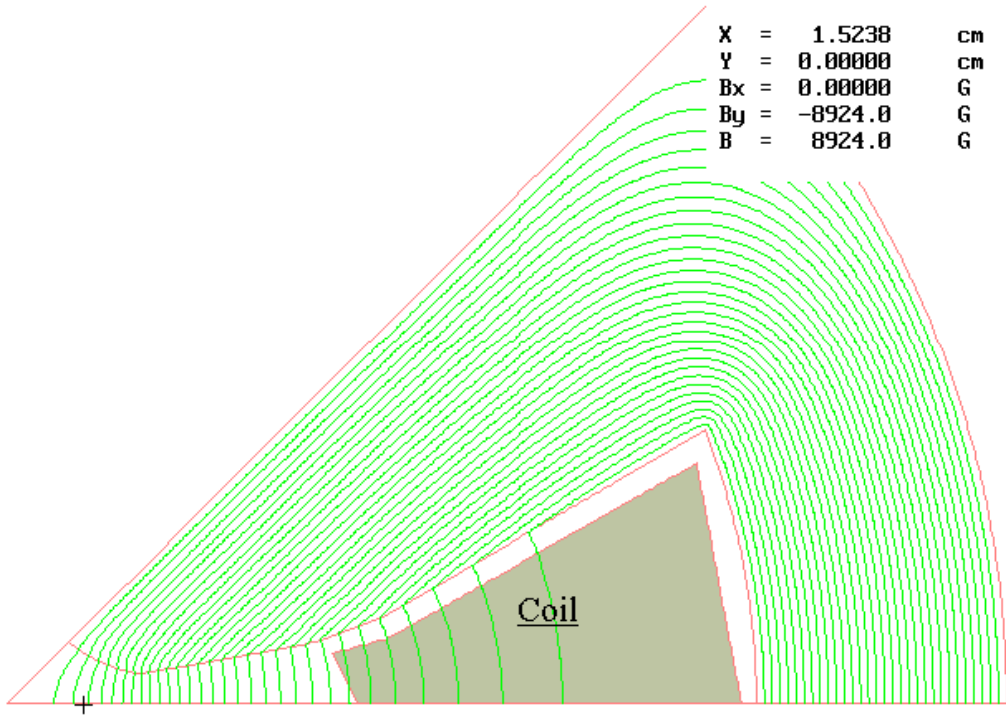


Figure 8.3.1: The cross-section and the field distribution for the high gradient quadrupole lens.

8.3 Parameters of DC magnetic elements and power requirements

Due to requirements of the energy spread and the emittance growth preservation all the bending magnets in the Energy Collimation (EC) system, arcs, Beam Delivery Lines (BDLs), Diagnostic Commissioning Line (DCL) realize a moderate inductance value at the expense of the magnet length. The low inductance value in the bending magnets leads to comfortable operating conditions. The magnet length of $(5 \div 7)m$ is not a problem. As for longer $\approx 15m$ dipoles, the technical design might foresee these magnets form several parts. All bend magnet are assumed with the gap of $40mm$ - also leading to the DC power reduction.

All lenses are assumed with bore hole diameter of $35mm$ and maximal magnetic field at the poles not higher than $1T$.

The gradients of the main part of quadrupole lenses are in reasonable limits and there are no limitation for the technical design. For the lenses with high gradient $G \sim 58T/m$ a special pole shape (Fig. 8.3.1) should be foreseen.

Both sextupole and oktupole lenses (Fig. 8.3.2 and Fig. 8.3.3) operate in comfortable conditions and there is a reserve for increasing the magnetic field.

There are a lot of magnetic elements in the different parts of the lines, which are considered in this report. For the detailed information one has to see Chapters 3, 4, 5, 6. The data to estimate the magnet parameters in the DC power and cooling water

Sextupole Magnet

X = 1.4985 cm
Y = 0.00000 cm
Bx = 0.00000 G
By = -3971.5 G
B = 3971.5 G

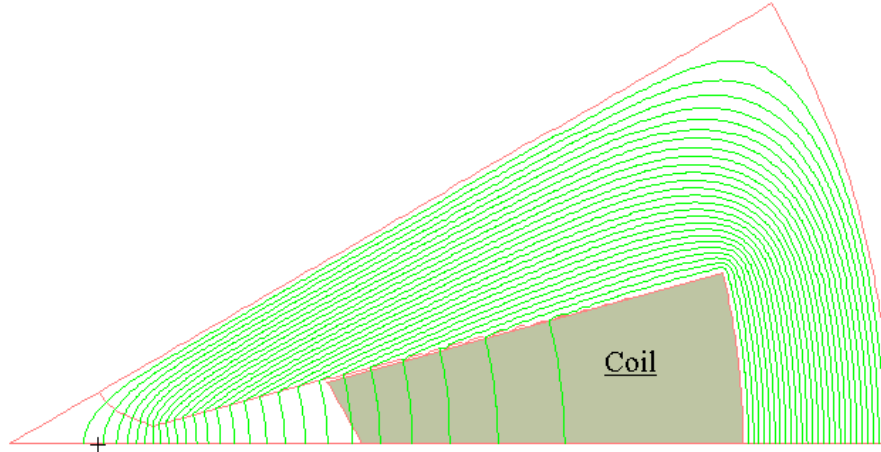


Figure 8.3.2: The cross-section and the field distribution for the sextupole lens.

Octupole Magnet

X = 1.4985 cm
Y = 0.00000 cm
Bx = 0.00000 G
By = -798.98 G
B = 798.98 G

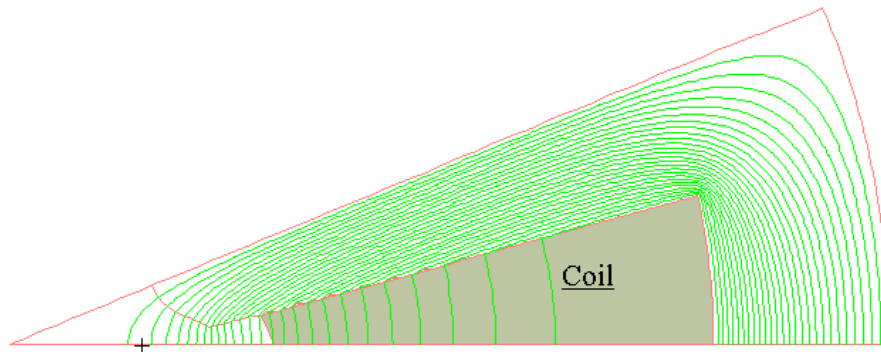


Figure 8.3.3: The cross-section and the field distribution for the oktupole lens.

consumptions for the different elements are presented in Table 8.3.1, where: L_e is the effective length of the element, B, G are the inductance and the gradient for bending magnets (B) or quadrupoles (Q) respectively, N_u is the number of units, I is the current, P_{DC}^{un} is the DC power per unit, P_{DC}^{to} is the DC power for the group of elements, V_c is the cooling water consumption.

For the beam elevation system (Fig. 3.1.1) a total consumption is presented. As for a beam delivery system, the DC power requirement and cooling water consumption are shown for different parts separately (see Fig. 4.1.1). The same consumptions for the beam dump line are shown for the arc ADL, separately, because the total consumption depend on the adopted beam line scheme.

8.4 Summary

Due to the requirements of the energy spread and the emittance preservation all the bending magnets in the transport lines before the undulators realize a moderate inductance value at the expense of the magnet length. The low inductance value in the bending magnets leads to comfortable operating conditions. The magnet length of $(5 \div 7)m$ is not a problem. As for longer $\approx 15m$ dipoles, the technical design should foresee these magnets form several parts. All lenses are assumed with a maximal magnetic field at the poles not higher than $1T$. The gradients for the main part of quadrupole lenses are in reasonable limits and there are no limitation for the technical design.

The dual mode pulse magnet design is proposed for operation both in pulse and in DC mode. The dual mode operation allows us to use the same bending magnet in the beam delivery system (pulse mode) and to bend the beam to commissioning beam line.

The pulse power supply scheme is proposed to provide the current pulse with stable (field stability $\approx 10^{-4}$), enough long ($\approx 2ms$) flat-top with repetition rate $2.5Hz$, ensuring a reasonable pulse voltage value at the coils.

Table 8.3.1: Parameters of DC magnetic elements

Part	Type	$L_e,$	B, G	N_u	$I,$	$P_{DC}^{un},$	$P_{DC}^{to},$	$V_c,$
		m	$T, \frac{T}{m}$		A	kW	kW	$\frac{m^3}{h}$
EC	B	15.0	0.136	4	600	9.5	38	4.8
	Q	0.8	15.19	10	390	2.0	20	2.0
	S	0.4	614	6	390	1.6	0.8	0.3
Subt.							59	2.94
TC	Q	1.0	1.05	12	8	0.1	1.2	
Subt.							1.2	
A1	B	4.7	0.081	128	435	3.0	384	52.2
A1	Q	0.8	29.35	64	390	4.0	256	20.5
A1	Q	0.8	34.69	64	460	5.5	352	20.5
AM1	Q	0.8	29.35	4	390	4.0	16	1.3
AM2	Q	0.8	16.68	2		1.3	2.6	1.3
AM2	Q	0.8	5.5	2		0.14	0.3	
A1	S	0.2	1025	64		0.57	36.5	10.2
A1	S	0.2	1824	64	520	3.4	115	10.2
Subt.							1163	116
D2	B	7.0	0.36	3	1000	19	57	3.42
D2	Q	0.8	25.35	4	340	3.0	12	1.3
D2	Q	0.8	58.21	2	715	12	24	1.02
D2	S	0.4	1277	2	390	1.6	3.2	0.3
D2	O	0.4	22392	2	150	1.8	115	10.2
D2	Q	0.8	18.51	10	390	1.6	16	3.2
Subt.							227	20.0
D1	Q	0.8	29.19	2	390	4.0	8	0.64
D1	Q	0.8	58.37	4	720	12.5	50	2.0
D1	S	0.4	614	2		0.4	0.8	0.3
D1	O	0.4	7597	2		0.04	0.08	
Subt.							59	2.94
M2	Q	0.8	30.0	7	400	4.16	29.12	2.23
M3	Q	0.8	30.0	7	400	4.16	29.12	2.23
Subt.							58.3	4.46
DCL	B	15.0	0.136	1	600	9.5	9.5	1.2
DCL	B	7.0	0.36	2	1000	19	38	2.3
DCL	Q	0.8		15			60	4.5
Subt.							107	8.0
ADL	B	8.0	0.7	2	1500	76	152	5.0
ADL	Q	0.8	51.00	5	720	10.5	52	4.0
Subt.							204	9

9 Conclusion

The important parameter for all transport and distribution lines for the FEL facility is an energy acceptance. All the systems should satisfy to contradictory scientific requirements, together with a space limitations and cost reduction wishes. In this report the results of the study for the collimation, the elevation and the distribution and the beam absorption lines are presented.

The titanium spoiler together with the copper absorber are chosen as a collimator for the FEL transport line. The collimation efficiency is at least 10^{-6} if there are no focusing elements in between. The radiation dose distribution is estimated together with safety requirements.

The FODO optics scheme is chosen for the transverse energy collimation combining the collimation efficiency, spoiler survival conditions and energy acceptance requirements.

A special optics for energy protection collimation is recommended.

The elevation arcs and the beam distribution lines are optimized in the limited space requirements and ensure $\pm 5\%$ energy acceptance.

The special commissioning beam line has all possibilities for the measurements of all relevant beam parameters and calibrations of another beam diagnostic monitors.

The post accelerator before the FEL beam delivery system has all rights to be considered as a solution to provide the electron beam energy modulation.

The optics scheme for beam dump lines has a block structure. Several unified blocks - the matching section, the bending arc and defocusing section, allow to construct practically arbitrary reasonable line. The option one line - one dump is a simplest one. Taking into account a high dump cost, the option two lines in one dump is also proposed.

All magnetic elements are assumed with a maximal magnetic field at the poles not higher than $1T$ and there are no limitation for the technical design.

The dual mode pulse magnet design is proposed for operation both in pulse and in DC mode. The pulse power supply scheme is proposed to provide the current pulse with stable (field stability $\approx 10^{-4}$), enough long ($\approx 2ms$) flat-top with repetition rate $2.5Hz$, ensuring a reasonable pulse voltage value at the coils.

References

- [1] Conceptual Design of a 500 GeV e^+e^- Linear Collider with Integrated X-ray Laser Facility. DESY 1997-048
- [2] D. Walz. Justification for temperature rise and thermal stress limit. SLAC-NLC-Note-22, 1996
- [3] W.R. Nelson et al., Radiation calculations and shielding considerations for the design of the Next Linear Collider. SLAC-PUB-7336, 1996
- [4] I.S. Baishev, N.V. Mochov Space distribution of electron-photon shower energy deposition. IHEP Preprint 79-124, Serpukhov, 1979
- [5] J. Irwin et al., Optimizing a nonlinear collimation system for future linear colliders. SLAC-PUB-5507, 1991
- [6] P. Tenenbaum et al., Studies of beam optics and scattering in the next linear collider post-linac collimation system. Proc. of the Linac 2000 Conf., Monterey, CA, USA, 2000, (to be published).
- [7] G. Wustefeld, Transfer line, TESLA TDR meeting, Zheutun, 2-9 February 2000, DESY, 2000
- [8] J. Frish et al., Advanced collimator systems for the NLC. Proc. of the Linac 2000 Conf., Monterey, CA, USA, 2000, (to be published).
- [9] P. Tenenbaum et al., Direct measurement of geometric wakedields from tapered rectangular collimators. Proc. of the Linac 2000 Conf., Monterey, CA, USA, 2000, (to be published).
- [10] J. Tuizzolo et al., Magnets for the National Spallation Neutron Source accumulator ring. Proc. of the PAC97 Conf., p. 3233, 1998
- [11] S.H. Rokni et al., Radiation protection systems for the final focus test beam. SLAC-PUB-95-6784, 1995
- [12] M.M. Kolmochkov, V.N. Lebedev Practical handbook for radiation safety at particle accelerators. Energoatomizdat, Moscow, 1986 (in Russian).
- [13] K. Brown et al., TRANSPORT-a Program to Compute Charge Particle Beam Transport System, CERN 73-16.
- [14] B.C. Brow et al., The design and manufacture of the Fermilab Main Injector dipole Magnets. Proc. of the EPAC92 Conf., p. 1376, 1993
- [15] D. Woodley, P. Emma. Measurement and Correction of Cross-Plane Coupling in Transport Lines, Proc. of the Linac 2000 Conf., Monterey, CA, USA, 2000, (to be published).
- [16] R.S. Larsen et al., A Precision Toroidal Charge Monitor for SLAC, Symposium on Beam Intensity Measurements, Daresbury, 22-28, 1968.

- [17] 2. D. Yount, A High-Precision Faraday Cup and Quantameter for SLAC, SLAC-PUB 398, 1968
- [18] J.Camas et al., High Sensitivity Beam Intensity and Profile Monitors for SPS Extracted Beams, Proc. PAC 1993, p. 2498, 1994
- [19] A. Peters et al, A Cryogenic Current Comparator for Nondestructive Beam Intensity Measurements, Proc. EPAC 1994, p. 290, 1994.
- [20] R.Shafer, Beam Position Monitoring, AIP Conference Proceedings 212, 1989, p.26
- [21] T. Shintake, Development of Nanometer Resolution RF-BPMs, Proc. of the XII High Energy Accelerator, HEACC'98, Dubna, 1998,
- [22] C.Yan et al., Beam Energy Measurement Using the Hall C Beam Line, Proc. PAC 1993, p.2136.
- [23] K. Wittenburg, Conventional wire scanners for TESLA, DESY note, DESY 12-23-2000, 2000.
- [24] A.Burns et al., Wire Scanner News from the CERN - SPS, Proc. PAC 1989, p. 1580, 1990.
J. Camas et al., Observation of Thermal Effects on the LEP Wire Scanners, Proc. PAC 1995, p 2649, 1996
- [25] R.A. Erickson, Monitoring in Future e+e- Colliders. in Lecture notes in Physics, 343, Frontiers of Particle Beams. Springer-Verlag, Berlin, Heidelberg, 1989.
- [26] A.M. Tron, Private Communication. 09.10.2000.
- [27] A.M. Tron, Limitations at Short Bunch Length Monitoring, Proc. of the PAC 99 Conf. New York, p.2190, 1999.
- [28] D.X. Wang, G. A. Kraft, Measuring Longitudinal Distribution and Bunch Length of Femtosecond Bunches with RF Zero-Phasing Method, Proc. LINAC 1998, p.2020
K.L.F. Bane, et al. Measurement of Longitudinal Wakefield and Bunch Shape in the SLAC Linac, SLAC-PUB-7536, 1997.
- [29] O. Kurnaev, M. Maslov, V. Sytchev. Preliminary consideration of the sweeping TESLA kickers. DESY note, DESY, May 2000.
- [30] K. Flöttmann, V. Paramonov (ed.) Conceptual design of a Positron Pre-Accelerator for the TESLA Linear Collider, TESLA 99-14, DESY, 1999
- [31] K. Flöttmann, V. Paramonov (ed.) Conceptual design of a Positron Injector for the TESLA Linear Collider, TESLA 2000-12, DESY, 2000
- [32] V.V. Balandin, N.I. Golubeva, Hamiltonian Methods for the Study of Polarized Proton Beam Dynamics in Accelerators and Storage Rings. DESY Report 98-016, DESY, Hamburg, 1998